Bulletin of Romanian Chemical Engineering Society

1 2019

ISSN 2360-4697
Edited by SICR and Matrix Rom

The journal is included in the international database
INDEX COPERNICUS INTERNATIONAL

ISSN 2360-4697

Bulletin of Romanian Chemical Engineering Society

Volume 6 2019 Number 1

Contents

ADVANCED PROCESS MODELLING OF TAME INDUSTRIAL SYNTHESIS IN gPROMS®

Elena Cătălina UDREA, Valentin PLEȘU*, Costin Sorin BÎLDEA

University POLITEHNICA of Bucharest, Department of Chemical and Biochemical Engineering, str. Gh. Polizu 1-7, RO-011061, Bucharest Romania

Abstract

Tert-amyl methyl ether (TAME), widely used as gasoline additive, is obtained by the etherification of isoamylenes with methanol. This study develops a mathematical model simulating the behavior of two fixed-bed catalytic reactors for TAME synthesis in an industrial plant. Each reactor consists in a fixed bed of acidic catalyst (Amberlyst 35 wet) of 7.6 m height and 2 m diameter, which is operated adiabatically. The model includes dynamic, one-dimensional mass and energy balance equations, together with appropriate initial and boundary conditions. For numerical integration, the axial coordinate is discretized by the backwards finite difference (BFDM) method. The model is used to predict the transient profiles of molar concentration and temperature along the reactor beds. The model is implemented in gPROMS® ModelBuilder, with physical properties calculations supported by SIMULIS®. Comparison with industrial data shows good agreement.

Key words: Fixed-bed reactor, dynamic modelling, numerical integration, gPROMS

1. Introduction

The octane rating indicates the performance of the gasoline and aviation fuels, more precisely the maximum compression ratio at which a particular fuel can be utilized in an engine without „knocking" of the fuel / air mixture. Gasoline with high octane number is used in high performance engines that require high compression ratios. Tetraethyl lead, used in the past as octane enhancer, was forbidden because of its toxicity and it was replaced by other octane boosters, as light ethers. Amongst them, the methyl-tert-butyl ether (MTBE) - employed on large scale in the 1990s – was phased out because polluting the ground water. Currently, MTBE is replaced by the more environmentally-friendly tert-amyl methyl ether (TAME) and ethyl-tert-butyl ether (ETBE). TAME is mostly used as an oxygenate additive to gasoline, enhancing the octane number, raising the

* Corresponding author: Email address: v_plesu@chim.upb.ro

oxygen contents, and reducing the exhaust emissions of volatile organic compounds.

Figure 1 shows the general scheme of a Fluid Catalytic Cracking (FCC) unit together with the downstream process. The reactor effluent is separated in the Main Column. The overhead, containing mainly C1-C5 hydrocarbons is further processed in the Gas Concentration (GASCON) unit. The heavy product of the GASCON unit is hydro-desulphurized. The heavier components (HCN) are sent to the gasoline pool. The lighter isoamylene-rich fraction (LCN) is used for production of tert-amyl methyl ether (TAME).

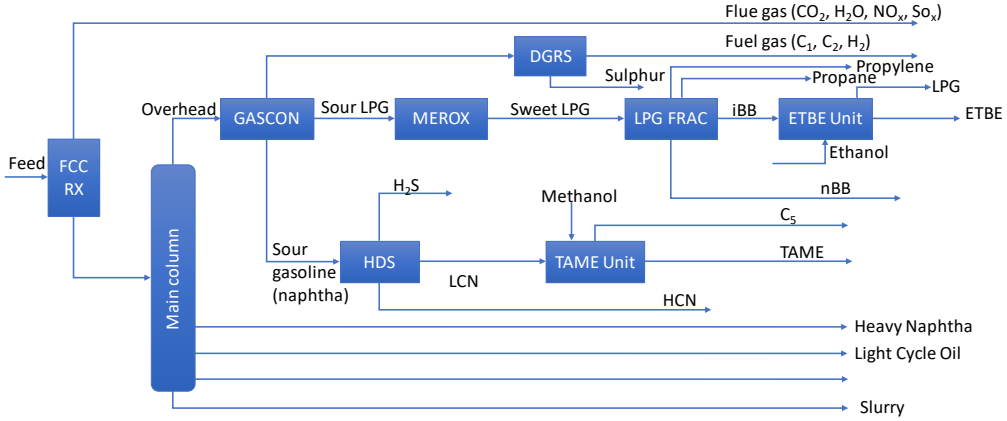

Fig 1. Fluid Catalytic Cracking plant

TAME is obtained by the reaction of methanol with the isoamylenes (2-methyl-1-butene, 2M1B, and 2-methyl-2-butene, 2M2B) from the Light Cracking Naphtha (LCN) fraction. The main reactions of the TAME process are the etherification reactions of isoamylenes with methanol and the isomerization reaction between the two isoamylenes (Figure 2). The reactions take place in liquid phase in the presence of a catalyst: ion exchange resin like Amberlyst 35 wet. In addition to the three main reaction, secondary reactions such as dimerization of isoamylenes, dehydration of methanol, etc. occur.

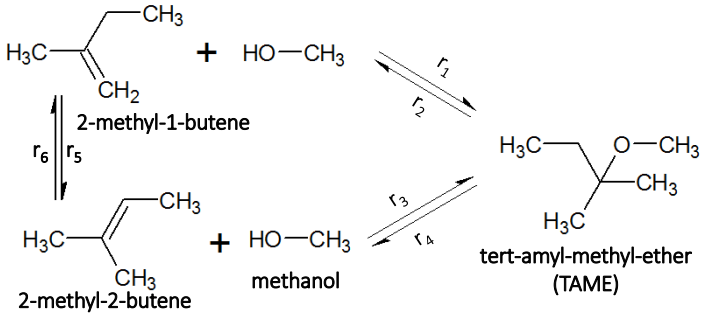

Fig 2. TAME reaction system

Figure 3 shows the flowsheet of the TAME process. The gasoline and methanol (fresh and recycled) are mixed and preheated to reaction temperature. The reaction takes place in a series of two adiabatic, fixed-bed tubular reactors, with intermediate cooling. The effluent contains, besides the TAME product, the unreacted isoamylenes, the inert C5 alkanes (iC5) and the excess of methanol. A distillation column separates TAME concentrate from the C5 – methanol mixture. The latter may be further processed in third reactor, for completing the reaction. Finally, the unreacted methanol is separated by extraction with water. The raffinate is etherified gasoline with a small amount of methanol, while the extract contains the excess of methanol which is recovered by distillation and recycled.

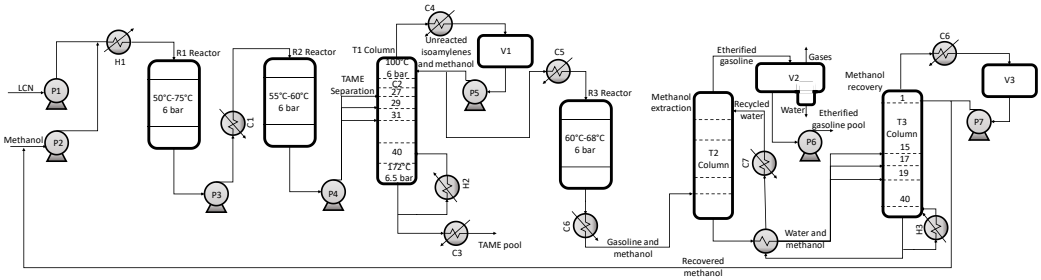

Fig 3. Process flowsheet diagram of TAME reaction and separation section [1]

In this work, the mathematical model of the first two reactors (R1 and R2) is developed. The specifications, shown in Table 1, are similar to industrial processes.

Table 1

TAME synthesis reactor operating conditions

Plant capacity / [$t_{gasoline}$ /yr]	175,000		
Internal diameter, D_i / [m]	2		
Packing height, H / [m]	7.6		
Molar ratio alcohol: reactive olefins	1.3		
Feed composition (wt.%)	iC5	2M2B	2M1B
	80.22	13.27	6.51

2. Reactors modelling

In this section, the mathematical model of the industrial reactors for TAME synthesis is presented. The model implemented in gPROMS® includes the mass and energy balance equations with appropriate initial and boundary

conditions. The model is complemented by constitutive equations which allow calculation of the reaction rate and physical properties.

Assumptions

The assumptions of the mathematical model are:

- The reaction mixture contains the following compounds specific to LCN fraction: inerts, grouped as isopentane; methanol; 2-methyl-1-butene; 2-methyl-2-butene; TAME.
- The behavior of the tubular reactor is suitably described by a one-dimensional pseudo-homogeneous model.
- The fluid velocity is constant in a cross section of the reactor (plug-flow).
- The liquid phase and the catalyst particles have the same temperature.

The model unknowns are the component concentrations $C_i(z,t)$, $i \in COMP = \{2M2B,\ MeOH,\ TAME,\ 2M1B,\ iC5\}$ and temperature $T(z,t)$, which are distributed along the axial coordinate z and are changing during the time t. The significance of the other variables is presented in the ***Notation*** section, together with typical value.

Balance equations

The model consists of mass balance equations for each component, and energy balance.

a. Component mass balance

The first term of the equation is the transient term, namely the evolution of concentration in time, while the right-hand side is contains convective, axial dispersion and reaction terms.

$$\varepsilon \cdot \frac{\partial C_i}{\partial t} = -v_s \cdot \frac{\partial C_i}{\partial z} + \varepsilon \cdot D_z \cdot \frac{\partial^2 C_i}{\partial z^2} + \rho_b \cdot \sum_{j \in REAC} \nu_{i,j} \cdot r_j, \qquad (1)$$

$$z \in (0, H),\ i \in COMP$$

In distributed parameter models, the initial and boundary conditions are extremely important. In order to have a well-developed model, the specification of the initial conditions for the time-dependent equations and the corresponding boundary conditions to establish the equation domain are significant [2], [3].

At the ***reactor inlet*** (z = 0), the Robbins-type condition considers a perfectly mixed feed and ensures flow continuity. The incoming fluid is mixed with the liquid inside the reactor.

$$v \cdot C_{tot,in} \cdot x_{in,i} = v \cdot C_i(t,0) - \varepsilon \cdot D_z \cdot \frac{\partial C_i}{\partial z}(t,0),\ i \in COMP \tag{2}$$

At the ***reactor outlet*** (z = H), the Neumann-type condition specifies that the reaction does not takes place outside the reactor.

$$\frac{\partial C_i}{\partial z}(t,H) = 0,\ \ i \in COMP \tag{3}$$

b. Energy balance

The energy balance follows the same structure as the mass balance, this time the partial differential terms being for temperature. The first term is the accumulation (transient) term. Then, the convective and diffusion terms (defined by effective thermal conductivity) follow. Finally, the reaction term contains the enthalpy of the reaction.

$$\begin{aligned}&\left(\varepsilon \cdot \rho_f \cdot C_{pf} + (1-\varepsilon) \cdot \rho_{solid} \cdot C_{ps}\right) \cdot \frac{\partial T}{\partial t} = -\rho_f \cdot C_{pf} \cdot \mathrm{v}_s \cdot \frac{\partial T}{\partial z} + \lambda_z \cdot \frac{\partial^2 T}{\partial z^2} + \\ &+ \rho_b \cdot \sum_{j \in REAC} r_j \cdot \left(-\Delta H_j\right),\ z \in (0,H)\end{aligned} \tag{4}$$

The differential equations is completed with Robbins- and Neumann-type conditions, for reactor inlet and outlet, respectively.

$$v \cdot T^{feed} = \rho_f \cdot C_{pf} \cdot \mathrm{v} \cdot T(t,0) - \lambda_z \cdot \frac{\partial T}{\partial z}(t,0) \tag{5}$$

$$\frac{\partial T}{\partial z}(t,H) = 0 \tag{6}$$

The **initial conditions** set the values of the time-dependent variables at the initial moment (t = 0) inside the reactor.

$$C_i(0,z) \ = \ C_i^*(z) \tag{7}$$

$$T(0,z) \ = \ T^*(z) \tag{8}$$

Reaction rate

The kinetic model based on activities [4] follows the Eley-Rideal mechanism [5]. Considering 2 active centers and assuming that methanol is the only species adsorbed on the catalyst surface, the expressions of the reaction rates are:

R1: MeOH + 2M1B ⇔ TAME $$r_1 = L^2 \frac{k_{ap,1} \cdot K_M^2 \left(a_{1B} \cdot a_M - \frac{a_T}{K_{eq1}} \right)}{\left(1 + K_M \cdot a_M\right)^2} \quad (9)$$

R3: MeOH + 2M2B ⇔ TAME $$r_3 = L^2 \frac{k_{ap,2} \cdot K_M^2 \left(a_{2B} \cdot a_M - \frac{a_T}{K_{eq2}} \right)}{\left(1 + K_M \cdot a_M\right)^2} \quad (10)$$

R5: 2M1B ⇔ 2M2B $$r_5 = L \frac{k_{ap,3} \cdot K_M \left(a_{1B} - \frac{a_{2B}}{K_{eq3}} \right)}{1 + K_M \cdot a_M} \quad (11)$$

Considering an Arrhenius-type expression for the temperature-dependent kinetic and adsorption equilibrium constants, as presented in the equations below, the model has the following parameters.

$$k_{ap,j} = k_{0,ap,j} \cdot \exp\left(-\frac{E_{a,j}}{R \cdot T} \right) \quad (12)$$

Table 2

Parameters of apparent kinetic constant

Kinetic constant	$k_{0ap,j}$ (kmol/(kg_{cat}·h)	$E_{a,j}$ (kJ/kmol)
$k_{ap,1}$	$5.4 \cdot 10^{13}$	$1.06 \cdot 10^5$
$k_{ap,3}$	$2.03 \cdot 10^{11}$	$9.2 \cdot 10^4$
$k_{ap,5}$	$1.16 \cdot 10^{10}$	$8.2 \cdot 10^4$

$$K_M = K_{0,M} \cdot \exp\left(-\frac{\Delta H_M^{ads}}{R \cdot T} \right) \quad (13)$$

Table 3

Parameters of adsorption constant

M	ΔH_M^{ads}(kJ/kmol)	$K_{0,M}$
Methanol	-10,000	8.34×10^{-2}

The expressions of temperature-dependent equilibrium constants are taken from [6].

R1:MeOH + 2M1B ⇔ TAME $$K_{eq1} = \exp\left(-8,3881 + \frac{4041,2}{T}\right) \quad (14)$$

R3:MeOH + 2M2B ⇔ TAME $$K_{eq3} = \exp\left(-8,2473 + \frac{3225,3}{T}\right) \quad (15)$$

R5:2M1B ⇔ 2M2B $$K_{eq5} = \exp\left(-0,1880 + \frac{833,3}{T}\right) \quad (16)$$

Liquid phase properties

The reaction mixture presents a strong non-ideal behavior induced by the high polarity of methanol as compared to other components. The non-ideality of the liquid phase is described by the NRTL model. Physical properties (molar density, liquid dynamic viscosity, molar heat capacity, etc.) are estimated with relationships and parameters taken from Simulis® [7]. More details are given in reference [8].

3. Results and discussions

Once the model is defined and correctly implemented in gPROMS, the process is simulated. The numerical method discretizes the axial coordinate by the backward finite differences method (BFDM) and integrates in time the resulting set of ordinary differential equations (ODEs). A study was conducted to determine the number of discretization steps. As can be seen, from Fig. 3, 80 axial discretization steps are enough as practically there no change of the temperature and concentration profiles when the number of steps is doubled.

Figure 4 shows steady-state concentration and temperature profiles along the two fixed-bed adiabatic reactors. The reactants are consumed, and the TAME product is formed. The temperature increases due to the exothermic character of the etherification reaction. The temperature difference between the two reactors is due to the intermediate the cooling.

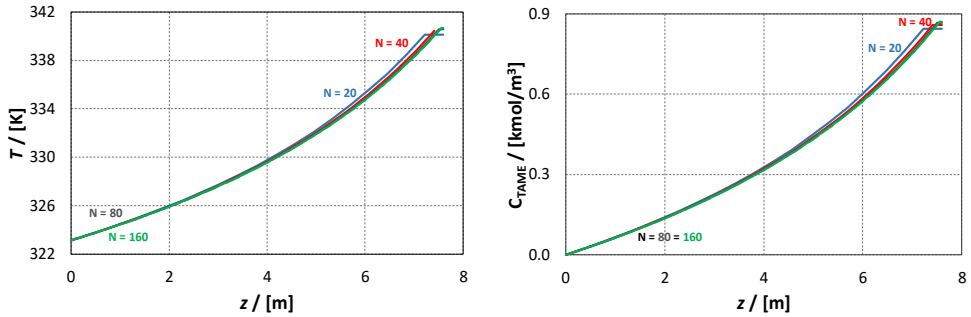

Fig. 3. Effect of the number of discretization steps on the axial temperature and concentration profile along the first reactor

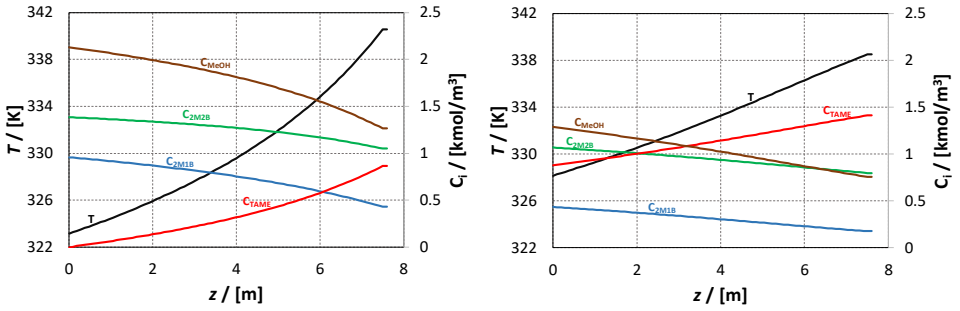

Fig. 4. Evolution of the temperature and concentrations of the reaction systems components along the reactors R1 (left side) and R2 (right side)

Figure 5 shows the dynamic behavior of the system, when the inlet temperature is increased by 10°C.

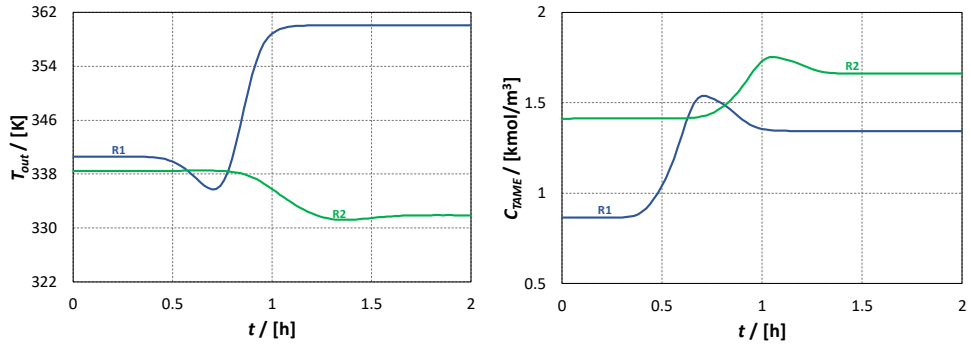

Fig 5. The response of temperature and TAME concentration at the exit of the two reactors at the addition of 10°C to the inlet temperature in the R1 reactor

In figure 5 it is noticed that the reactor outlet temperature begins to change after 0.4 hours, corresponding to the residence time for R1 reactor. The temperature at R2 reactor outlet begins to change for another 0.4 hour (0.8 hour).

In the mass and energy balance equations, it can be observed that concentration and temperature time-derivatives are multiplied by different factors. This means that the concentration and temperature changes will propagate at different speeds along the catalytic layer. In particular, the concentration disturbances move with the flow rate. On the other hand, the temperature changes propagate at a lower speed due to the inertia of the catalyst bed. After increasing the inlet temperature, the reaction rate increases in the first part of the reactor. As the reactants are consumed, towards the reactor-exit the reactants concentration decreases. Less heat is generated and therefore the temperature decreases. After a while, the increase of temperature at the reactor inlet affects the temperature at the end of catalyst bed.

Figure 6 illustrates the temperature and concentration profiles of the reactants and the product throughout the reactors, at different times.

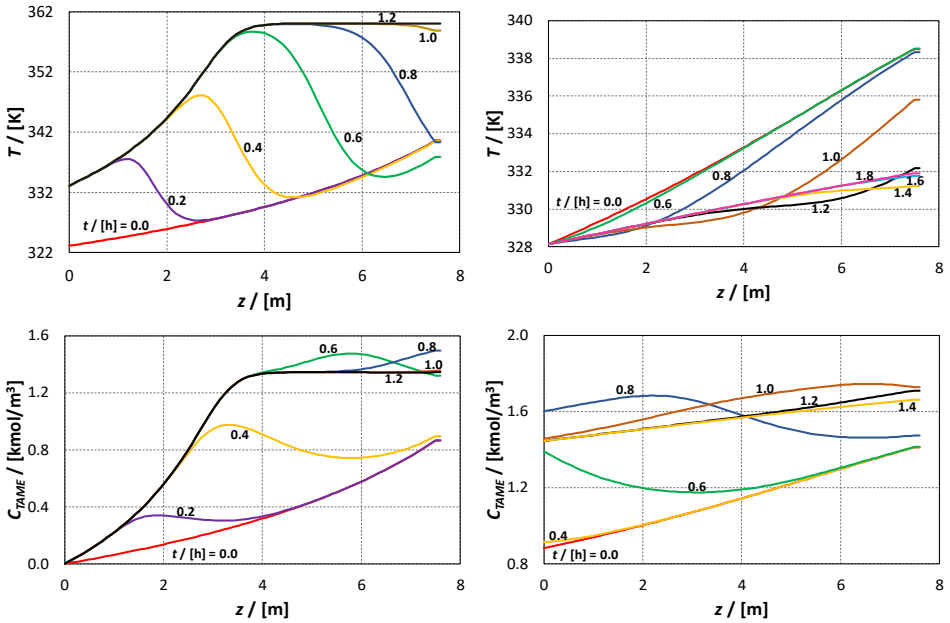

Fig 6. The temperature and TAME concentration profiles along the R1 (left side, up and down) and R2 (right side, up and down) reactors and at different time points

It can be observed in Figure 6 that temperature, following the introduction of the perturbation, reaches the stationary state after 1.2 hours in the first reactor and after 1.8 hours in the second reactor. In the case of concentration profiles, regardless of the compound, the concentrations reach the stationary state after about 1.2 hours in the first reactor and after 1.4 hours in the second reactor.

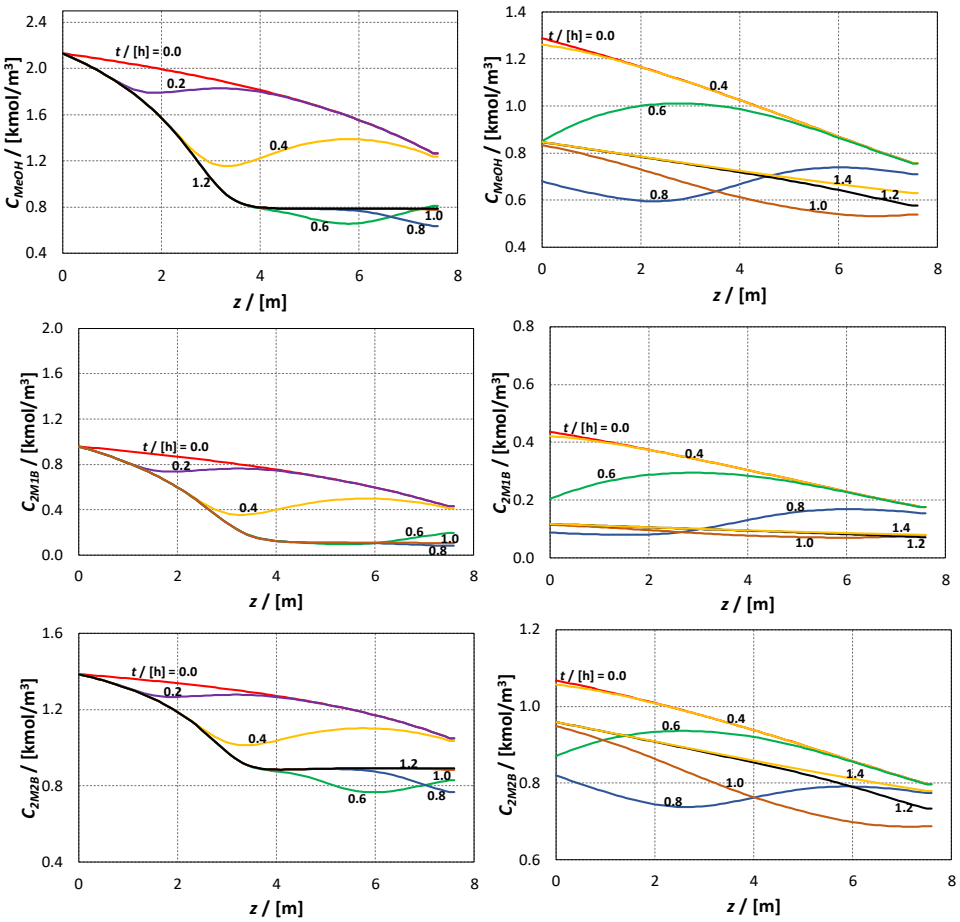

Fig 7. Concentration profile of methanol (top), 2M1B (middle) and 2M2B (bottom) along the R1 (left side) and R2 (right side) reactors at different time points

6. Conclusions

gPROMS® is a suitable environment for advanced process modelling. Detailed mathematical model is proposed for component mass balance and energy balance supported by adequate thermodynamic and kinetic models for reactors. Time and space profiles for temperature and concentrations are presented. Time profiles show that the steady state conditions are reached quite quickly. The model developed in this study proved to describe well the industrial scale reactors. Model solution results give detailed information about the behavior of both reactors. These results can assist the process engineer in decision making on correct process operation.

Table 4

The concentrations (mass fractions) obtained at the R2 reactor outlet in gPROMS® presented in comparison with the industrial results

Components	gPROMS® results	Industrial data
TAME	0.209	0.1873
Isoamylenes	0.099	0.0632
Methanol	0.035	0.0384
Inert	0.657	0.6985

Notation

a_i – liquid-phase activity of component i
$K_{eq,j}$ – thermodynamic equilibrium constant of reaction j
$k_{ap,j}$ – apparent kinetic constant of reaction j, (kmol/kg_{cat}/h)
K_M – adsorption equilibrium constant of component M (methanol) on the active center,
ΔH_M^{ads} – heat of adsorption of component M (methanol), (kJ/kmol)
L – concentration of active sites on the catalyst (5.2)
$E_{a,j}$ – activation energy of reaction j, (kJ/kmol)
$k_{0ap,j}$ – preexponential factor of apparent kinetic constant of reaction j, (kmol/kg_{cat}/h)
$K_{0,M}$ – preexponential factor of adsorption equilibrium constant of component M (methanol,
i – component identification, (2M2B, MeOH, TAME, 2M1B, iC5)
j – reaction number (R1, R3, R5)
ρ_b – bulk density (800 kg_{cat}/m^3_f)
ρ_s – solid density (2000 kg_{cat}/m^3_f)
ρ_f – fluid density (9.06… 10.96 kmol/m^3_f)
C_{pf} – fluid specific heat capacity (154 … 192 kJ/kg_f/K)
C_{ps}– solid specific heat capacity (1.518 kJ/kg_s/K)
D_z – axial diffusivity (0.002 … 0.003 m^3_f/m_{cat}/h)
λ_z – axial thermal conductivity (0.6 … 0.9 W/m_r/K)
ε – bed voidage fraction (0.6 m^3_f/m^3_r)
ΔH_j – enthalpy of reaction j, (R1: -36140.7 kJ/kmol; R2: -28909.9 kJ/kmol; R3: -7230.87 kJ/kmol)
R – ideal gas constant (kJ/kmol/K)
$v_{i,j}$ – stoichiometry of component i in reaction j
t – time variable
z – axial direction
$C_i(t,z)$ – molar concentration of component i, (1.385 …0.81 2M2B, 2.13 …0.77 MeOH, 0.9 … 1.4 TAME, 0.95 …0.18 2M1B, 6.17…6.3 iC5 kmol/m^3_f)

$C_{tot,in}$ – inlet total concentration, (1.38 2M2B, 2.13 MeOH, 0.9 TAME, 0.95 2M1B, 6.17 iC5 kmol/ m^3_f)
$x_i(t,z)$- molar fraction of component i
$x_{in,i}(z)$- inlet molar fraction of component i (0.13 2M2B, 0.2 MeOH, 0 TAME, 0.09 2M1B, 0.58 iC5)
$T(t,z)$ – reactor temperature
T^{feed} – feed temperature (323.15 K)
v_s – superficial velocity (1.546 $m^3_f/m^3_r/h$)
$r_j(z)$ – rate of reaction j
$F_{v,,in}$ – inlet volumetric flowrate (3.247 MeOH, 33.65 LCN m^3/h)
v_r – reactor volume (23.86 m^3)
Indices: M – methanol, 1B – 2M1B (2-methyl-1-butene), 2B – 2M2B (2-methyl-2-butene), T – TAME.

REFERENCES

[1] Muja, I., Nastasi, A., Obogeanu, F., Grozeanu, I., Anghel, C. (1994). *Synthesis process for metoxylated gasoline* (Rom.). State Office for Inventions and Trademarks, Bucharest, Romania, 108972 B1.
[2] Hangos, K., Cameron, I. (2001). *Process Modelling and Model Analysis*, PSE, v.4. London, UK; San Diego, USA: Academic Press.
[3] Botella Tapiador, E. (2017). *Modelling and experiments for TAME synthesis by reactive distillation*, Msc. Thesis, University POLITEHNICA of Bucharest.
[4] Ferreira, M., Loureiro, J., Number of Actives Sites in TAME Synthesis: Mechanism and Kinetic Modeling. *Industrial and Engineering Chemical Research*, 43, (2004), 5156-5165.
[5] Froment, G.F., Bischoff, K.B., De Wilde, J. (2011). *Chemical Reactor Analysis and Design 3rd edition*, John Wiley & Sons Inc, United States of America, 71-81.
[6] Rihko, L.K., Kinetics of Heterogeneously Catalyzed tert-Amyl-Methyl-Ether Reaction in the Liquid phase. *Industrial and Engineering Chemistry Research*, 34, (1995), 1172-1189.
[7] SIMULIS® Thermodynamics, *Thermodynamics models V.2.0*, ProSim SA. 2014.
[8] Udrea, E. C. (2018). *The study of TAME synthesis process* (Rom.). Msc. Thesis, University POLITEHNICA of Bucharest.

MATHEMATICAL MODEL TO PREDICT THE TANKERS SAFE LOAD WITH VACUUM GASOIL

Ioan Alexandru TUTUN[1,*], Claudia KONCSAG[2], Tănase DOBRE[1]

[1]University POLITEHNICA of Bucharest, Chemical and Biochemical Engineering department, 1-3 Gheorghe Polizu, 011061, Bucharest, Romania
[2]Ovidius University Of Constanta, 124 Mamaia Street, 900527, Constanta, Romania

Abstract.

A great number of Vacuum Gasoil transshipments data obtained in the last 5 years from more than 23 major transshipment hubs have been investigated in this work in order to obtain a general analysis of its possible contaminants in the Midstream Sector. The data correlated in model were gathered from samples taken before, during and after the transshipment between wither Terminal/Vessel, Vessel/Vessel and Vessel/Terminal as per ASTM D4057. The analysis was thereafter performed in laboratories of First-Class Independent Inspector Laboratory and Terminals/Refineries laboratories. Correlations were derived which show that the vacuum gasoil quality is highly influenced by the Onboard Quantity (OBQ) present on board of the vessel before loading, far more than shown in the International Standard Guidelines in force at present time. It was found that implementing a blending program library along with a statistical data base and existing general guidelines drawn both from International Standards in Force and guidelines proposed by the author, generated a mathematical and logical model that delivers the maximum content of Fuel Oil in a given tank, over which we can safely load the Vacuum Gasoil, excluding the possible damage by contamination in 99% of the cases. The same model was run on the existing data from previous operations selected by a randomizer program, respecting the request to have a prediction reliability of 99%. In addition, this model can further indicate the level of damage suffered already by the Vacuum Gasoil, which was already contaminated with Fuel Oil, for which can be of high value in case of an investigation or pending Claim towards recovering the damage.

Key words: OBQ, vacuum Gasoil, fuel oil, contamination, asphaltenes

Introduction

Over the recent years, there has been an increase in the qualitative incidents in the Midstream Sector of the Oil and Gas Industry. The challenges arises due to the ever-fluctuating price of crude and petroleum products in all over the world.

The marketers are always looking for the best price on the market, price which usually comes with a hidden aspect. And since most of the quantitative

* Corresponding author: Email address: alex.tutun@yahoo.com

losses are being limited and dissipated due to more and more efficient quantification solutions available, the speculation on the price tends to lean towards a qualitative direction. The quality claims in midstream sector, with preponderance in the Marine Shipping Industry, has always had its downsides, before due to the lack of technology to allow a very accurate and representative sampling and analysis of the cargo, and thereafter due to the limitations imposed by performing such verifications on board of tankers. Even if the industry has come a long way and succeeded to establish a minimum standard requirement [1] in order to increase the representativity of the results obtained, due to the numerous different particularities of each operation there are still many gaps to cover when it comes to perform the best qualitative due diligence.

One of the factors that tend to not be given a response nowadays is the On-Board Quantity of a tanker or shore tank (also referred as OBQ [2]), which represents, without a doubt, a risk of contamination for the nominated cargo subjected to be loaded. And since the tank cleaning procedures [3] are lengthy, costly, bunker consumable, water consumable and generate slops, all marketers tend to avoid it, taking a risk that is often proven unsubstantiated* (*to be noted that every marketer has a different approach for each particular case and that the above is a subjective opinion based on the authors experience in the field, trend observed and specific only for the referrals subject to this article*). If in the past the inspections performed in a tank [4] were much more thorough and not so time depending, nowadays the pre-transfer tanks condition inspections are very limited (due to inert gas conditions of the tanks), also due to a very limited time window for loading and delivery of the product.

One of the many products that has suffered due to this market trend is the Vacuum Gas Oil. Vacuum Gas Oil can be considered an intermediary petroleum product in the refining industry. It is a very quality restrictive product due to the refining processes that it is involved in, processes that are very sensitive to the variations of several crucial parameters like metals, water and asphaltenes, all of which can be found in quite significant levels in fuel oil. Due to the unbalanced production of refineries, Vacuum Gas Oil has become in the recent market both product and feedstock. However, since most refineries are not direct connected through a system of pipelines, and due to the high limitative variations of the qualitative demands over the offer, transportation via sea ways was and is still considered the most viable. Transportation of the Vacuum Gas Oil from the place of its production towards its destination (usually another refinery or in some cases a temporary storage) has its downsides due to the highly risk of contamination. Considering that the Vacuum Gas Oil is not one of the most common traded petroleum product (in comparison with gasoline, gasoil, crude oil and Fuel Oil), there are not so many dedicated storage shore facilities or marine tankers dedicated exclusively for this product. For the marine tankers, this would imply

most of the time very low-cost effective routes and increased demurrages, all money consuming risks that no one cares for or can afford to take. The response found by the industry in this sense was to appoint a Cargo Expeditor [5] which must assess the situation in all its variables and propose the most cost-effective solution to the parties involved. However, this solution is based on the experience of the cargo expeditors with other similar situations and its base knowledge, avoiding or excluding completely the most important part of the issue, which is the prevention part.

In this paper, we will study the behavior of loaded Vacuum Gas Oil on board of the vessels that carried previously Fuel Oil of different qualities, including in it the analysis of several possible cases for cargo tanks preparation and cleaning procedures. The results obtained will thereafter be interpreted into a model that tries to include more parameters and factors to offer a more reliable picture of the risk taken and to limit as much as possible the contamination of the commodity. Also, the model has the target to surpass all the existing industry standards like API/MPMS HM50 [4] or BP Tank Cleaning Guide [6], all in respect of loading VGO on top of Fuel Oil OBQ.

Experimental

In this Step, we have gathered and investigated data from 1,233 Vacuum Gasoil transshipments, relevant to more than 23 major transshipment hubs, throughout 5 years, in order to obtain a general analysis of contamination in the midstream sector. Locations and participation percentages in Vacuum Gasoil transshipments data are given with Fig.1. The data correlated in the model in respect of the Vacuum Gas Oil product studied, were gathered from samples taken before, during and after the transshipment between terminal/vessel, vessel/vessel and vessel/terminal. The analyses of Vacuum Gas Oil were performed in First-Class Independent Inspector Laboratories or Terminals/Refineries Laboratories using international approved standard method of analysis [7-14], relevant to the quality specification sold or bought. The data results gathered were filtered for non-representative cases where there were indications of non-homogeneity (especially in on-board blending cases), where sampling on board was considered as non-representative and the analysis results were non-comparable with shore results in the critical parameters [15] (i.e: density, viscosity, flash point, pour point, water by distillation, sulphur), where laboratory analysis were not performed using standard industry test procedures, as specified in the ASTM or where there were suspicious or proven cases of fraud for quantitative or qualitative procedures used.

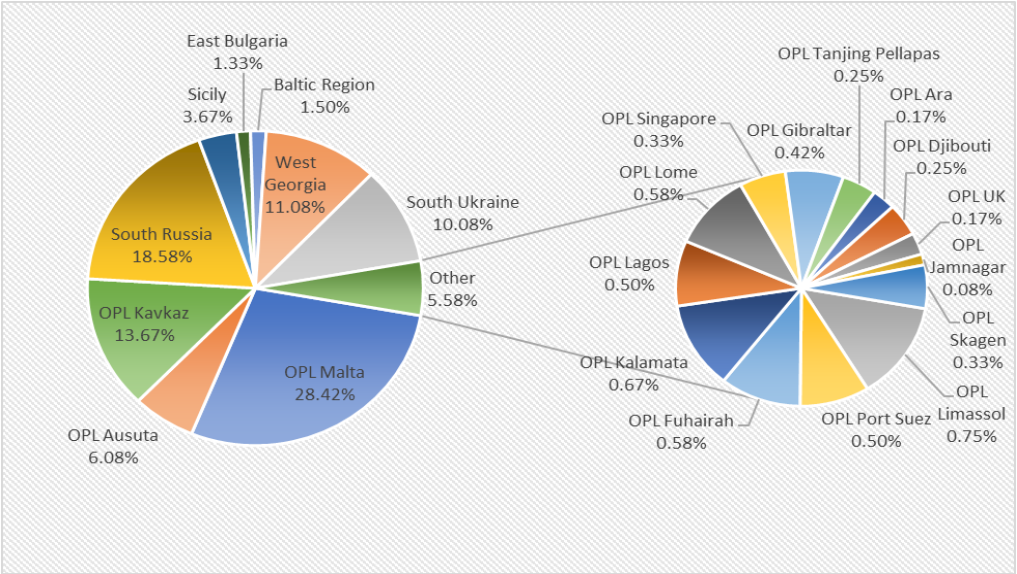

Fig. 1. Locations and participation percentages in Vacuum Gasoil transshipments data

In addition, in respect of the selected cases of study, we collected data regarding the size of the vessel, cargo tanks geometry, capacity of vessel's interior and deck cargo lines, last cargo or cargoes carried with their relevant quality, information about remaining on board after the last discharge of the respective vessel and inspection data on the On Board Quantity (OBQ) determined before loading of the Vacuum Gasoil, especially where measurable quantities were determined.

The sale specification of VGO from different regions were then used in order depict the critical limit values that have the greatest impact in risk of contamination when loading it on top of Fuel Oil OBQ. Putting the data available side to side it was almost immediately notable that the VGO most sensitive quality parameter in this type of situation was the asphaltenes content. Figure 2 and Figure 3 are presenting the variation of asphaltenes content of the VGO before loading (as analyzed from the samples drawn before loading ex. Shore Tank/s [15]) and the results obtained after loading (as analyzed from the samples drawn after loading ex. Vessel's Cargo Tanks [16]).

Vacuum Gasoil quality available on market. Even though the present market offers a wide range of VGO with respect to its quality, it is trended in the sector of Petroleum Trading to pin a certain quality frame to a region. For example, we can see from Table 1 that the content of asphaltene in the VGO lifted from South Russian Region tends to be lower than the ones available in the Mediterranean area. However, even with the wide array of quality fingerprints available to

differentiate each VGO one from another, there does not seem to be a dependence between the asphaltenes content and the other parameters.

Typical selling specification of vacuum gasoil. Of course, Trading of Petroleum Products is a two way street because more of than usual, the deals are not back to back on quality clause. That leads almost every time to a different quality selling specification compared to the quality purchase one. In Table 2 we can see few selected cases with the limits imposed by several buyers of the VGO. Most of the receivers will factor their quality clauses and requirements in line with the scope of use of the VGO. Furthermore, receivers are also amending their quality requirements in line with a discounted price, dependent with the demand of the material [16-17].

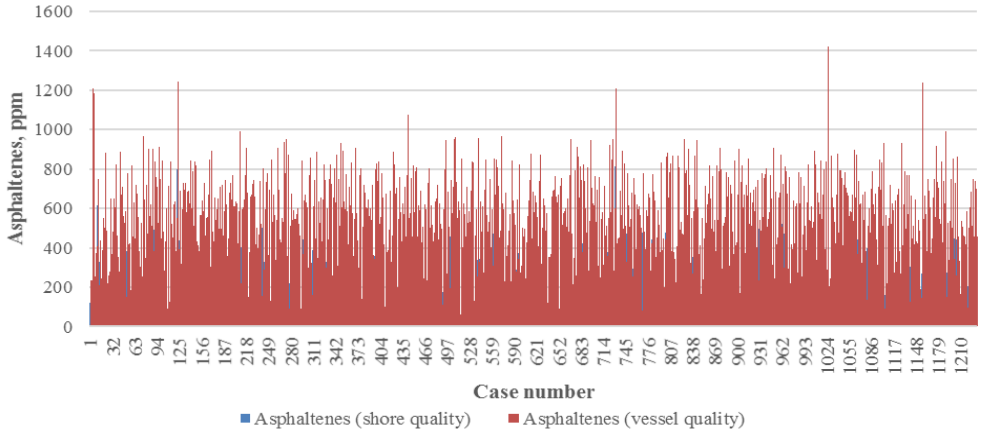

Fig. 2. Shore/Ship of total asphaltenes content in vacuum gasoil transshipments (1232 cases)

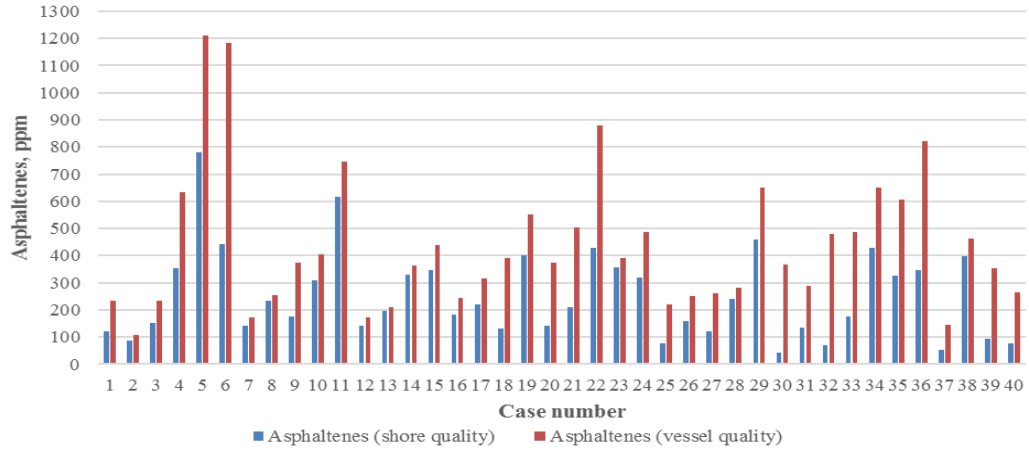

Fig. 3. Shore/Ship detail respect to total asphaltenes content in vacuum gasoil transshipments for 40 cases from Fig. 2

Vacuum Gas Oil is often very restrictive on quality requirements when bought, especially on parameters like asphaltenes, carbon residue (CCR), metals and water content. For our selected cases, Selling Specification Qualities limit the asphaltenes content to an average of 500 ppm.

Table 1

Examples of Vacuum Gasoil quality available on market

№	Parameter	Units	East Bulgaria	East Turkey	South Greece	South France	West Georgia	South Spain	West Spain	South Russia
1	Density at 15°C	g/l	924.5	918.7	895.5	912.0	914.6	932.6	886.2	911.2
2	Kinematic Viscosity at 50°C	cSt	16.26		14.54	59.17	47.05	36.00		43.96
3	Sulphur	% mass	0.48	0.26	1.6	0.98	0.268	1.26	0.448	0.871
4	Pour Point	°C	21	18	33	45	6		48	33
5	Flash Point	°C		130	93.5	184	146	>120	175	185
6	Asphaltenes	ppm	780	250	70	469	760	1042	195	294
7	Organic Chlorides	ppm	ns	ns	<2	ns	1	ns	<1	0.3
8	Carbon Residue	% mass	0.22	0.15	0.1	0.35	0.4	ns	0.12	0.27
9	Bromine Number at 360°C cut	mgBr/ 100g	ns	ns	3	2.6	2.8	ns	1.8	2.1
10	Nickel	mg/kg	0.2	0.3	0.1	0.1	1.1	ns	2	0.1
11	Vanadium	mg/kg	0.4	0.27	0.5	0.8	1.1	ns	<1	0.5
12	Sodium	mg/kg	ns	5.46	0.1	0.1	1	0.2	0.2	0.3
13	Copper	mg/kg	<1	<1	ns	<0.2	0.2	ns	<1	<0.1
14	Iron	mg/kg	1.63	ns	0.1	0.1	2.3	ns	<1	0.4
15	Aluminum	mg/kg	ns	ns	ns	1	ns	ns	<5	0.2
16	Silicon	mg/kg	ns	1.29	<1	1	ns	ns	<10	0.4
17	Calcium	mg/kg	1.23	ns	ns	0.5	ns	ns	<1	0.1

Contaminants origin – fuel oil specification by regions. The variation of asphaltenes content in Fig. 2 and Fig. 3 (the increase of it) has in most of the cases only one cause, which is the cross contamination of the VGO with Fuel Oil during its transhipment. This cross contamination can originate either from shorelines (less likely but nonetheless encountered in some places) but most likely from the Fuel Oil OBQ present on board of the vessel in the cargo tanks before loading. It is a usual practice to use a tanker to lift VGO after it had previously carried Fuel Oil, without cleaning its cargo tanks, which is at present time the most common source of contamination of the VGO with asphaltenes.

When compared to each region presented in Table 3, we can observe that the asphaltenes content differs between the regions and does not seem to be dependent of other parameters. Considering that the refineries process the same

types of crude oils with certain margins (purchased usually from term contracts), the asphaltenes content varies so slightly through time, but not significantly [18].

Table 2

Examples of Selling specification

No.	Parameter	Units	Case 1	Case 2	Case 3	Case 4	Case 5
1	Density at 15°C	g/l	0.915 max	0.925 max	0.925 max	0.93 max	0.92 max
2	Kinematic Viscosity at 50°C	cCt	50 max	35 max	50 max	50 max	50 max
3	Pour Point	°C	40 max	33 max	40 max	40 max	42 max
4	Flash Point	°C	150 min	-	100 min	100 min	150 min
5	Asphaltenes	mg/kg	500 max	600 max	500 max	400 max	500 max
6	Organic Chlorides	mg/kg	-	-	-	2 max	-
7	Bromine Number at 360°C cut	mgBr/ 100g	-	8 max	5 max	4 max	5 max
8	CCR	% mass	0.5 max	0.4 max	0.4 max	0.8 max	0.4 max
9	Nickel	mg/kg	1 max	1 max	1 max	1 max	2 max
10	Vanadium	mg/kg	1 max	1 max	0.5 max	1 max	2 max
11	Sodium	mg/kg	1.5 max	2 max	1.5 max	1 max	1 max
12	Copper	mg/kg	-	1 max	1 max	-	1 max
13	Iron	mg/kg	2 max	3 max	1.5 max	3 max	1 max
14	Aluminum	mg/kg	-	-	-	-	2 max
15	Silicon	mg/kg	-	5 max	-	1 max	1 max
16	Calcium	mg/kg	-	-	-	-	4 max
17	Zinc	mg/kg	-	-	-	-	-
18	Phosphorus	mg/kg	-	-	-	-	-

Table 3

Fuel oil specification by regions

No.	Parameter	Units	Novorossiysk, Russia	Rotterdam, Netherlands	Ventspils, Latvia	Greece	Iran
1	Statistical qualities collected	-	92	150	133	61	77
2	Density at 15°C	g/l	0.977	1.0002	0.9995	0.995	0.975
3	Kinematic Viscosity at 50°C	cCt	589.9	450.6	650.5	443.2	378.2
4	Pour Point	°C	4	-3	9	6	3
5	Flash Point	°C	132	95	110	77	88
6	Asphaltenes	mg/kg	61000	120000	82000	78000	65000
7	Organic Chlorides	mg/kg	10				
8	CCR	% mass					
9	Bromine Number at 360°C cut	mgBr/ 100g	4		16.5	2	
10	Nickel	mg/kg	23	44	54	16	12
11	Vanadium	mg/kg	46	150	160	190	99
12	Sodium	mg/kg	18	22	24	29	19
13	Copper	mg/kg	<1	<1	<1	<1	<1
14	Iron	mg/kg	30	8	80	7	12

In respect of the other parameters, the asphaltenes content shows the biggest gap in values between VGO and Fuel Oil, which is also the first indication of a Fuel Oil contamination. In present time, it is very difficult to prove with preciseness the point where the VGO was contaminated or picked up another bump in the asphaltene content, but none of the experts in the field can deny that Fuel Oil is the prime cause of contamination of the VGO [S&P Platts]

Developing the model

General assessments: 1) The comparison of the shore/ship asphaltenes content of the Vacuum Gasoil showed a non-linear dependence on the value; 2) The dependence trended to be linked to several factors involved in the transshipment operation like: a) the properties of the previous Fuel Oil cargo carried (density, viscosity, pour point and asphaltenes); b) the discharge performance of the previous Fuel Oil cargo reflected in clingage, ROB/OBQ, remaining cargo in vessel's lines; c) the temperature of the cargo, sea water and ambient during the discharge operation of the previous Fuel Oil cargo; d) vessels particularities (cargo tanks geometry and coating, cargo pumping specification, cargo lines specification)
Factors used: 1) A theoretical approach based on idealistic behaviour and existing theoretical model analogy is impossible due to the complexity of the variables and the limitation of the information available up to the point of making the appropriate decision; 2) The model proposed by us uses the blending equations, empirical data gathered, approximation values and numerical regression in order to predict the increase in asphaltenes content of the VGO cargo loaded on top of the Fuel Oil; 3) The calculation starts with determining the particularities of the vessel. From this, the model makes a supposition of the usual clingage which he considers the base theoretical OBQ. This OBQ is thereafter multiplied by:

a) **Viscosity Factor:** Factor developed from empirical data that considers the possible OBQ increase in dependence with the high viscosity of the Fuel Oil carried as the last cargo. In within the limited values of available data exponential dependence on viscosity of this factor was established (1)

$$F_{Visc} = 1 + 0.051\exp\left(0.2339\left(\frac{\vartheta - \vartheta_{min}}{\vartheta_{min}}\right)\right) \quad (1)$$

b) **Pour Point Factor:** Factor developed from empirical data that considers the possible OBQ increase in dependence with the pour point of the Fuel Oil carried as the last cargo. It is appreciating an exponential dependence of this factor up to limit values of available data (2).

$$F_{pp} = 1 + 0.003\exp\left(2.195\left(\frac{pp - pp_{min}}{pp}\right)\right) \qquad (2)$$

To be noted that the factor was limited to a maximum value of 2.81 under the limitations of this model. After that, no matter how much the pour point was increased, the value remains constant, for the limit values of the available data.

c) **Temperature Factors:** Factors developed from empirical data that takes into account the possible OBQ increase in dependence with the cargo temperature carried (in line with the rheological properties of the Fuel Oil), the sea water temperature and the ambient temperature during the last discharge of the Fuel Oil. First and second temperature factors can be appreciated by mean of relation (3) and (4). Here t_{OB} is the temperature of fuel oil during the previous discharge operation and t_{sw} gives the sea ambient temperature.

$$F_{T1} = \frac{1 + 0.1\left(\frac{t_{OB} - 40}{40}\right)^2 + 0.2\left(\frac{t_{OB} - 40}{40}\right)^4 \; for\; t_{OB} \le 40^0 C}{1 \;\; for\; t_{OB} \succ 40^0 C} \qquad (3)$$

$$F_{T1} = \frac{1 + \left(\frac{t_{sw} - 20}{20}\right)^2 + \left(\frac{t_{sw} - 20}{20}\right)^4 \; for\; t_{sw} \le 20^0 C}{1 \;\; for\; t_{sw} \succ 20^0 C} \qquad (4)$$

d) **Vessel Line Factor**: Factor developed from the empirical data that takes into account the possible OBQ increase in dependence with the Cargo Lines used by the vessel. It uses a polynomial dependence of vessel line factor (F_{Line}) upon active volume of the vessel line (5)

$$F_{Line} = 0.07V_{line} + 1.2\,10^{-4}V_{Line}^2 \qquad (5)$$

e) **Clingage Factor** was developed from the empirical data that considers the usual clingage, which is found on board of the Vessel as the film that adhered to the Bulkheads of the Cargo Tanks.

f) **Sedimentation Factor** can be established from data that considers the increase in sediments in the ROB. It is the case when the Vessel carried out Fuel Oil Cargoes for an extended period, without any Cargo Tanks washings or preparation in between

Applying the model

Based on the statistical data gathered, we have observed the variation of the asphaltene levels in line with the parameters involved and with our proposed factors and tried to depict a dependency towards which the value of the theoretical result would get close enough to the real result.

For this, we have developed a program that uses the data base (existent and with the possibility of extending it) and a specific sets of predictive equations for above presented factors (mostly based on multi-numerical regression with variational tendency). Based on the equations of blending for asphaltenes [15], we have created in the program a short window [Table 4] where the user can input all the available parameters to obtain the critical OBQ. This critical value of OBQ is used later to define the maximum set-value of the asphaltenes level in order to consider the VGO cargo still on specification and acceptable by the receiver. Considering the critical OBQ value as the line that should not be crossed in order to be able to conserve the asphaltenes in the required sale limits, we have define it later on in the model the real OBQ that was responsible for the increment of the asphaltenes value. Since the real OBQ is obtained by the use of industry accepted blending equations, we have considered all errors up to this stage of model to be only negligible as long as they were in the recognized precision arrays for their respective methods of analysis.

Table 4

Model – Blending towards Critical Value

No.	Parameters/Steps	Units	Value
1. Insert parameters of scheduled parcel of VGO			
1	Volume	m³	31775.376
2	Weight	MTA	28890.172
3	Density	g/l	0.9092
4	Asphaltenes	ppm	400
2. Insert quality parameters of OBQ			
5	Density	g/l	0.9892
6	Asphaltenes	ppm	106500
3. Select maximum allowed increasing of asphaltenes content			
7	Increasing of asphaltenes	% weight	**25.00%**
8	Critical value of asphaltenes	ppm	**500.00**
4. Receive critical quantity of OBQ (for inserted quality)			
9	Critical OBQ	% weight	**0.09%**
		m³	**27.552**

On the next stage of the model, we have created an input window to collect all the available parameters for each case, including sufficient items in order to obtain a more comprehensive comparison between the critical OBQ, the real OBQ and the physically measured OBQ. This was a very important stage in our model since it showed an unexpected behavior reporting to the international standard practices. At this stage we also observed the high sensitivity of the VGO

during transshipments respect to physically measured OBQ and variations of the contained asphaltenes.

Table 5

Model Factors Input and Comparison

Parameters				Units	Case 1	Case 2	Case 3	Case 4
Statistical data								
On board quantity	Volume			m³	18.2	0	21	17.5
				% vol.	0.05%	0.00%	0.03%	0.08%
	Weight			MTA	17.781	0.000	20.752	17.066
				% w.	0.06%	0.00%	0.03%	0.08%
	Density			g/l	0.9770	0.9892	0.9882	0.9752
	Asphaltenes			ppm	99000	67900	91000	121000
Vessel loaded	Volume			m³	33231.82	32333.12	67872.22	23236.32
				% vol.	99.95%	100.00%	99.97%	99.92%
	Weight			MTA	31071.75	29843.47	63874.54	21391.35
				% w.	99.94%	100.00%	99.97%	99.92%
	Multipliers (Using OBQ par.)			g/l	0.9350	0.9230	0.9411	0.9206
	Asphaltenes			ppm	121	88	152	354
Total figures (real)	Volume			m³	33250.02	32333.12	67893.22	23253.82
	Weight			MTA	31089.53	29843.47	63895.30	21408.42
	Density			g/l	0.9350	0.9230	0.9411	0.9206
	Asphaltenes			ppm	235	108	233	635
Selling limit of Asphaltenes				ppm				
Empirical prediction of asphaltenes								
Empirical parameters	Multipliers (Using OBQ parameters)	Viscosity factor	Viscosity	cSt	382.0	298.0	176.0	312.0
			Factor	-	1.109	1.087	1.064	1.091
		Pour point fac.	Pour point	°C	9	6	12	9
			Factor	-	1.000	1.000	1.027	1.000
		Temp. factors	Cargo temp.	°C	42	39	49	32
			Sea/Ambient	°C	11	30	5	10
			Temp factor 1	-	1.000	1.000	1.000	1.000
			Temp factor 2	-	1.100	1.000	1.232	1.100
		Clingage factor		m³	12.3	15.3	19.3	23.3
		Line factor	Line capacity	m³	43.0	41.3	83.2	35.0
			Vessel lines condition factor	m³	3.01	2.891	5.824	2.45
	Asphaltenes theoretical			ppm	239	129	227	615
	Difference (theory-Real)			ppm	4	21	-6	-20

The model, considered in Table 5 with imputed and computed data for five cases, establishes the difference between theoretical asphaltenes prediction and those real values, obtained in laboratory. Here we were able to adjust and modify the prediction equation (6) as needed, until the results showed the errors to be in within the acceptable set up limits.

.

Table 6

Example of Calculation

Parameters				Units	Case 19
Statistical data					
On board quantity	Volume			m³	7.2
				% vol.	0.02%
	Weight			MTA	7.122
				% w.	0.02%
	Density			g/l	0.9892
	Asphaltenes			ppm	**106500**
Vessel loaded	Volume			m³	31775.376
				% vol.	99.98%
	Weight			MTA	28890.172
				% w.	99.98%
	Multipliers (Using OBQ parameters			g/l	0.9092
	Asphaltenes			ppm	**400**
Total figures (real)	Volume			m³	31782.576
	Weight			MTA	28897.294
	Density			g/l	0.9092
	Asphaltenes			ppm	**550**
Selling limit of Asphaltenes				ppm	
Empirical prediction of asphaltenes content					
Empirical parameters	Multipliers (Using OBQ parameters	Viscosity factor	Viscosity	cSt	420.0
			Factor	-	1.120
		Pour point factor	Pour point	°C	12
			Factor	-	1.027
		Temp. factors	Cargo temp.	°C	48
			Sea/Ambient temp	°C	-10
			Temp factor 1	-	1.000
			Temp factor 2	-	1.532
		Clingage factor		m³	27.8
		Line factor	Line capacity	m³	42.9
			Vessel lines condition factor	m³	3.003
	Asphaltenes theoretical			ppm	**560**
	Difference (theory-Real)			ppm	**10**

The model constraints were concentrated in a precision marker known as repeatability [13], since it is the most restrictive reference variable available in the international standard practices and also acceptable by the Petroleum Trading Industry as inserted in most of the contractual clauses. We show that by using all the proposed factors and considering the way each one influences the asphaltene changing during the transshipment of the VGO, we have obtained the following basic model equation:

$$P_{OBQ} = P_{0(BaseOBQ)}(F_{visc} + F_{pp} + F_{T1} + F_{T2}) + P_{line}F_{line} + P_{Cling} \quad (6)$$

In Table 6 we can see the implementation in model interface of equation (6) by showing for a specific case the calculation with the results obtained.

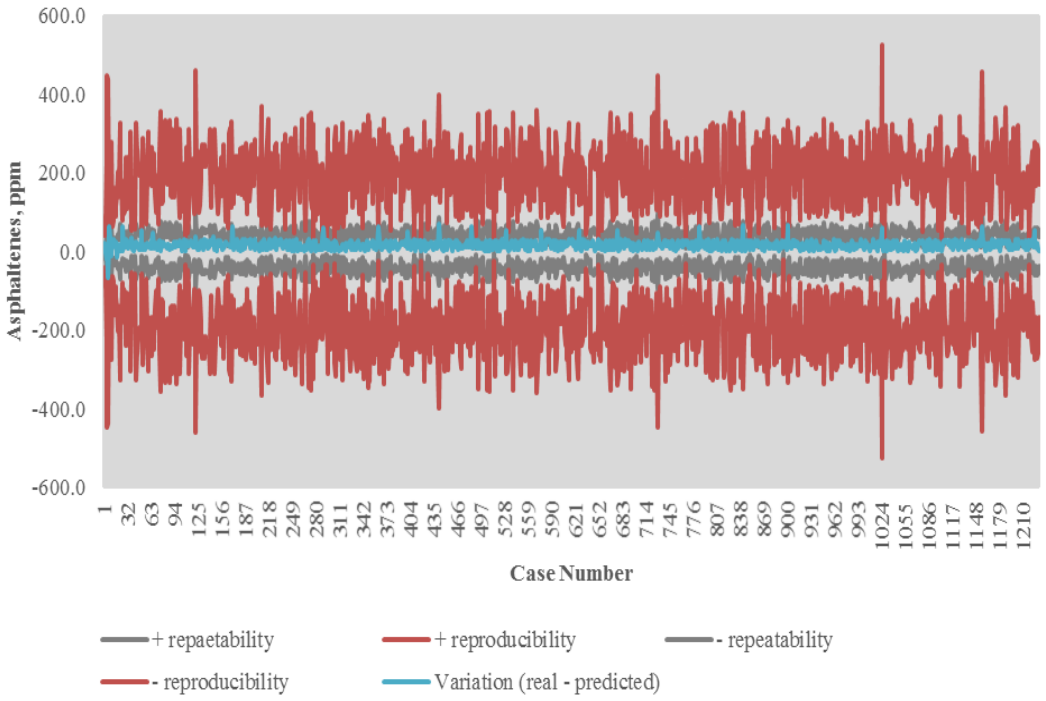

Fig. 4. State of repeatability, reproducibility and real predicted variation for cases from Fig. 2

The model simulations for cases given in Fig. 2 and Fig.3 are concentrated in terms of repeatability, reproducibility and real predicted variation (difference) in Fig. 4 and Fig. 5.

Fig. 5. State of repeatability, reproducibility and real predicted variation for cases from Fig. 3

Results and discussions

In this study, we can observe that the prediction for the asphaltene content are comparable with the results obtained on ship's composite after loading, in within the limit of precision (the limit of precision was taken from the usual method for asphaltene content testing – Total 642)

Applying the proposed model to the studied cases, we observe that the predictions made of the asphaltene content would have indicated the high risk of contamination of the VGO with Fuel Oil, even though the inspection party followed the latest international standard practices (see Table 7).

The more reliable result obtained through this model could be explained by the fact that it takes into consideration factors which the latest international standard practices do not address, like the specific particularities of the vessel, the more detailed parameters of the last cargo carried and the conditions in which it was discharged and also information regarding the contractual quality clauses of cargo transhipped

Table 7

Example of Calculation

Cargo contamination by OBQ - Asphaltenes

Parameter	Units	Predicted Real OBQ	Loaded cargo	Total
Volume	m³	44.153	31,731.223	31,775.376
	% vol.	0.14%	99.86%	100.00%
Weight	MTA	43.676	28,850.028	28,893.704
	% weight	0.15%	99.85%	100.00%
Density	g/l	0.9892	0.9092	0.9093
Quality				
Asphaltenes	ppm	106500	400	560
			Increasing of Asphaltenes content	161ppm [40.25%]
			Critical (Max. allowed) Asphaltenes content, ppm	500
			Reserve to the critical value, ppm	OUT!
			RISK	Cargo OFFSPEC

Conclusions

The presented model is very useful as a tool to predict the critical calculated OBQ towards which you could load on top or not. The critical OBQ cannot any longer be considered as the measured OBQ since in the present days, the OBQ inspections are limited to deck level via vessel's vapor lock valves under inert conditions, using hermetic appliances. The model is very useful in nowadays midstream market because it helps to: i) minimize contamination claims which are highly detrimental and damaging towards every party involved, ii) optimize the vessel's cargo changeover of tanker carriers based on a more field-realistic approach, iii) minimize the production of Slops and Washings from Cargo Changeover, iv) reduce the demurrages caused by delays for unexpected cargo tanks rejections, cargo rejections or claims, v) safeguard the quality of the commodity carried and raise the awareness of the contamination prevention importance instead of being forced to take just corrective actions, which are much more higher in extra cost generating. In addition, the model has the capacity to improve provided that more data available is processed and the data filters are applied accordingly.

REFERENCES

[1] API MPMS Chapter 17.2 Measurement of Cargoes On Board Tank Vessels (includes Errata 1 dated April 2000) 2nd Edition | May 1999 | Reaffirmed: September 2011 2-Year Extension: May 2016.
[2] API MPMS Chapter 17.4 Method for Quantification of Small Volumes on Marine Vessels (OBQ/ROB) 2nd Edition | September 2016.
[3] Energy Institute, London - Hydrocarbon management HM 50 Guidelines for the cleaning of tanks and lines for marine tank vessels carrying petroleum and refined products, October 2018, 5th edition.
[4] API MPMS Chapter 17.8 Guidelines for Pre-Loading Inspection of Marine Vessel Cargo Tanks and Their Cargo-Handling Systems 2nd Edition | August 2016.
[5] Energy Institute, London - Hydrocarbon management HM 95 Guidelines for marine petroleum cargo superintendents, January 2016, 1st edition.
[6] BP Tank Cleaning Guide 2018.
[7] API MPMS Chapter 8.1, Standard Practice for Manual Sampling of Petroleum and Petroleum Products (ASTM D4057).
[8] ASTM D4052 - 18a Standard Test Method for Density, Relative Density, and API Gravity of Liquids by Digital Density Meter.
[9] ASTM D95-13(2018) Standard Test Method for Water in Petroleum Products and Bituminous Materials by Distillation.
[10] ASTM D7157-18 Standard Test Method for Determination of Intrinsic Stability of Asphaltene-Containing Residues, Heavy Fuel Oils, and Crude Oils (n-Heptane Phase Separation; Optical Detection).
[11] ASTM D4294-16e1 Standard Test Method for Sulfur in Petroleum and Petroleum Products by Energy Dispersive X-ray Fluorescence Spectrometry.
[12] ASTM D93-18 Standard Test Methods for Flash Point by Pensky-Martens Closed Cup Tester
[13] ASTM D6560-17 Standard Test Method for Determination of Asphaltenes (Heptane Insolubles) in Crude Petroleum and Petroleum Products 1, 2.
[14] API MPMS Chapter 9.1 Standard Test Method for Density, Relative Density (Specific Gravity), or API Gravity of Crude Petroleum and Liquid Petroleum Products by Hydrometer Method (ASTM D1298).
[15] James G. Speight, *Rules of Thumb for Petroleum Engineers*, Chapter 42, Blending and Mixing, 3rd March 2017.
[16] Hong E., P., Watkinson. A study of asphaltene solubility and precipitation, *Fuel*, 83, 14–15, (2004), 1881-1887.
[17] B. J., Abu, T. Maen, M. Husein, Adsorption of asphaltenes from heavy oil onto in situ prepared NiO nanoparticles, *Journal of Colloid and Interface Science*, 378, 1, (2012), 64-69.
[18] X. Li, P. Chi, X. Guo, Q. Sun, Effects of asphaltene concentration and asphaltene agglomeration on viscosity, *Fuel*, 255, 1 November 2019, 115825.
[19] API MPMS Chapter 8.3 Standard Practice for Mixing and Handling of Liquid Samples of Petroleum and Petroleum Products (includes Errata 1 dated March 1996) (ASTM D5854).
[20] API MPMS Chapter 7, 1st Edition, June 2001, Reaffirmed: February 2012 2-Year Extension: March 2017.
[21] API MPMS Chapter 3.1A, 3rd Edition August 2013.

IN-SILICO MODULATE GLYCOLYTIC OSCILLATOR IN MODIFIED *E. COLI* TO CONTROL BIOPROCESSES OF INDUSTRIAL INTEREST

Marina MIHALACHI, Gheorghe MARIA*, Luminita Cristiana GIJIU

University POLITEHNICA of Bucharest, Department of Chemical and Biochemical Engineering, str. Gh. Polizu 1-7, RO-011061, Bucharest Romania

Abstract

*Tryptophan (**TRP**) is an aromatic non-polar amino-acid essential, whose biosynthesis maximization is of high practical importance in industry, and medicine. On one hand, it is to underline that **TRP** synthesis is an oscillatory process strongly connected to the glycolysis through the **PEP** (phosphoenolpyruvate) node. On the other hand, it is well-known that glycolysis, under certain environmental conditions, displays autonomous oscillations of the glycolytic intermediates' concentrations thus reflecting the dynamics of the control and regulation of this major catabolic pathway with a major role in the cell central carbon metabolism (**CCM**) in living cells. Consequently, glycolysis model is the 'core' module of any systematic and structured model-based analysis of most of metabolic sub-process. By coupling two adequate reduced kinetic models for the glycolysis and **TRP** synthesis in the **E. coli** cells, adopted from literature, with the model of a semi-continuous bioreactor, this paper derives, for the first time, an **in silico** analysis of the optimal operating conditions of the bioreactor used for tryptophan synthesis, with accounting for the two interfering oscillatory processes. The paper also points-out the main factors influencing the glycolytic oscillations, by in silico (model-based) identifying some conditions, able to be modulated leading to occurrence of stable glycolytic oscillations in the E. coli cells, and **TRP** synthesis optimisation.*

Keywords: Reduced dynamic models; Glycolysis; Tryptophan synthesis; *Escherichia coli;* Oscillation occurrence; Bioreactor optimization

1. Introduction

When developing an industrial bioprocess, one essential engineering problem concerns the choice not only of the best bioreactor operating policy, but also the most suitable cell culture with genetically modified micro-organisms (GMO) to get the maximum reactor productivity for the target metabolite. As described in the literature, such GMO-s, can be *in-silico* (math model-based) design by using Systems Biology, Bioinformatics, and (Bio)Chemical Engineering tools [1].

In the last decades, there has been a continuous trend to replace complex chemical syntheses, energetically intensive and generating toxic wastes, with

* Coresponding author: Email address: gmaria99m@hotmail.com

biosynthesis or biological processes to produce some fine chemicals or organic compounds in food, pharmaceutical, or detergent industry, using enzymatic or cell culture batch, semi-batch (fedbatch), fixed-bed, or fluidized-bed reactors.[1,2] This includes, among others, the production of monosaccharides derivatives, organic acids, alcohols, amino acids, and so on by using single-enzymatic or multi-enzymatic reactors, or the production of baker's yeast, food products and additives, recombinant proteins (enzymes and vaccines), and biopolymers by using bioreactors with cell cultures. The mentioned advantages of enzymatic synthesis, and of fermentation using cell cultures, over chemical catalytic processes are shortly underlined in Fig.1**.**

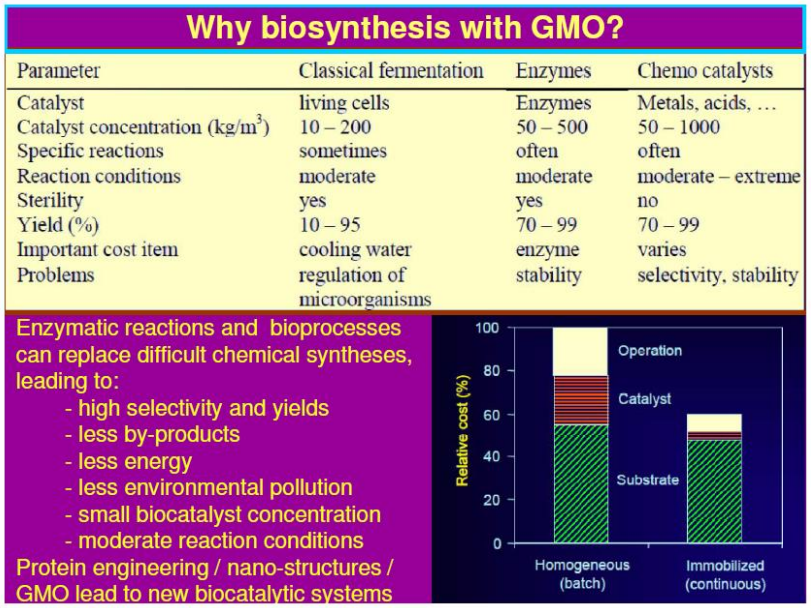

Fig. 1. Advantages of enzymatic synthesis, and of fermentation using cell cultures, over chemical catalytic processes. Structure of the production cost in the case of biosynthesis with free vs. immobilized enzymes

On the other hand, optimization of biological or enzymatic reactors requires adequate kinetic models of the biological / enzymatic process [1, 11]. This is why tremendous experimental and computational efforts have been invested in this respect, despite the high complexity of biological / cellular processes.

Glycolysis is an essential part of the cell metabolism. Glycolysis is the metabolic pathway that converts glucose (GLC) into pyruvate (PYR) (Fig. 2-4, 9). The free energy released by the subsequent tricarboxylic acid cycle (TCA) originating from pyruvate is used to form the high-energy molecules ATP (adenosine triphosphate), and NADH (reduced nicotinamide adenine dinucleotide) that support the glycolysis and numerous enzymatic syntheses into the cell [3].

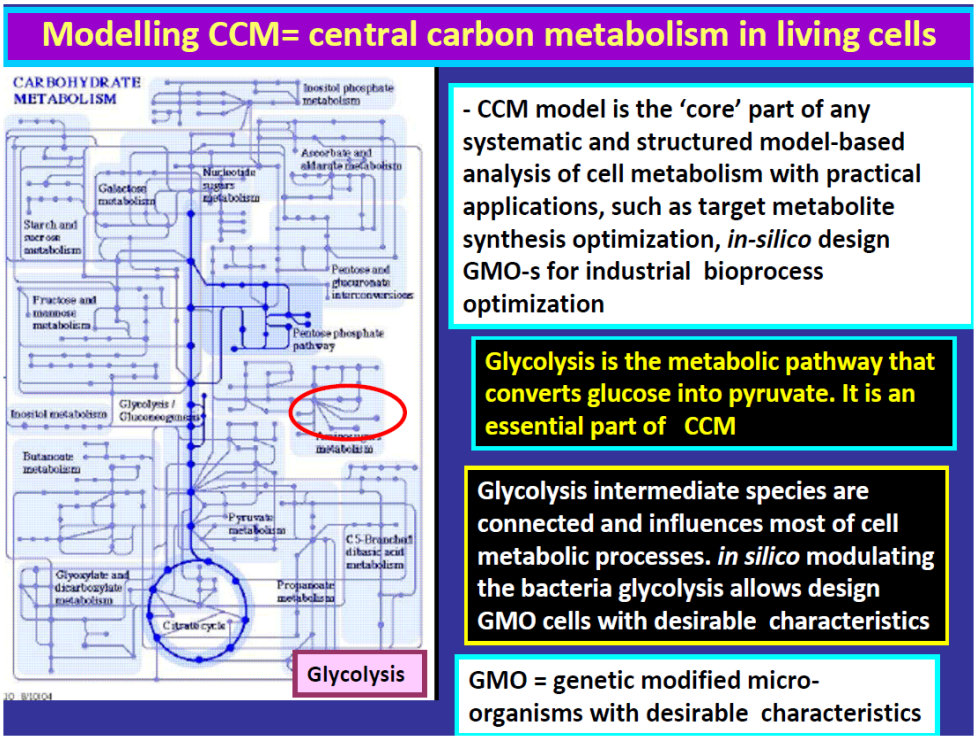

Fig. 2. Glycolysis pathway is the "core" of the CCM [**8**].

In fact, glycolysis, together with the phosphotransferase (PTS)-system for glucose transport into the cell, the pentose-phosphate pathway (PPP), and the tricarboxylic acid cycle (TCA), characterize the central carbon metabolism (CCM) [1,2,4,8] (Fig. 2, 3) which is responsible for all metabolic syntheses. The CCM model is the 'core' part of any systematic and structured model-based analysis of the cell metabolism with immediate practical applications, such as target metabolite synthesis optimization, *in-silico* re-programming of the cell metabolism to design new GMO-s, of practical applications in the biosynthesis industry, environmental engineering, and medicine [1-3]. As glycolysis is connected and influences most of cell metabolic processes, modulating the bacteria glycolysis based on lumped kinetic model is a classical but still of high interest subject [2,5].

By using the lumped dynamic model of Maria [4], this paper is aiming at identifying some conditions allowing modulating the characteristics (oscillation period, species concentration amplitude), of the glycolytic oscillations in *E. coli* cells. [3,5]. Such a model can be used, for instance to maximize the production of amino-acids (**TRP** here) by using immobilized GMO cells in a bioreactor [2].

2. Adopted kinetic model of glycolysis and TRP synthesis in *E. coli* prokaryotic bacteria

The adopted glycolysis kinetic model in *E. coli* (given in Table 2) is those proposed by Maria [4]**,** based on the reaction pathway presented in Fig.4 with the rate expressions given in Figs. 5-7. How glycolytic oscillations occur is shortly explained in section 3.

Aiming to maximize **TRP** production, by modulating the glycolysis characteristics by which **TRP** synthesis is closely connected through the **PEP** node (Fig.9), a **TRP** synthesis kinetic model it is also necessary.

Based on a simplified **TRP** synthesis pathway given in Fig. 9 and extended studies reviewed by **[**2,3,5,7**],** Bhartiya et al.[6] proposed a simplified kinetic model for the **TRP** synthesis given in the Table 4.

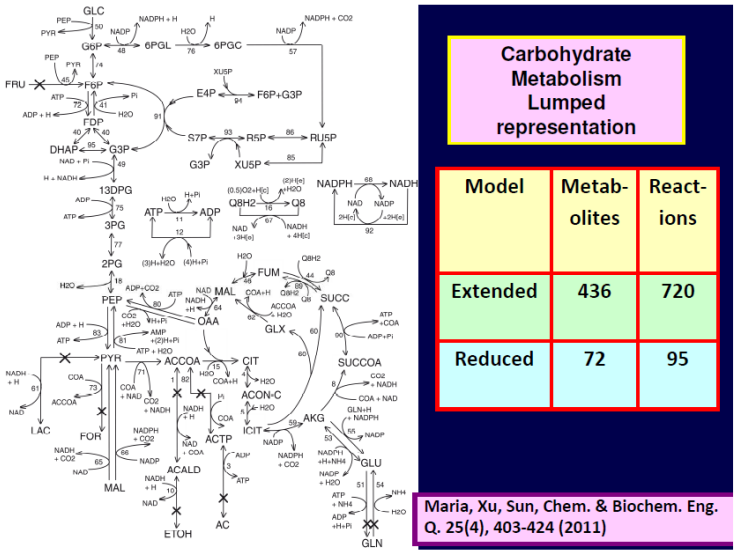

Fig. 3. Glycolysis and carbohydrate metabolism (CCM) model in *E.coli* of [9].

However, this adopted **TRP** model [6] (Table 1) suffered two modifications to match with the Bhartiya [6] experimental data, as suggested by Maria et al. [7]: I) The rate constant k_4 was re-estimated in order to fit the experimental curves of [6], that is the **OR**, **mRNA**, **T, E** species trajectories given in Figure 9 **(**stationary [**PEP]**s = 1 mM case), by using a classic estimator [7] and, II) To be connected to the glycolysis pathway (as displayed in Fig. 9), the **TRP** synthesis kinetic model of Table 4, was completed with terms accounting for the connection with the glycolysis through **PEP** node, **PEP** being explicitly included in the **TRP** synthesis rate (see the dc_T / dt term in Table 4; the nitrogen source in

the **TRP** balance is considered in excess and included in the k_4)[2-7]. Parameter estimation has been done by using the effective MMA of Maria [16].

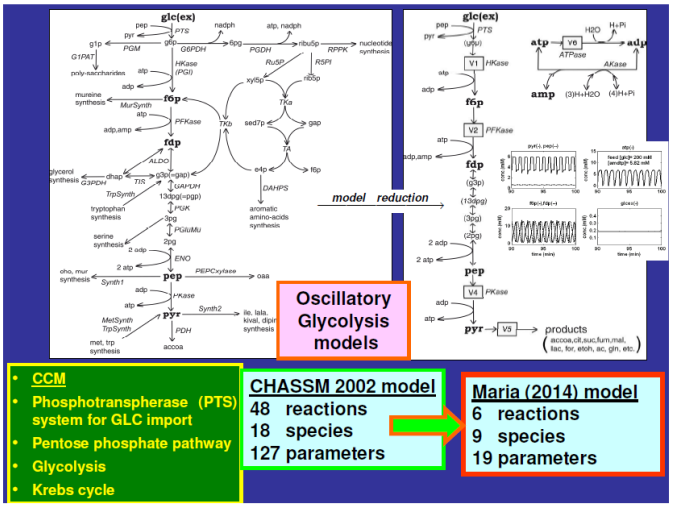

Fig. 4. A comparison of the glycolysis models of [10], and of [4]. The last one allows simulating glycolytic oscillations.

3. How glycolytic oscillations occur and simulation of some oscillation conditions

How glycolytic oscillations occur? Oscillations in chemical systems represent periodic state variable (i.e. species concentrations) transitions in time. According to Franck [12], spontaneous occurrence of self-sustained oscillations in chemical systems is due the coupled actions of at least two simultaneous processes. Oscillations sourced in a so-called “oscillation node” (that is a chemical species, or a reaction), on which concomitant rapid positive (perturbing) and slow negative (recovering) regulatory loops act. Because the coupling action between the simultaneous processes is mutual, the total coupling effect actually forms closed feedback loops for each kinetic variable involved. There exists a well-established set of essential thermodynamic and kinetics prerequisites for the occurrence of spontaneous oscillations [12].

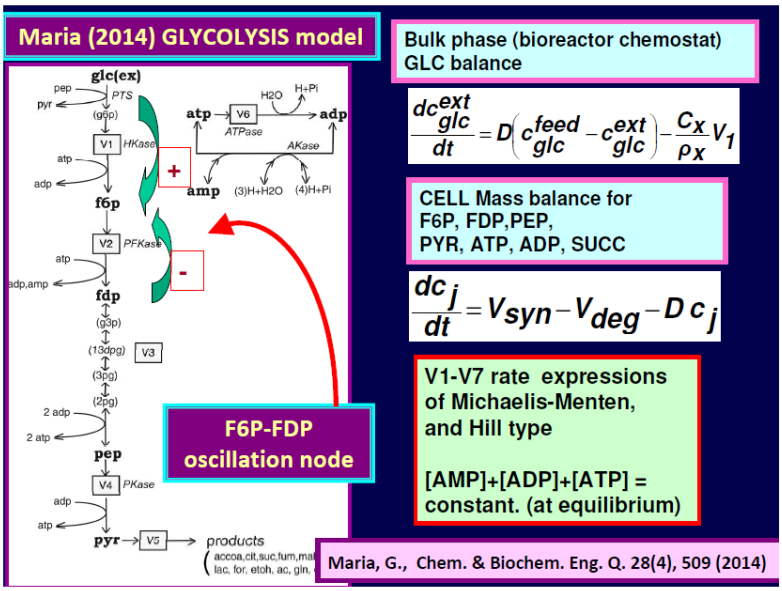

Fig. 5. Explanation of the regulatory loops simultaneously acting on the reaction V2, that produce glycolytic oscillations [3-5].

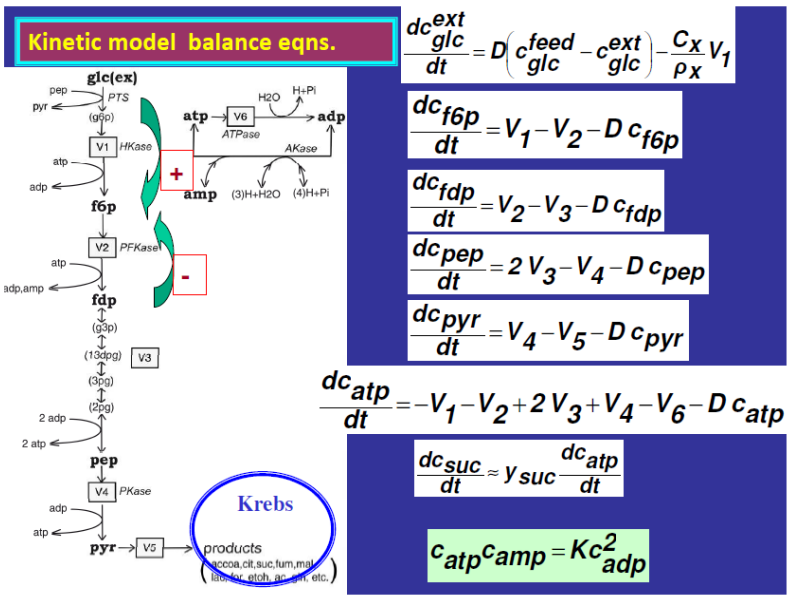

Fig. 6. The differential mass balance of the glycolysis kinetic model [4].

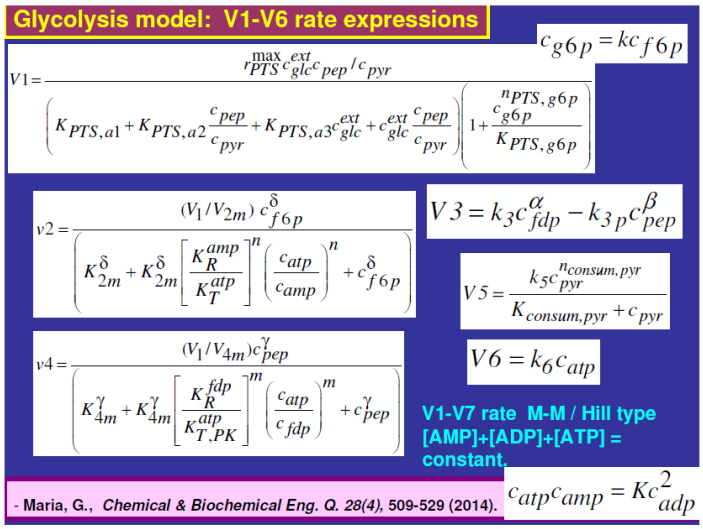

Fig. 7. Reaction rate expressions of the glycolysis kinetic model [4].

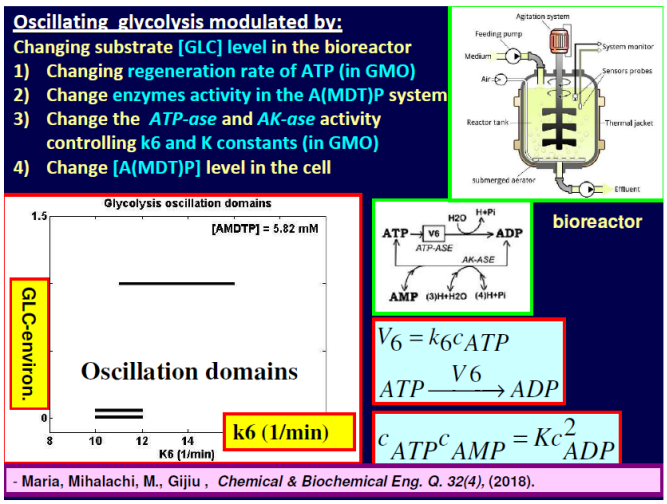

Fig. 8. Some oscillation domains of the glycolysis in *E. coli* in-silico simulated by using Maria [4] model. Suggestions to design GMO to modulate glycolytic oscillations [2,3,5]).

In the glycolysis case, as revealed by Termonia and Ross [13-15], glycolytic oscillations occurrence is due to the antagonistic action of two processes on regulating the V2 reaction rate that converts **F6P** in **FDP** (see reaction scheme in the Figs. 4-6). The glycolytic oscillation occurrence and characteristics (period, amplitude) are influenced by both external (environmental) and internal (genomic) factors [3, 4].

4. Bioreactor and cellular bioprocess structured model coupling glycolysis and TRP (tryptophan) synthesis in the *E. coli* cell

By adopting the glycolysis kinetic model of Maria [4], one can determine, by repeated simulations, the cell external and internal conditions leading to glycolytic oscillation occurrence, and conditions determining **TRP** synthesis maximization. In simulations, one considers the *E. coli* cell growing conditions of the semi-continuous bioreactor of Chassagnole et al. [10], given in Table 1 by using sparking air in excess, and necessary nutrients (for a cell culture equilibrated growth). The main mass balance equations of the bioreactor and glycolysis dynamic model are presented in Tables 2-3. To obtain the model solution with enough precision, a low-order stiff integrator ("ODE23S" routine) of the Matlab™ package was used.

Table 1

Nominal operating conditions of the tested semi-batch bioreactor (SBR) [2].

Parameter	Nominal value	Obs.
Biomass concentration (C_x)	8.7 gDW L^{-1} culture volume	adopted
Cell content dilution rate (μ)	$0.278 \times 10^{-4} - 1.667 \times 10^{-3}$ min^{-1} (adjusted to be identical to D)	To be optimized
Culture dilution rate, $D = F_L/V_L$	$0.278 \times 10^{-4} - 1.667 \times 10^{-3}$ min^{-1} (adjusted to be identical to μ)	To be optimized
Glucose feeding solution concentration C_{GLC}^{feed}	100–200, mM	200–400, mM (this paper).
Initial glucose concentration in the bioreactor $C_{GLC}^{ext}(t = 0)$	0.0557, mM (stationary value of Chassagnole et al., 2002)	1–5 mM (this paper)
Biomass density (ρ_x)	565.5 gDW (L cytosol)$^{-1}$	565.5 gDW (L cytosol)$^{-1}$
Measured [**AMDTP**]total	5.82 (mM)	5.82 (mM)

5. Simulation results

Simulations were made for the cell culture conditions given in Table 1**,** and for cells with [AMDTP]total = 5.82 mM.[3] Following the discussion in the previous chapter on oscillations occurrence, the influence of two main factors is studied here, that is:

i) [Glc]ext (related to the bioreactor operating conditions);
ii) $\boldsymbol{k_6}$ reaction rate (determined by the *ATP-ase* characteristics, related to the cell phenotype),
iii) all other reaction rate constants, and [AMDTP] level were kept unchanged during simulations of values given in Tables 2-3.

Simulations were conducted in an exhaustive way, by covering the ranges of the initial [Glc]ext = [0.01-1] mM (at $\boldsymbol{t = 0}$), and $\boldsymbol{k_6}$ = [0.1-20] 1/min. The results are plotted in Fig. 8. These simulation results lead to several model-based conclusions:

I) Oscillations are basically determined by the external level of [Glc] (triggering the glucose import into the cell) but also, for a certain [AMDTP], total energy

resources level in the cell (assumed to be quasi-constant in the present case study), are determined by the ATP to ADP conversion rate, and ATP regeneration rate (reflected here by k_6, and K constants of Table 2).

Table 2.

The glycolysis kinetic model of Maria [4] and its parameters.

Reaction	Parameters
$GLC + PEP \rightarrow F6P + PYR$ $PYR + ATP \rightarrow PEP + ADP + H$ $GLC + ATP \rightarrow F6P + ADP + H$	$c_{G6P} = kc_{F6P}$;
$V_1 = r_{PTS} = \frac{\rho_X}{C_X} \cdot \frac{r_{PTS}^{max} c_{GLC}^{ext} c_{PEP}/c_{PYR}}{\left(K_{PTS,a1} + K_{PTS,a2}\frac{c_{PEP}}{c_{PYR}} + K_{PTS,a3} c_{GLC}^{ext} + c_{GLC}^{ext}\frac{c_{PEP}}{c_{PYR}}\right)\left(1 + \frac{c_{G6P}^{n_{PTS,G6P}}}{K_{PTS,G6P}}\right)}$	$r_{PTS}^{max} = 308.8587$ $K_{PTS,a1} = 1.0260$ $K_{PTS,a2} = 3740.091$ $K_{PTS,a3} = 5911.072$ $K_{PTS,G6P}$ = absent $n_{PTS,G6P} = 0$
$F6P + ATP \rightarrow FDP + ADP + H$ $V_2 = r_{PFK} = \frac{(V_1/V_{2m})c_{F6P}^{\delta}}{\left(K_{2m}^{\delta} + K_{2m}^{\delta}\left[\frac{K_R^{AMP}}{K_T^{ATP}}\right]^n \left(\frac{c_{ATP}}{c_{AMP}}\right)^n + c_{F6P}^{\delta}\right)}$	$k = 5.8$ $\delta = 1.0437$ $V_{2m} = 0.062028$ $K_{2m} = 6.16423$ $K_R^{AMP} = 25\ \mu M$ $K_T^{ATP} = 60\ \mu M$
$FDP + 2ADP(+2NAD + 2P) \Leftrightarrow 2PEP + 2ATP(+2NADH + 2H + 2H2O)$ $V_3 = k_3 c_{FDP}^{\alpha} - k_{3p} c_{PEP}^{\beta}$	$k_3 = 73.63477$ $k_{3p} = 337.0371$ $\alpha = 0.05$ $\beta = 3$
$PEP + ADP + H \rightarrow PYR + ATP$ $V_4 = r_{PK} = \frac{(V_1/V_{4m})c_{PEP}^{\gamma}}{\left(K_{4m}^{\gamma} + K_{4m}^{\gamma}\left[\frac{K_R^{FDP}}{K_{T,PK}^{ATP}}\right]^m \left(\frac{c_{ATP}}{c_{FDP}}\right)^m + c_{PEP}^{\gamma}\right)}$	$\gamma = 1.33188$ $m = 4$ $V_{4m} = 0.13336$ $K_{4m} = 1.14644$ $K_R^{FDP} = 0.2$ Mm $K_{T,PK}^{ATP} = 9.3$ mM
$PYR \rightarrow products$ (ACCOA, CIT, SUCC, LAC, ETOH, AC, ...) $V_5 = \frac{k_5 c_{PYR}^{n_{consum,PYR}}}{K_{consum,PYR} + c_{PYR}}$	$k_5 = 693.3544$ $K_{consum,PYR} = 395.525$ $n_{consum,PYR} = 2.68139$
$ATP \rightarrow ADP + H$ $V_6 = k_6 c_{ATP}$	$k_6 = 12$ (can vary in the range of 0.1–4000)
Obs.: k_6 takes values according to the micro-organism phenotype (characteristics of the gene encoding the enzyme *ATPase* that catalyse this reaction).	
$2ADP \Leftrightarrow ATP + AMP$ $c_{ATP} c_{AMP} = K c_{ADP}^2$	$K = 1$
Obs.: Termonia and Ross (1981a, 1981b, 1982) indicated experimental evidence of a very fast reversible reaction catalysed by *AKase*, the equilibrium being quickly reached.	

II) Oscillations occur for <u>low</u> [Glc]ext but with a slow Glc import, due to relatively low k_6 constant values (i.e., a cell with a slow ATP conversion to ADP and ATP recovery);

III) By contrast, <u>high</u> levels of [Glc]ext, triggering high rate import, also produce glycolytic oscillations for larger values of k_6, due to the limited ATP recovery rate (k_6 being also related to the K constant governing the AMDTP pathway). Eventually, for too small, or too large k_6 values, the glycolysis reaches its steady-state.

Table 3

The dynamic model of the semi-continuous bioreactor of Maria et al. [2] and its parameters

(A) Species mass balance (glycolysis)	Auxiliary relationships, and parameters of Maria (2014), Maria et al. (2018a).
$\frac{dc_{GLC}^{ext}}{dt} = D(c_{GLC}^{feed} - c_{GLC}^{ext}) - \frac{C_x}{\rho_x}V_1$	
$\frac{dc_{F6P}}{dt} = V_1 - V_2 - \mu\, c_{F6P}$	i) Cell species initial concentrations are those measured by Chassagnole et al. (2002), that is (in mM):
$\frac{dc_{FDP}}{dt} = V_2 - V_3 - \mu\, c_{FDP}$	
$\frac{dc_{PYR}}{dt} = V_4 - V_5 - \mu\, c_{PYR}$	
	$c_{GLC}^{ext}(t=0) = 0.0557$ mM [reference value of Chassagnole et al. (2002), or 1–5 mM (this paper)]
	$c_{F6P}(t=0) = 0.600325977$,
	$c_{FDP}(t=0) = 0.272961814$,
	$c_{PEP}(t=0) = 2.67294507$
	$c_{PYR}(t=0) = 2.67061526$
	$c_{ATP}(t=0) = 4.27$
	ii) $c_{AMP} + c_{ADP} + c_{ATP} = c_{AMDTP}$ = constant (Termonia and Ross, 1981a, 1981b, 1982);
$\frac{dc_{ATP}}{dt} = -V_1 - V_2 + 2V_3 + V_4 - V_6 - \mu\, c_{ATP}$	iii) c_{ADP} results from solving the thermodynamic equilibrium relationship $c_{ATP}c_{AMP} = Kc_{ADP}^2$, that is: $c_{ADP}^2\frac{K}{c_{ATP}} + c_{ADP} - c_{AMDTP} + c_{ATP} = 0$
	iv) Products formation from **PYR** has been neglected in the model;
	v) Biomass concentration (C_x) is assumed to be quasi-constant.
	vi) D= bioreactor dilution.; μ = cell content dilution rate.
$\frac{dc_{PEP}}{dt} = 2V_3 - V_4 - \mu\, c_{PEP} - y_{trp}(2V_3)$	Completion with terms accounting for the PEP consumption in the TRP synthesis: $y_{trp} = {}^{r_{syn,trp}}/_{r_{syn,pep}} = 1/43.63$ (at **QSS**), from(Stephanopoulos and Simpson, 1997).

Table 4

TRP synthesis kinetic model [6] coupled with the glycolysis kinetic model [4] through PEP node [2,5].

(B) Species mass balance (TRP synthesis)	Parameters (Bhartiya et al., 2006)
$\frac{dc_{OR}}{dt} = k_1 c_{OT} C_1(T) - k_{d1}\, c_{OR} - \mu\, c_{OR}$	
$\frac{dc_{MRNA}}{dt} = k_2 c_{OR} C_2(T) - k_{d2}\, c_{MRNA} - \mu\, c_{MRNA}$	Initial values:
$\frac{dc_E}{dt} = k_3\, c_{MRNA} - \mu\, c_E$	
$\frac{dc_T}{dt} = k_4 c_{PEP} C_3(T)\, c_E - \frac{gT}{T+K_g} - \mu\, c_T$	
(the **PEP** term in the right side is accounting for the connection of **TRP** synthesis with the glycolysis)	$c_{OR}(t=0) = 0.01$, μM
	$c_{MRNA}(t=0) = 0.01$, μM
	$c_E\ (t=0) = k_3 c_{MRNA,o}/\mu$, μM
	$c_T\ (t=0) = 0.01$, μM
	$k_1 = 50$, 1/min.; $c_{OT} = 3.32$; nM
	$k_{d1} = 0.5$, 1/min.;
$C_1(T) = \frac{K_{i,1}^{n_H}}{K_{i,1}^{n_H} + T^{n_H}}$;	$k_4 = 0.059$; 1/min (Maria et al. (2018a)
$C_2(T) = \frac{K_{i,2}^{1.72}}{K_{i,2}^{1.72} + T^{1.72}}$	$g = 25$, μM/min.; $K_g = 0.2$, μM
	$k_2 = 15$, 1/min; $k_{d2} = 15$, 1/min
$C_3(T) = \frac{K_{i,3}^{1.2}}{K_{i,3}^{1.2} + T^{1.2}}$	$K_{i,1} = 3.53$, μM; $K_{i,2} = 0.04$, μM
	$K_{i,3} = 810$, μM; $n_H = 1.92$
	μ = Cell content dilution rate.
Obs. The nitrogen source in the **TRP** synthesis is considered in excess and included in the k_4 constant. To be connected to the glycolysis kinetic model, the **PEP** concentration kinetic trajectory generated by the glycolysis model was explicitly included in the **TRP** synthesis rate. Notations: **OR** = the complex between **O** and **R** (aporepressor of the **TRP** gene); **OT** = total TRP operon; **MRNA** = tryptophan mRNA during its encoding gene dynamic transcription, and translation; **E** = enzyme anthranilate synthase; **T** = **TRP** = tryptophan.	

IV) By contrast, high levels of [Glc]ext, triggering high rate import, also produce glycolytic oscillations for larger values of $\boldsymbol{k_6}$, due to the limited ATP recovery rate ($\boldsymbol{k_6}$ being also related to the ***K*** constant governing the AMDTP pathway). Eventually, for too small, or too large $\boldsymbol{k_6}$ values, the glycolysis reaches its steady-state.

V) The glycolytic oscillation domains in Fig. 8, plotted in terms of k_6 and [Glc]ext, are very narrow, revealing their high sensitivity with respect to the inducing factors, and their poor stability. As expected, such a result indicates that oscillations stability is also dependent on the micro-organism characteristics. For instance, by contrast, the glycolytic oscillations in yeast have been proved [3] to be very robust even in the presence of environmental noise, "oscillations being a side-effect of the trade-offs between robustness and regulatory efficiency of the feedback control of the auto-catalytic reaction network".

Simulation of the bioreactor dynamics with including coupled glycolysis and **TRP** kinetics models, revealed several conclusions relevant for TRP production maximization [2]:

I) The glucose initial concentration in the bioreactor, and its concentration in the feeding solution do not influence quantitatively the bioreactor performances (see Fig. 10);

II) On the contrary, the **TRP** production is strongly influenced by the bioreactor dilution. The maximum **TRP** production reaches the value of 0.47 (micro-M/min) for certain operating conditions ([GLC]o = 1 mM; dilution rate of 0.0003097 1/min) with quickly amortized oscillations (QAO) for glycolysis, and quasi-steady-state (QSS) regime for TRP synthesis (see Fig. 11)[2].

III) The bioreactor dilution (adjusted to be the same with the cell dilution rate) strongly influences the QSS / OSC (stable oscillations) regime of the cell bioprocess.

IV) In all cases, it is worth noting the firm evolution of the glucose level in the bulk-phase toward its steady-state (Fig. 10).

V) For the all set points investigated here and by [2], it is to remark the strong influence of the dilution (i.e. bioreactor dilution taken equal to the cell dilution) on the oscillatory behavior of the two cell sub-processes. While the glycolytic species present stationary or amortized oscillations, the **TRP** synthesis oscillations are very stable, even if of small amplitude, tending to QSS under some glycolytic/bioreactor conditions.

VI) Of course, other variables, not accounted in the model (cell characteristics reflected in the model constants) can influence the location of the problem solution. Subsequent experimental checks can validate this problem solution and, eventually, in the case of inconsistencies, they will lead to the model updating/completions for correcting its adequacy in order to perform futures bioreactor optimization analyses.

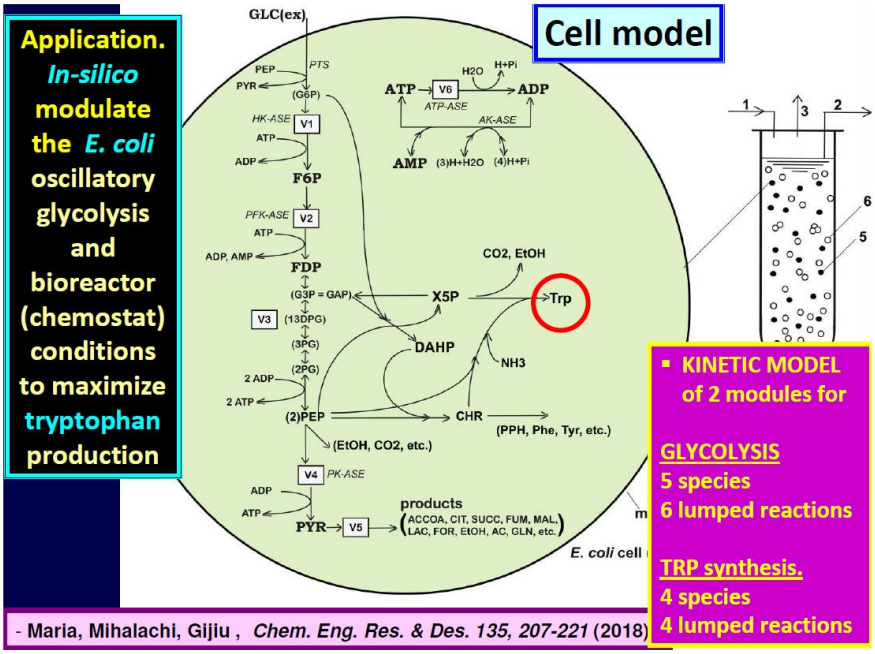

Fig. 9. Reaction pathway of glycolysis coupled with the **TRP** synthesis [2]. **TRP** synthesis kinetic model [6] coupled with the glycolysis kinetic model [4] through **PEP** node [2,5].

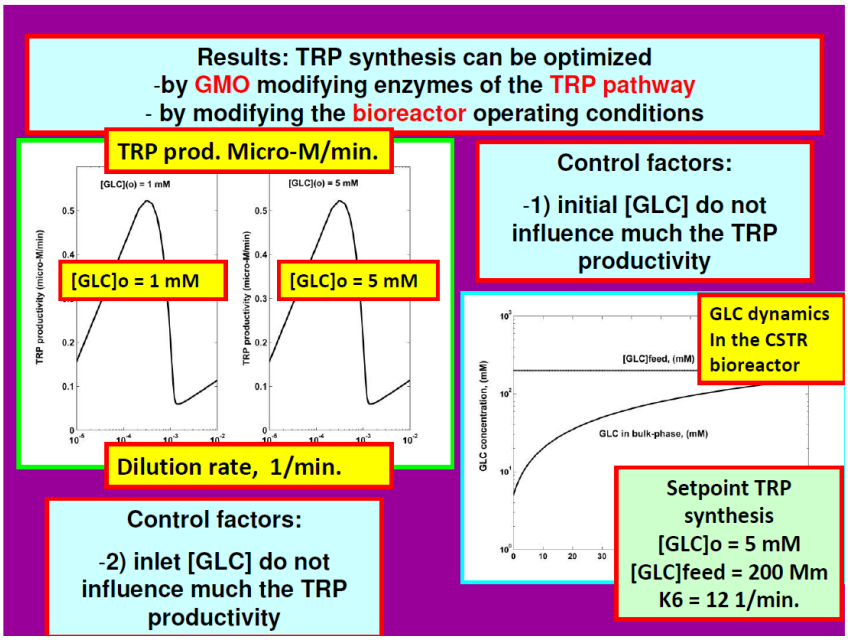

Fig. 10. In-silico evidence that tryptophan synthesis productivity is not influenced by the initial or inlet concentrations of glucose in the chemostat [2,3,5].

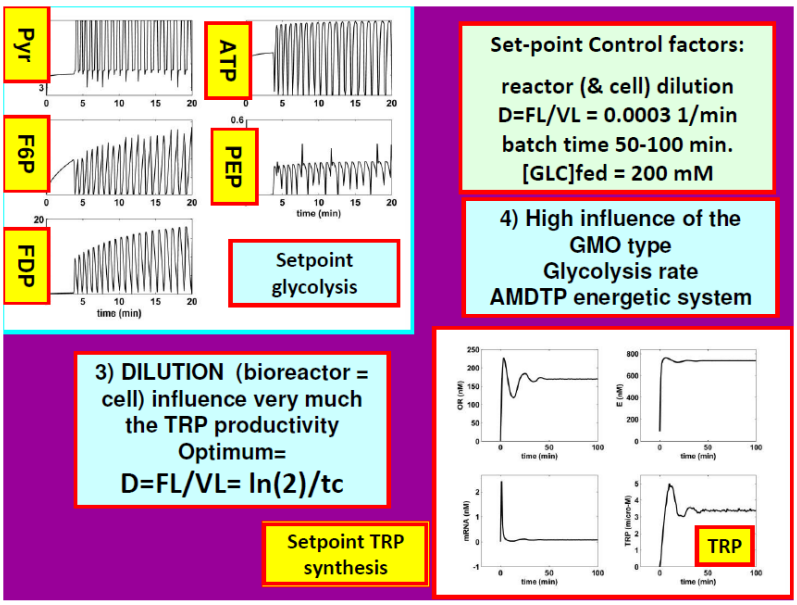

Fig. 11. In-silico determination of the optimal set-point (bioreactor and cell dilution) leading to maximization of the tryptophan synthesis [2,3,5].

6. Conclusions

The use of reduced kinetic models when modelling complex metabolic pathways is a continuous challenging subject when developing structured cell simulators for various applications (flux analysis, target metabolite synthesis optimization, *in-silico* re-programming of the cell metabolism and design of new micro-organisms, bioreactor / bioprocess optimization)[1]. As exemplified by the present case study, concerning *E. coli* glycolysis influence on the **TRP** synthesis, reduced kinetic models, of simple and easily adaptable structure to various cell cultures, can successfully be used for quick analyses of cell metabolism, such as the substrate utilization, oscillation occurrence, or structured interpretation of metabolic changes in modified cells.

The obtained results in the present paper prove, in a simple, but eloquent way that, beside cell phenotype characteristics (determinant for the **TRP** operon expression, and for the **ATP** regeneration engine), glycolysis is one of the major factors determining the **TRP** synthesis efficiency, and **TRP** maximization. So, to maximize the cell **TRP** production, glycolysis should be modulated to increase its speed.

This paper also proves in a relatively simple, yet eloquent way, how a lumped, but enough detailed and adequate dynamic model of essential cell metabolic processes (CCM) can support *in silico* engineering evaluations, if the

cell nano-scale metabolism (including metabolic by-products) will be somehow reflected by the bioreactor macro-scale dynamic model [2,3,7].

Acknowledgment. First author is grateful for the participation grant to the 21th Romanian International Conference on Chemistry and Chemical Engineering offered with generosity by the Romanian Chemical Engineering Society.

Abbreviations and notations

13DPG, PGP	1,3-diphosphoglycerate	Glc, GLC	glucose
2PG	2-phosphoglycerate	GLCex, GLC(ex)	Glucose in the environment
3PG	3-phosphoglycerate	GLN	glutamine
AC	acetate	GRC	genetic regulatory circuits
AA	amino-acid	H	Hydrogen radical
ACCOA	acetyl-coenzyme A	HK-ase	hexokinase
AK-ase	adenylate kinase	LAC	lactate
AMDTP	adenosin-(mono)(di)(tri)phosphate lump	MAL	malate
ADP	adenosin-diphosphate	mM	Milli-molar
AMP	adenosin-monophosphate	MRNA	tryptophan mRNA during its encoding gene dynamic transcription, and translation
ATP	adenosin-triphosphate	NAD(P)H	nicotinamide adenine dinucleotide (phosphate) reduced
ATP-ase	ATP monophosphatase	O	**TRP** active gene
CCM	central carbon metabolism	OR	the complex between **O** and **R** (aporepressor of the **TRP** gene)
CIT	citrate	OT	total **TRP** operon
CHR	chorismat	P, Pi	Phosphoric acid
DAHP	3-Deoxy-D-arabino-heptulosonic acid 7-phosphate	PEP	phosphoenolpyruvate
DHAP	dihydroxyacetonephosphate	PFK-ase	phosphofructokinase
DW	dry-weight	PK-ase	pyruvate kinase
E	enzyme anthranilate synthase	Phe	Phenylalanine
ETOH	ethanol	PPP	pentose-phosphate pathway
F6P	fructose-6-phosphate	PPH	prephenate
FAD	Flavin adenine dinucleotide	PTS	phosphotransferase, or phosphoenolpyruvate: glucose phosphotransferase system

FADH	semiquinone form of the reduced FAD	PYR	pyruvate
FADH2	hydroquinone form of the reduced FAD	QSS	quasi-steady-state
FDP	fructose-1,6-biphosphate	R	aporepressor of the **TRP** gene
FOR	formate	SUCC, SUC	succinate
G3P, GAP	glyceraldehyde-3-phosphate	TCA	tricarboxylic acid cycle
G6P	glucose-6-phosphate	TF	transcription factors
GKase	glucokinase	T, TRP	tryptophan
GERM	gene expression regulatory module	Tyr	Tyrosine
		X5P	Xylulose 5-phosphate
c_j	species *j* concentration	**Indices**	O =initial; syn= synthesis
D	cell content dilution rate	Index s	Stationary (quasi-steady-state)
k_j , K_j	rate constants	y_{trp}	stoichiometric coeff.
t , t_c	Time, Cell cycle	**Super-script**	n = reaction order
QAO	quickly amortized oscillations	OSC	stable oscillations

REFFERENCES

[1] Maria, G., (2018), *In-silico design of Genetic Modified Micro-organisms of industrial use, by using Systems Biology and (Bio)Chemical Engineering tools*, Juniper publ., California (USA), ISBN 978-1-946628-12-1.

[2] Maria, G., Mihalachi, M., Gijiu, C.L., ., *In silico* optimization of a bioreactor with an *E. coli* culture for tryptophan production by using a structured model coupling the oscillating glycolysis and tryptophan synthesis, *Chem. Eng. Res. Design*, 135, (2018), 207-221.

[3] *M*aria, G., Mihalachi, M., Gijiu, C.L.,, Model-based identification of some conditions leading to glycolytic oscillations in *E. coli* cells, *Chem. Biochem. Eng. Q.*, 32, (2018), 523-533.

[4] *M*aria, G., In-silico derivation of a reduced kinetic model for stationary or oscillating glycolysis in *Escherichia coli* bacterium, *Chem. Biochem. Eng. Q*., 28**,** (2014), 509-529.

[5] Mihalachi, M., Maria, G., Influence of pep glycolytic precursor on tryptophan synthesis dynamics in *e. coli* cells, *U.P.B. Sci. Bull., B - Chemie*, 81(2), (2019), 29-36.

[6] Bhartiya, S., Chaudhary, N., Venkatesh, K.V., Doyle III, F.J., Multiple feedback loop design in the tryptophan regulatory network of *Escherichia coli* suggests a paradigm for robust regulation of processes in series. *J. R. Soc. Interface***,** 3 (2006), 383–391.

[7] Maria, G., Gijiu, C.L., Maria, C., Tociu, C., Interference of the oscillating glycolysis with the oscillating tryptophan synthesis in the *E. coli* cells, *Computers & Chemical Engineering*, 108 (2018), 395-407.

[8] KEGG PATHWAY. (2011), Phenylalanine, tyrosine and tryptophan biosynthesis; Kyoto encyclopedia of genes and genomes, Kanehisa Laboratories, Bioinformatics Center of Kyoto University, http://www.kegg.jp/kegg-bin/show_pathway?

[9] Edwards, J.S., Palsson, B.O., Proc Natl Acad Sci U S A. 97 (10), (2000), 5528-5533.

[10] Chassagnole, C., Noisommit-Rizzi, N., Schmid, J. W., Mauch, K., Reuss, M., *Biotechnology and Bioengineering*, 79**,** 53 (2002). http://dx.doi.org/10.1002/bit.10288.

[11] Maria, G., (2017), *Deterministic modelling approach of metabolic processes in living cells - a still powerful tool for representing the metabolic process dynamics*, Juniper publ., Newbury Park, California 91320, (USA), ISBN 978-1-946628-07-7(USA). https://juniperpublishers.com/ebook-info.php.

[12] U.F. Franck, Feedback kinetics in physicochemical oscillators, Ber. Bunsenges. *Phys. Chem.* 84, (1980), 334-341.

[13] Y. Termonia, J. Ross, J., Oscillations and control features in glycolysis: Numerical analysis of a comprehensive model, *Proceedings of the National Academy of Sciences* of the USA, 78**,** (1998), 2952-2956.

[14] Y. Termonia, J. Ross, Oscillations and control features in glycolysis: Analysis of resonance effects, *Proceedings of the National Academy of Sciences* of the USA, 78, (1981), 3563-3566.

[15] Y. Termonia, J. Ross, Entrainment and resonance in glycolysis, *Proceedings of the National Academy of Sciences* of the USA, 79, (1982), 2878-2881.

[16] Maria, G.**,** (2003), *ARS combination with an evolutionary algorithm for solving MINLP optimization problems, In: Modelling, Identification and Control*, M.H. Hamza (Ed.), IASTED/ACTA Press, Anaheim (CA), 112-118 (ISBN 0-88986-343-1; http://www.sigmod.org/sigmod/dblp/db/conf/mic/mic2003.html

MATHEMATICAL MODEL FOR FIXED BED SORBENT CHROMATOGRAPHY: CHROMATOGRAPHIC SEPARATOR

Tănase DOBRE, Oana Cristina PÂRVULESCU*,
Cristian Eugen RĂDUCANU, Roxana Mihaela LAZAR

Dept. of Chemical and Biochemical Engineering, Faculty of Applied Chemistry and Materials Science, University POLITEHNICA of Bucharest, 1-7 Gh. Polizu Street, 011061, Bucharest, Romania

Abstract

Chromatographic separation is based on the different affinity of the components of a mixture for the stationary and mobile phases. A deterministic model for chromatographic separation of two components using a granular fixed bed as a stationary phase was developed. The species to be separated were adsorbed onto the fixed bed until its saturation (saturation or sorption stage) and then they were desorbed using a fluid as an eluent (elution or desorption stage). The overall sorption rate of components was expressed as a difference between sorption and desorption rates and a plug flow with axial dispersion of mobile phase was assumed. Process dynamics were calibrated based on data reported in the related literature on the sorption/desorption of diosgenin and sclareol onto/from fixed bed imprinted polymer pearls. Good species separability for saturation stage was obtained at low levels of liquid superficial velocity and high values of fixed bed height. To obtain a desired separation in the elution stage, a mobile phase with a higher affinity for a component should be used.

Key words: chromatography, modelling, fixed bed, sorption, elution, imprinted polymer

1. Introduction

The first researches on chromatographic separation were published by the Russian botanist Mikhail Semyonovich Tsvet (also spelled Tswett), who separated plant pigments in a column filled with calcium carbonate [1]. The term of chromatographic elution, introduced by Tadeus Reichstein and Joseph von Euw, refers to the chromatographic separation of sample components by passing them through a stationary phase [2]. From 1937 until now, 12 Nobel prizes have been awarded for researches in which chromatography had an essential role, *e.g.*, Archer John Porter Martin and Richard Laurence Millington Synge won the

* Corresponding author; E-mail: oana.parvulescu@yahoo.com

Nobel Prize in Chemistry (1952) for the invention of partition chromatography [3].

As shown in Fig. 1, the chromatographic separation is based on the different affinity of the components of a sample (mixture) for the stationary phase (packed in a column) and the mobile phase (eluent flowing through the stationary phase). Concentrations of sample components along the column containing the stationary phase (Fig. 1) are shown in Fig. 2. For each mixture component, the surface under the curve that describes the variation of component concentration along the fixed bed is the same whatever the position in the bed (*e.g.*, S_A area in Fig. 2 is the same regardless of position, because this area is proportional to the amount of *A* component in the mixture).

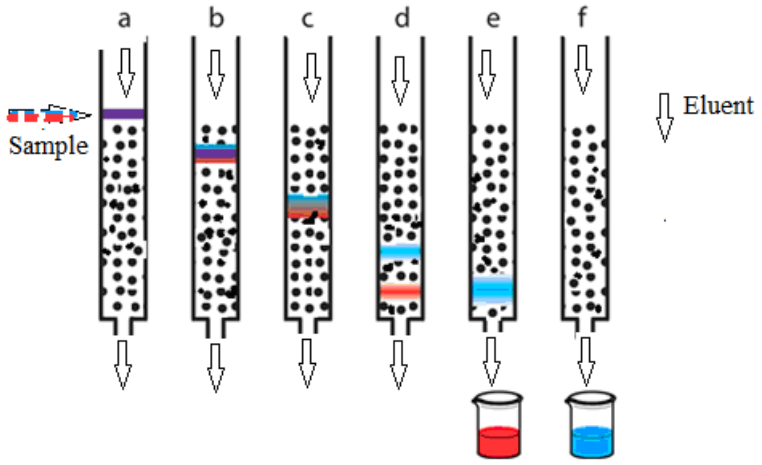

Fig. 1. The principle of chromatographic separation of two components (blue and red) by passing them through a column containing a solid stationary phase which is eluted with a mobile phase.

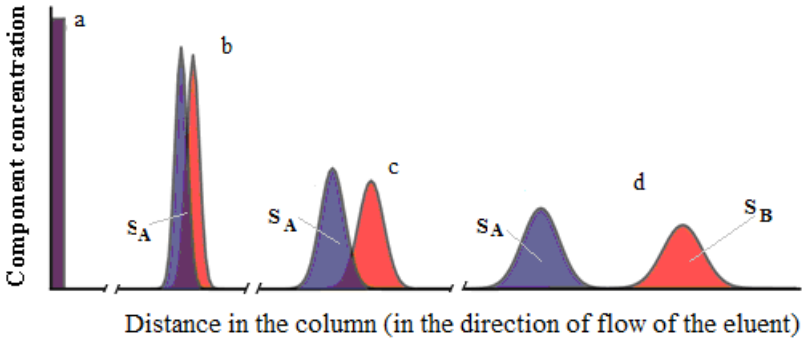

Fig. 2. Concentration of two components of a sample along the column containing the stationary phase.

As the peak of a component is completely separated from the peak of the other component (case *d* in Fig. 2), the composition of the mixture can be calculated by measuring the areas of these peaks. This is the basic principle of chromatographic analysis, a modern instrumental analysis method, which has heavily evolved over the last 10 years [4]. A scheme of a gas chromatograph and a picture of Buck Scientific Gas Chromatograph (Mass Transfer Laboratory, Faculty of Applied Chemistry and Materials Science (FACMS), UPB) are shown in Fig. 3.

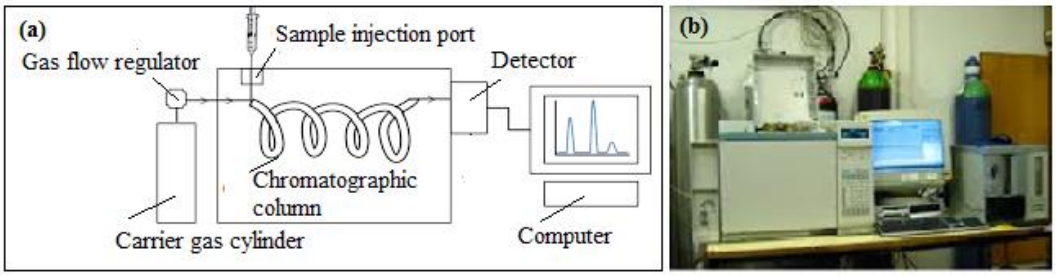

Fig. 3. Scheme of a gas chromatograph (a) and a picture of Buck Scientific Gas Chromatograph (Mass Transfer Laboratory at FACMS, UPB) (b).

Mechanisms of component separation are mainly based on adsorption, ion exchange, and size-exclusion. Often, chromatographic processes can occur through a combination of them.

The present work focuses on the modelling of the chromatographic separation of two compounds using a granular fixed bed as a stationary phase. The compounds to be separated are sorbed onto the fixed bed until its saturation and then they are desorbed using a fluid as an eluent.

2. Modelling

For a stationary phase consisting in fixed bed particles, the model selected to predict *i* (*A* and *B*) species sorption from a mobile phase has been based on the following simplifying assumptions [5-10]:

- plug flow with axial dispersion of mobile phase along the stationary phase;
- a monolayer sorption of *i* species molecules occurs onto the surface of stationary phase particles and pores walls;
- internal and external diffusion resistance is negligible;
- overall sorption rate of *i* species depends on the competition between sorption and desorption processes.

Model equations, initial and boundary conditions for sorption of *i* species from the mobile phase onto stationary phase are as follows [5-10]:

- mass balance equation for *i* species in the mobile phase flowing through the fixed bed:

$$\frac{\partial c_i}{\partial \tau} + w\frac{\partial c_i}{\partial z} = D_{li}\frac{\partial^2 c_i}{\partial z^2} - \frac{\partial c_{Si}}{\partial \tau} \quad (1)$$

- overall sorption rate equation of *i* species:

$$\frac{\partial c_{Si}}{\partial \tau} = k_{ai}\left(1 - \frac{a_1 c_{SA} + a_2 c_{SB}}{Q}\right)c_i - k_{di}c_{Si} \quad (2)$$

- initial conditions:

$$\tau = 0 \qquad 0 < z \le H \qquad c_i = 0 \quad (3)$$

$$\tau = 0 \qquad z = 0 \qquad c_i = c_{i0} \quad (4)$$

- boundary conditions:

$$\tau > 0 \qquad z = 0 \qquad \frac{\partial c_i}{\partial z} = \frac{w}{D_{li}}(c_{i0} - c_i) \quad (5)$$

$$\tau > 0 \qquad z = H \qquad \frac{\partial c_i}{\partial z} = 0 \quad (6)$$

An adequate modification of initial and boundary conditions as well as of model parameters (D_{li}, a_i, k_{ai}, k_{di}, Q, w), transforms the sorption model into the desorption (elution) model of the species retained in the stationary phase [6].

3. Results and discussions

Sorption and elution dynamics are mainly affected by superficial velocity of mobile phase flowing through stationary phase (fixed bed particles), fixed bed height, operating temperature, and characteristic parameters of solid phase [5-16].

Data from the related literature were used to predict the dynamics of sorption process of *i* species from mobile phase onto stationary phase. Table 1 contains values of characteristic parameters of sorption of diosgenin (A) and sclareol (B) from mobile phase (75% vol. alcoholic solution at 25 °C) onto fixed bed imprinted polymer (based on acrylonitrile-acrylic acid copolymer) pearls [5,6]. Axial dispersion coefficient was determined using Eq. 7 [7-10], where w (cm/s) is mobile phase superficial velocity and d_P mean particle diameter (cm).

$$D_{li} = D_l = \frac{w d_P}{2} \quad (7)$$

Graphical representations in Figs. 4-6 show the effects of superficial velocity of mobile phase (w), fixed bed height (H), and initial concentration of B species in the mobile phase (c_{B0}) on the breakthrough curves for fixed bed imprinted polymer pearls. Depicted data emphasize the following issues: (i) a good species separability is obtained at low levels of w and high values of H; (ii) separability efficiency does not depend by the values of c_{B0}; (iii) if the aim is a fast saturation of the fixed bed, *e.g.*, in order to concentrate the processed mixture, then high values of w and H are needed. Species separability in Figs. 4-6 can be quantified by a separability coefficient, $C_{sep,br}$, defined by Eq. 8 as a ratio between the period when a single component exits the fixed bed, τ_1, and the total bed breakthrough time, τ_{br}.

$$C_{sep,br} = \frac{\tau_1}{\tau_{br}} \tag{8}$$

Table 1

Characteristic parameters of sorption of A and B species from mobile phase onto stationary phase

Parameter	Symbol	Unit	Value	Value*
Sorption rate constant	k_{aA}	s^{-1}	2×10^{-2}	2×10^{-2}
	k_{aB}	s^{-1}	3×10^{-2}	3×10^{-2}
Desorption rate constant	k_{dA}	s^{-1}	1×10^{-4}	1×10^{-2}
	k_{dB}	s^{-1}	1×10^{-2}	5×10^{-2}
Constants in Eq. (2)	a_1	-	2×10^{-2}	2×10^{-2}
	a_2	-	3×10^{-2}	3×10^{-2}
Maximum monolayer sorption capacity	Q	mol/L	5×10^{-2}	5×10^{-2}

* mobile phase with higher affinity for A species

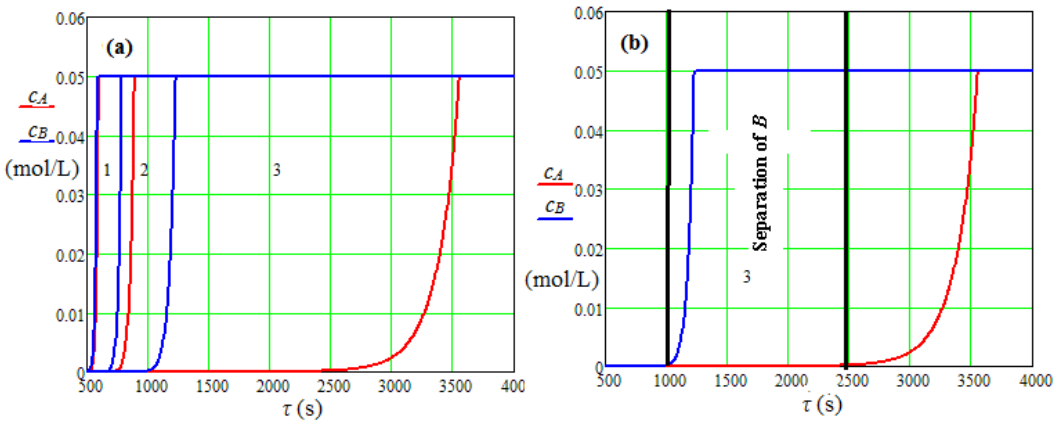

Fig. 4. Effect of superficial velocity of mobile phase on the breakthrough curves (a) and species separability (b) for fixed bed imprinted polymer pearls (H = 10 cm, d_P = 0.1 cm, $c_{A0} = c_{B0}$ = 0.050 mol/L): (1) $w = 5 \times 10^{-2}$ cm/s; (2) $w = 3 \times 10^{-2}$ cm/s; (3) $w = 1.5 \times 10^{-2}$ cm/s.

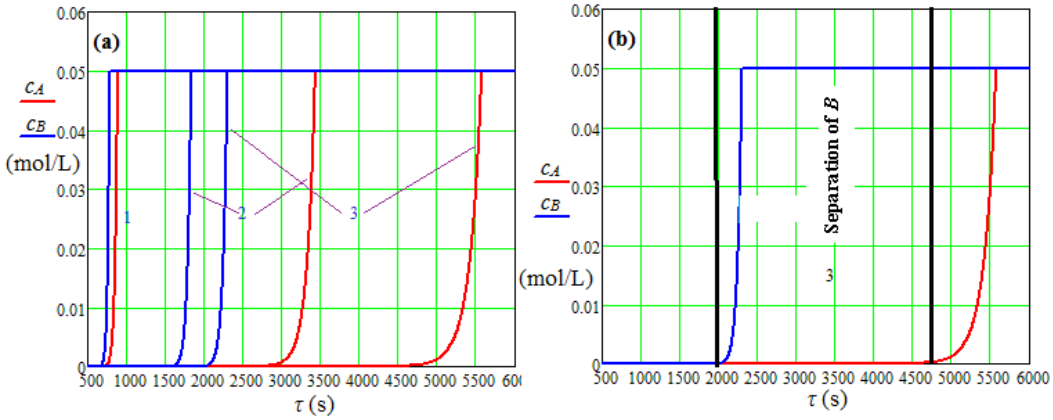

Fig. 5. Effect of fixed bed height on the breakthrough curves (a) and species separability (b) for fixed bed imprinted polymer pearls ($w = 3 \times 10^{-2}$ cm/s, $d_P = 0.1$ cm, $c_{A0} = c_{B0} = 0.050$ mol/L): (1) $H = 10$ cm; (2) $H = 20$ cm; (3) $H = 24$ cm.

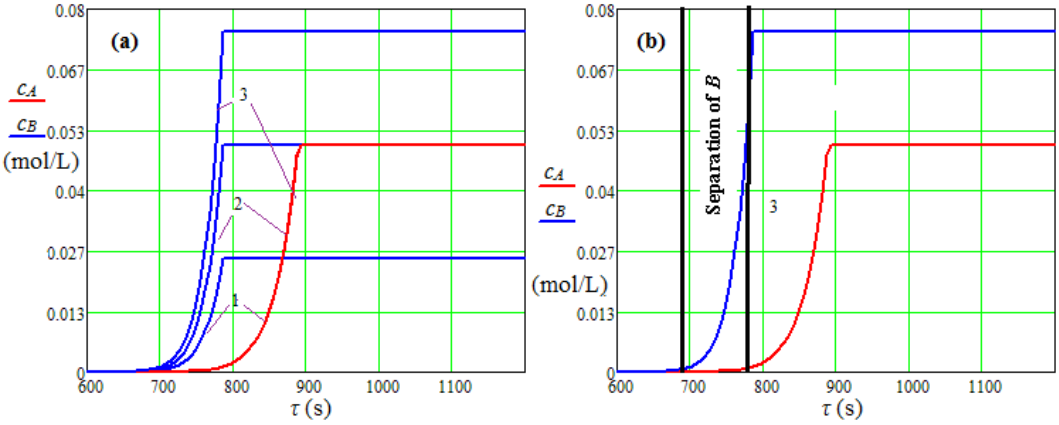

Fig. 6. Effect of initial concentration of *B* species in the mobile phase on the breakthrough curves (a) and species separability (b) for fixed bed imprinted polymer pearls ($H = 10$ cm, $d_P = 0.1$ cm, $c_{A0} = 0.050$ mol/L, $w = 3 \times 10^{-2}$ cm/s): (1) $c_{B0} = 0.025$ mol/L; (2) $c_{B0} = 0.050$ mol/L; (3) $c_{B0} = 0.075$ mol/L.

Plots in Figs. 7 and 8 show the effects of superficial velocity of mobile phase (w) and fixed bed height (H) on the elution curves for fixed bed imprinted polymer pearls. It was considered that the washing of diosgenin and sclareol retained by the stationary phase was performed using either 75% vol. alcoholic solution (the same mobile phase as in the saturation stage) at 65 °C or a mobile phase with higher affinity for A species [5,6]. A separability coefficient, $C_{sep,el}$, is defined by Eq. 9, where τ_{el} is the elution time.

$$C_{sep,el} = \frac{\tau_1}{\tau_{el}} \tag{9}$$

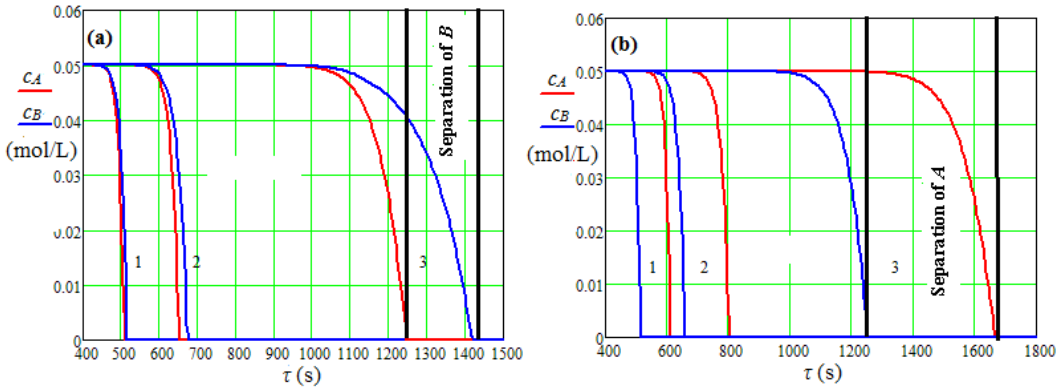

Fig. 7. Effect of superficial velocity of mobile phase on the elution curves for fixed bed imprinted polymer pearls (H = 10 cm, d_P = 0.1 cm, c_{SA0} = 0.014 mol/L, c_{SB0} = 0.048 mol/L):
(1) $w = 5 \times 10^{-2}$ cm/s; (2) $w = 3 \times 10^{-2}$ cm/s; (3) $w = 1.5 \times 10^{-2}$ cm/s ((a) the same mobile phase as in the saturation stage; (b) mobile phase with higher affinity for A species).

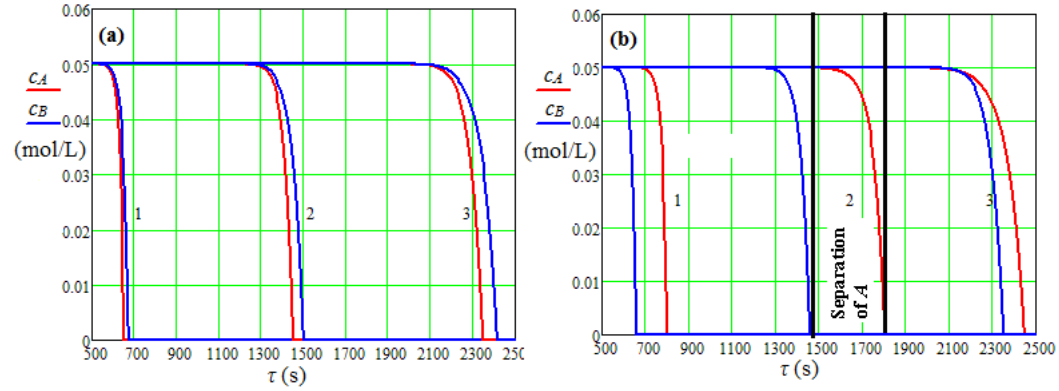

Fig. 8. Effect of fixed bed height on the elution curves for fixed bed imprinted polymer pearls ($w = 3 \times 10^{-2}$ cm/s, d_P = 0.1 cm, c_{SA0} = 0.014 mol/L, c_{SB0} = 0.048 mol/L):
(1) H = 10 cm; (2) H = 20 cm; (3) H = 24 cm ((a) the same mobile phase as in the saturation stage; (b) mobile phase with higher affinity for A species).

Table 2

Values of separability coefficient for breakthrough and elution of stationary phase

Figure	Operating conditions	τ_1 (s)	$\tau_{br/el}$ (s)	C_{sep} (%)
4	H = 10 cm d_P = 0.1 cm $c_{A0} = c_{B0}$ = 0.050 mol/L $w = 1.5 \times 10^{-2}$ cm/s	2500 – 1000 = 1500 (B species)	3600	41.7
5	H = 24 cm d_P = 0.1 cm $c_{A0} = c_{B0}$ = 0.050 mol/L $w = 3 \times 10^{-2}$ cm/s	4750 – 2000 = 2750 (B species)	5600	49.1
6	H = 10 cm d_P = 0.1 cm	775 – 695 = 80 (B species)	900	8.9

	c_{A0} = 0.050 mol/L c_{B0} = 0.075 mol/L $w = 3 \times 10^{-2}$ cm/s			
7a	H = 10 cm d_P = 0.1 cm c_{SA0} = 0.014 mol/L c_{SB0} = 0.048 mol/L $w = 1.5 \times 10^{-2}$ cm/s	1420 –1200 = 220 (B species)	1420	15.5
7b	H = 10 cm d_P = 0.1 cm c_{SA0} = 0.014 mol/L c_{SB0} = 0.048 mol/L $w = 1.5 \times 10^{-2}$ cm/s	1680 – 1200 = 480 (A species)	1680	28.6
8a	H = 20 cm d_P = 0.1 cm c_{SA0} = 0.014 mol/L c_{SB0} = 0.048 mol/L $w = 3 \times 10^{-2}$ cm/s	1500 – 1450 =50 (B species)	1500	3.33
8b	H = 20 cm d_P = 0.1 cm c_{SA0} = 0.014 mol/L c_{SB0} = 0.048 mol/L $w = 3 \times 10^{-2}$ cm/s	1800 – 1480 = 320 (A species)	1800	17.8

4. Conclusions

A model for chromatographic separation involving saturation of stationary phase (saturation or sorption stage) followed by elution with a mobile phase until the total washing of solid phase (elution or desorption stage) was developed. A plug flow with axial dispersion of mobile phase along the stationary phase was assumed. The overall sorption rate of species was expressed as a difference between sorption and desorption rates.

Data from the related literature on the sorption/desorption of diosgenin and sclareol onto/from fixed bed imprinted polymer pearls were used to simulate the process dynamics at various levels of superficial velocity of mobile phase, fixed bed height, and initial concentration of *B* species in the mobile phase.

Characteristic simulations of sorption stage indicated that good species separability was obtained at low levels of superficial velocity and high values of bed height. Moreover, it was proved that separability efficiency for sorption stage did not depend by the values of initial *B* species concentration. In order to obtain a desired separation in the desorption stage, it should be used a mobile phase having a higher affinity for a component.

Nomenclature

a_i constants in Eq. (2)
c_i concentration of *i* species in the mobile phase, g/cm^3
c_{Si} concentration of *i* species in the stationary phase (fixed bed particles), g/cm^3
C_{sep} separability coefficient
d_P mean particle diameter, cm
D_{li} axial dispersion coefficient, cm^2/s
H bed height, cm
$k_{ai/di}$ sorption/desorption rate constant, s^{-1}
Q maximum monolayer sorption capacity, g/cm^3
w superficial velocity of mobile phase, cm/s
z axial distance in the fixed bed, cm

Greek letters
τ time, s

Subscripts
a adsorption
br breakthrough
d desorption
el elution
i component in the mixture
0 initial

REFERENCES

[1] Tswett M.S., On a new category of adsorption phenomena and on its application to biochemical analysis, *Proceedings of the Warsaw Society of Naturalists*, Biology Section, 14(6), (1905), 20-39.
[2] Reichstein T., von Euw J., Chromatography with elution, *Helvetica Chimica Acta*, 21, (1938), 1197-1203.
[3] *** Wikipedia, List of Nobel Laureates in Chemistry, https://en. wikipedia. org/ wiki/ List_of_Nobel_laureates_in_Chemistry.
[4] Gunzler H., Williams A. (Eds.), *Handbook of Analytical Techniques*, Wiley-VCH, Weinheim, 2001.
[5] Dima Ș.O., *Molecularly imprinted polymers for selective separation of bioactives compounds - Synthesis, characterisation, mass transfer and mathematical modelling*, Ph.D. Thesis, University Politehnica of Bucharest, 2013.
[6] Dima Ș.O., Dobre T., Mathematical modelling and simulation of adsorption process in a fixed bed of molecularly imprinted polymeric pearls, *UPB Scientific Bulletin*, Series B, 78(2), (2016), 143-154.
[7] Dobre T., Pârvulescu O.C., Iavorschi G., Stroescu M., Stoica A., Volatile organic compounds removal from gas streams by adsorption onto activated carbon, *Industrial & Engineering Chemistry Research*, 53(9), (2014), 3622-3628.
[8] Dobre T., Pârvulescu O.C., Jacquemet A., Ion V.A., Adsorption and thermal desorption of volatile organic compounds in a fixed bed - Experimental and modelling, *Chemical Engineering Communications*, 203(12), (2016), 1554-1561.

[9] Ion, V.A., Pârvulescu, O.C., Dobre, T., Volatile organic compounds adsorption onto neat and hybrid cellulose, *Applied Surface Science*, 335, (2015), 137-146.
[10] Pârvulescu, O.C., Ion, V.A., Dobre, T., Nițu, S.G., The effect of process factors on n-hexane adsorption onto copper impregnated activated carbon, *UPB Scientific Bulletin*, Series B, 78(2), (2016), 121-130.
[11] Dima Ș.O., Dobre T., Sârbu A., Ghiurea M., Bradu C., Proofs for molecular imprinting of an acrylic copolymer by phase inversion, *UPB Scientific Bulletin*, Series B, 71(4), (2009), 21-30.
[12] Dima Ș.O., Dobre T., Stoica-Guzun A., Oancea F., Jinga S.I., Nicolae C.A., Molecularly imprinted bio-membranes based on cellulose nano-fibers for drug release and selective separations, *Macromolecular Symposia*, 359(1), (2016), 124-128.
[13] Dima Ș.O., Meouche W., Dobre T., Nicolescu T.V., Sârbu A. Diosgenin-selective molecularly imprinted pearls prepared by wet phase inversion, *Reactive and Functional Polymers*, 73(9), (2013), 1188-1197.
[14] Dima Ș.O., Sârbu A., Dobre T., Purcar V., Nicolae C.A, Diosgenin selective molecularly imprinted polymers with acrylonitrile-methacrylic acid matrix, *Materiale Plastice*, 49(2), (2012), 106 -113.
[15] Dobre T., Sanchez Marcano, J., *Chemical engineering - Modelling, simulation and similitude*, Wiley, New York, 2007.
[16] Ion, V.A., Pârvulescu, O.C., Dobre, T., Duțeanu, N., Nițu, S.G., Modelling of thermal desorption of volatile organic compounds from activated carbon, *Revista de Chimie* (Bucharest), 66(5), (2015), 703-706.

CONSIDERATIONS REGARDING THE OPTIMIZATION PROCEDURE OF THE ELECTRODEPOSITION OF NICKEL-COPPER FILMS USED FOR SUPERCAPACITORS AND/OR RECHARGEABLE BATTERIES PLATES

Ioana-Alina CIOBOTARU, Oana-Claudia CIOBOTEA-BARBU, Danut-Ionel VAIREANU*

University POLITEHNICA of Bucharest, Faculty of Applied Chemistry and Materials Science, 1-7 Polizu Street, 011061, Bucharest, Romania

Abstract.

The search for new ways of storing electrical energy, particularly produced from non-constant supplying sources, such as photovoltaic panels and wind generators is continuously expanding. One possible solution would be to employ supercapacitors, which may level the peak output as well as short term increased demands. One of the requirements for producing such supercapacitors is the possibility for a better structural deposition control of the supercapacitor plates, depending on the intended use. This paper presents the results of an optimization procedure applied to the electrodeposition parameters during the manufacture of some nickel-copper alloys intended for the supercapacitor plates use.

Key words: optimization procedure, Ni-Cu electrodeposited films, supercapacitors

1. Introduction

In the recent years, the development of alternative, efficient and sustainable energy sources has been of key importance and efforts have been made to ensure the energy requirements in a fast developing global economy. In the context of decreasing of available fossil fuels and the environmental problems caused by their intense use, the use of alternative energy sources is a prerequisite for sustainable development. However, one of the main issues that need to be addressed as regards energy production is the development of efficient conversion and storage devices. In this purpose, a practical and suitable technology is represented by electrochemical devices, i.e. batteries, fuel cells and electrochemical supercapacitors (SC) [1-4]. The later have been intensively studied over the last 50 years and may represent a viable alternative to

* Corresponding author. Email address: di_vaireanu@yahoo.co.uk

conventional energy storage by means of batteries as their particular structure and surface area may provide the storage of a higher amount of energy and ensure a higher lifespan or as an additional top-up back-up system for overloaded rechargeable batteries [5-9].

Our previous research proved that SC based on Ni-Cu foams [10-13] have high equivalent/specific capacitance. Depending on their application, specific procedures are required for the optimization of the working parameters for the electrodeposition process so that the desired performances of the Ni-Cu coatings are achieved.

In this context, this paper presents a method to identify the optimum values of the parameters for the electrodeposition of nickel-copper layers in order to achieve better equivalent capacitance, pore diameter/bridge thickness ratio and Ni/Cu concentration ratio for different applications.

The actual values of the electrodeposition parameters, namely five current densities, five values for the deposition time and three temperatures of the electrolyte solution, as well as the primary data, were previously published in [10-13], this paper dealing only with the optimization procedure.

2. Experimental

Procedure

The identification of the optimum domains of nickel-copper films electrodeposition so that they exactly correspond to the operating requirements is a step that quantifies the parameters of the obtaining process, in an easily interpretable form. For an easy identification of the optimum fields of the electrodeposition process in order to obtain alloys for different applications types, one may use the contour charts, which allow the delimitation of some well-defined intervals of the parameters that can be used during the electrodeposition process.

In order to obtain the contour charts, one has used the OriginPro 8 software. The data used to draw the contour chart were processed so that the variables are dimensionless, more precisely the values of the considered parameters were normalized by referring to the maximum values of the respective parameters.

The variables used to construct an optimization procedure are:

- Deposition temperature (T) - the value of the temperature used is expressed in K;
- Current density (i), $A \cdot cm^{-2}$;
- Normalized temperature - the ratio between the working temperature value and the maximum temperature value used in the deposition process;

$$\bar{T} = \frac{T}{T\,max} \quad (1)$$

- Current flow (Ø)- the ratio of the value of current density to that of the deposition time, $A \cdot cm^{-2} \cdot s^{-1}$;
- Normalized current flow - the ratio between the average value of the current density and that of the deposition time on its highest value:

$$\bar{\emptyset} = \frac{\frac{i}{t}}{\left(\frac{i}{t}\right)max} \quad (2)$$

- Capacitance (C) - average capacitance values, μF;
- Pore diameter (D_{pore}), μm;
- Bridge thickness (G_{bridge}), μm;
- Nickel content, %;
- Copper content, %;
- Electrical charge (Q), A·s.
- Normalized electrical charge - normalized values of the electric charge obtained from the ratio of the product to the current density value, deposition time and surface reported to its highest value:

$$\bar{Q} = \frac{itS}{(itS)max} \quad (3)$$

The parameters considered relevant for the use of these nickel-copper deposits in the construction of supercapacitors are the deposits composition, namely the nickel and copper content, the capacitance values, the active surface of the deposits expressed by the pore diameter and the thickness of the bridges. Therefore, three representative groups have been built to identify the optimum domains:

- I: the ratio between the average values of the capacitance and the surface:

$$\left(\frac{\bar{C}}{S}\right) = \frac{\frac{C}{S}}{\left(\frac{C}{S}\right)max} \quad (4)$$

- II: the ratio between the pore diameter and the bridges thickness of the deposited alloy:

$$\left(\frac{\overline{D\,pore}}{G\,bridge}\right) = \frac{\frac{D\,pore}{G\,bridge}}{\left(\frac{D\,pore}{G\,bridge}\right)max} \quad (5)$$

- III: the ratio between the concentrations values of nickel and copper in the analyzed samples:

$$\left(\frac{\overline{Ni}}{Cu}\right) = \frac{\frac{Ni}{Cu}}{\left(\frac{Ni}{Cu}\right)max} \quad (6)$$

3. Results and discussions

The dependence of the normalized ratio of capacity on surface according to the normalized temperature and normalized current flow

Data previously published in [10-13] were transformed in normalized or dimensionless groups using equations (1-6). For the representation of the contour chart of the normalized ratio of capacitance and surface as a function of normalized temperature and normalized current flow (Fig.1.), the normalized values of current flow and temperature and those of capacitance reported at surface were used.

From fig.1, one may see that two domains of maximum values have been obtained for the normalized ratio of capacitance and surface. The first domain is recorded for values of the normalized current flow between 0.34 and 0.35 and for a normalized temperature within the range of 0.96 – 1. The second domain is recorded for values of the normalized current flow between 0.71 and 0.79 and at a normalized temperature range between 0.959 – 0.979.

Therefore, it can be concluded that in order to obtain a capacitor with high values of the capacitance reported to the surface, one may consider as optimal working range, the second domain identified above, due to the wider range of values of the respective normalized current flow, of the normalized temperature.

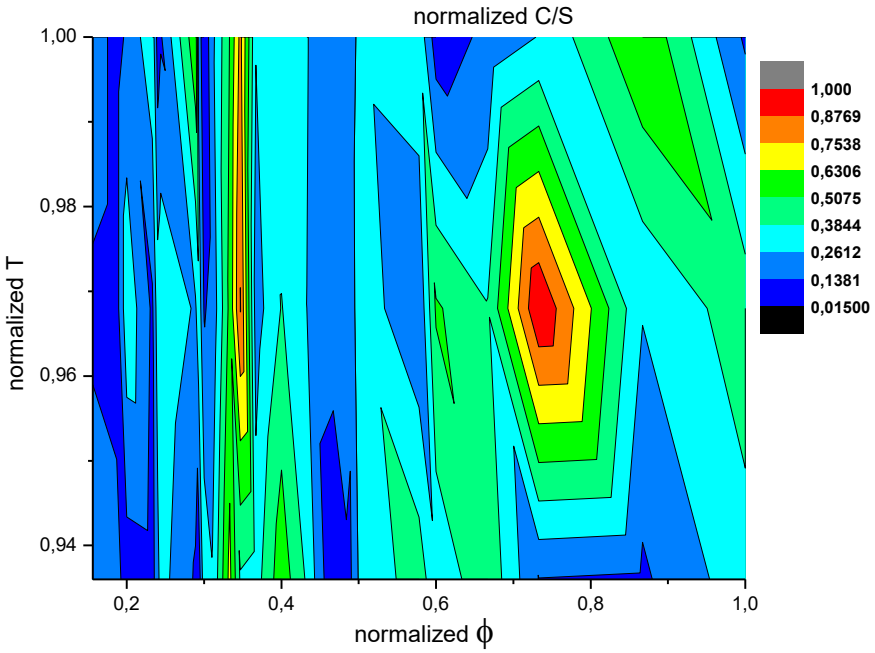

Fig.1. The contour chart of the normalized ratio of capacitance and surface according to normalized temperature and normalized current flow

The dependence of the normalized ratio between the diameter of the pores and the thickness of bridges by normalized temperature and normalized current flow

In order to represent the contour chart of the normalized ratio between the pore diameter and the bridge thickness depending on the normalized temperature and the normalized current flow (Fig.2.), one used the normalized values of the current flow obtained from the ratio of current density value to that of the deposition time on its highest value, the normalized values of the temperature obtained from the ratio of the average temperature to the highest temperature value.

In Fig.2. the optimum conditions may be observed in domain with the minimum ratio between the pore diameter on the bridge thickness. The optimum range of values for the normalized current flow is between 0.59 and 0.63, at a normalized temperature range between 0.97 and 1.

It can be concluded that the ratio between the pore diameter and the bridge thickness must be minimal, because if the alloy is used as catalyst, a material with potential catalytic properties and a maximum specific surface area is obtained.

This method may represent an alternative with better pore size control over the method of obtaining Raney-nickel skeletal catalysts.

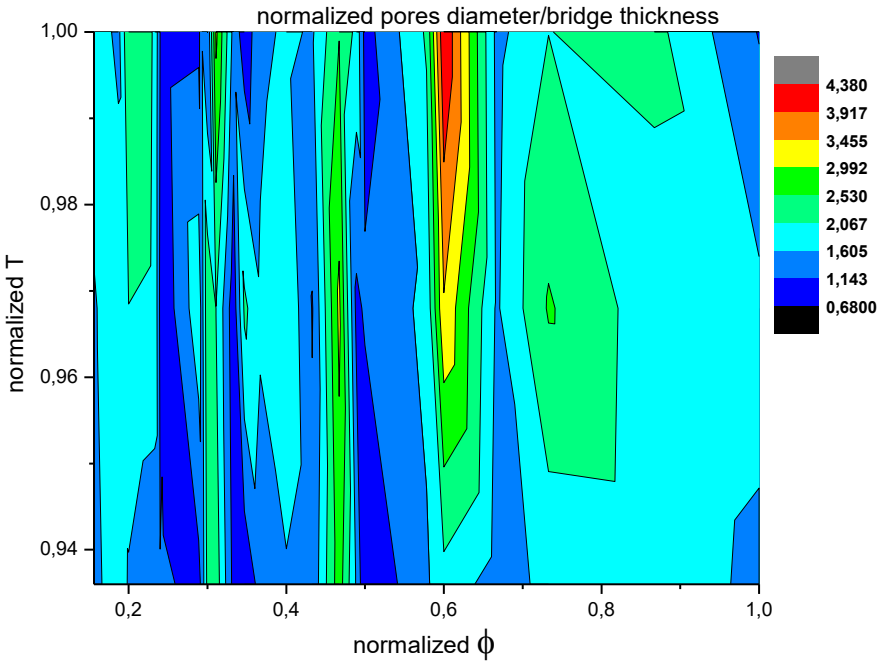

Fig.2. The contour chart of the normalized ratio between the pore diameter on bridge thickness according to normalized temperature and normalized current flow

The dependence of the normalized ratio between nickel and copper concentration according to normalized temperature and normalized current flow

In order to represent the contour chart of the normalized ratio between the nickel concentration on copper concentration according to normalized temperature and normalized current flow (Fig.3.), one has used the normalized values of current flow, obtained from the ratio between the average current density and the deposition time on its highest value, the normalized values of the temperature obtained from the ratio of average value of temperature to highest temperature value.

From Fig.3, one may observe two optimum intervals for the normalized ratio of the nickel on copper concentration depending on the normalized temperature and current flow. The first domain is recorded for values of the normalized current flow between values 0.71 and 0.8 and at normalized temperature within the range of values 0.952 – 0.979. The second domain is recorded for values of the normalized current flow between 0.42 and 0.43 and in a temperature range between 0.963 – 0.972.

It can be concluded that in order to obtain a capacitor with high values of the concentration of nickel relative to copper, it can be considered as the optimum working domain, the first domain due to the wider range of values of the current flow and the temperature.

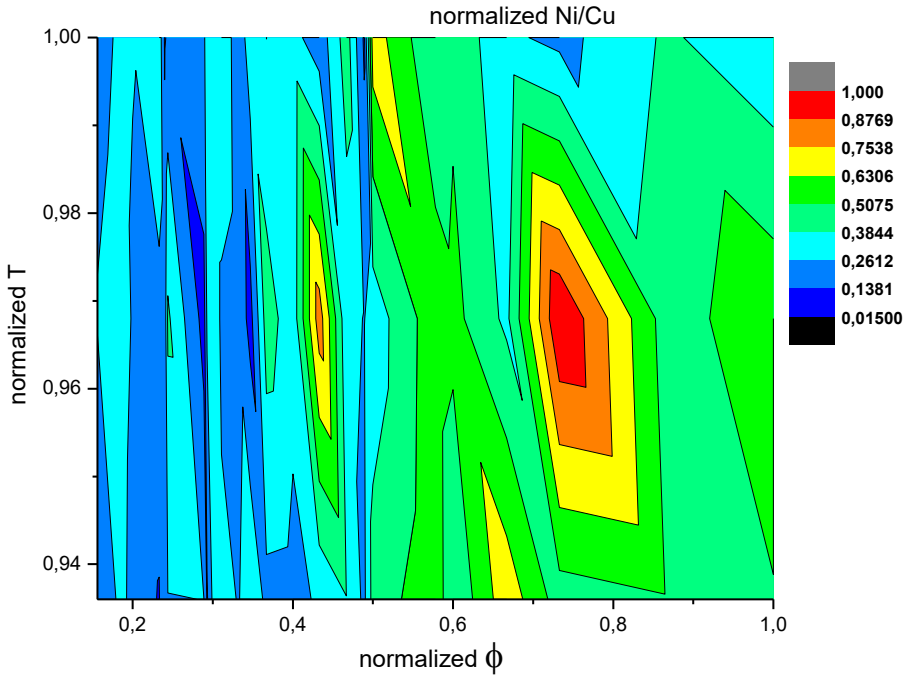

Fig.3. The contour chart of the normalized ratio of nickel on copper concentration according to normalized temperature and normalized current flow

The dependence of the normalized ratio between nickel and copper concentration according to normalized temperature and normalized electrical charge

In order to represent the contour chart of the normalized ratio between the concentration of nickel on copper depending on the normalized temperature and the normalized electrical charge (Fig.4.), one has used the normalized values of the electric charge obtained from the ratio of the product to the current density value, deposition time and surface reported to its highest value, the normalized values of the temperature obtained from the ratio of the average temperature value to highest temperature value.

From Fig.4. it can be observed that two optimum intervals are obtained for the normalized ratio of nickel on copper concentration depending on the normalized temperature and electric charge. The first domain is registered for normalized electric charge values in the range 0.24 – 0.27 and at a normalized temperature in the range of 0.952 – 0.98, while the second domain is recorded for normalized electric charge values in the range 0.57 – 0.59 and at a temperature range between 0.964 – 0.972.

It can be concluded that in order to obtain a capacitor with high values of the concentration of nickel reported to copper, it can be considered as the optimum working range, the second domain due to the wider range of values of the electric charge and the temperature.

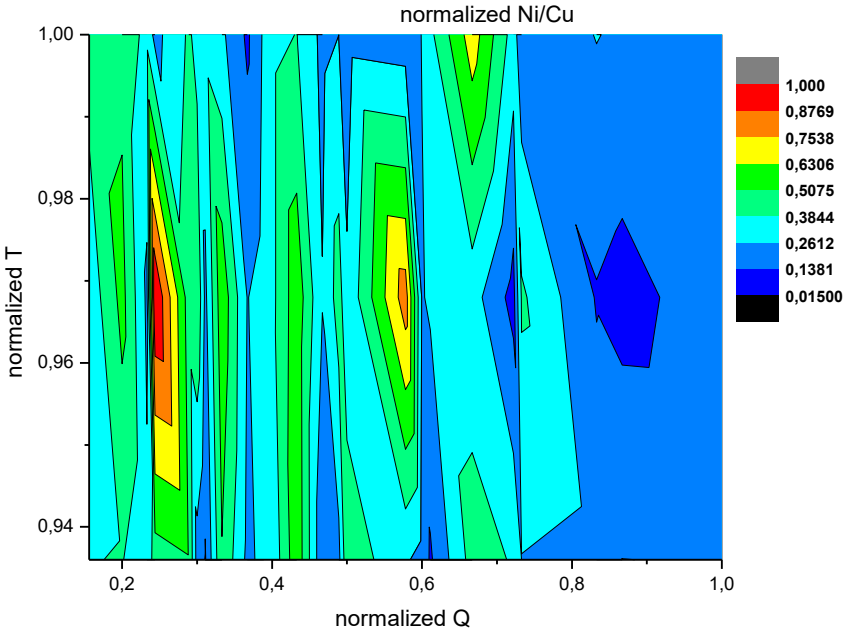

Fig.4. The contour chart of the normalized ratio of nickel to copper concentration according to normalized temperature and normalized electrical charge

4. Conclusions

Optimum domains for the electrodeposition of nickel-copper alloys have been established so that they correspond to the specific requirements of use. The processing of the experimental data obtained was done in an easily interpretable form that correlated the parameters of the obtaining process with the final characteristics of the nickel-copper deposits, using the contour-type charts from which the optimum domains for each interest parameter were extracted. Thus, the interest parameters for the performance of supercapacitors were identified, namely: the ratio between the average values of the capacitance and surface, the ratio between the pore diameter and the bridges thickness of the deposited alloy, the ratio between the values of the concentrations of nickel and copper in the analyzed samples.

Acknowledgement: Miss Ioana-Alina Ciobotaru has been funded by the Operational Programme Human Capital of the Ministry of European Funds through the Financial Agreement 51668/09.07.2019, SMIS code 124705.

REFERENCES

[1]. Rusi, S.R.M., Effects of Electrodeposition Mode and Deposition Cycle on the Electrochemical Performance of MnO_2-NiO Composite Electrodes for High-Energy-Density Supercapacitors, *Plos One*, 11, 5, (2016), 1-16.

[2]. Wang G., Zhang L., Zhang J., A review of electrode materials for electrochemical supercapacitors, *Chemical Society Reviews*, 41, 2, (2012), 797–828.

[3] Debasish S., Shukla A.K., Das Sarma D., Substrate Integrated Nickel-iron Ultra-battery with Extraordinarily Enhanced Performances, *ACS Energy Letters*,1, (2016), 82-88.

[4] M. Ceraolo M., Lutzemberger G., Poli D., State-Of-Charge Evaluation of Supercapacitors, *Journal of Energy Storage*, 11, (2017), 211-218.

[5] Lokhande C.D., Dubal D.P., Joo O., Metal oxide thin film based supercapacitors, *Current Applied Physics*, 11, (2011), 255-270.

[6] Devivier C., Tagliaferri V., Frovalusci F., Ucciardello N., Mechanical characterization of open cell aluminium foams reinforced by nickel electro-deposition, *Materials and Design*, 86, (2015), 272-278.

[7] Mirzaeian M., Ogwu A.A, Jirandehi H.F., Aidarova S., Ospanova Z., Tsendzughul N., Surface Characteristics of Silver Oxide Thin Film Electrodes for Supercapacitor Applications, *Colloids and Surfaces A: Physicochemical and Engineering Aspects*, 519, (2017), 223-230.

[8] Choi B.N., Chun W.W., Qian A., Lee S.J., Chung C.H, Dendritic Ni(Cu)-polypyrrole hybrid film for a pseudo-capacitor, *Nanoscale*, 7, (2015), 18561-18569.

[9] Kumar Meher S., Justin P., Ranga Rao G., Nanoscale morphology dependent pseudocapacitance of NiO: Influence of intercalating anions during synthesis, *Nanoscale*, 3, (2011), 683-692.

[10]. Ciobotea-Barbu O.C., Ciobotaru I.A., Benga F.M., Vaireanu D.I., The influence of the deposition parameters on the properties of Ni-Cu deposition, *Revista de Chimie*, 70, 1, (2019), 45-49.
[11]. Ciobotea-Barbu O.C., Ciobotaru I.A., Cojocaru A., Benga F.M., Vaireanu D.I., Practical Considerations Regarding the Electrodeposition of Ni-Cu Layers as Potential Supercapacitors Plates, *Revista de Chimie*, 70, 7, (2019), 2335-2339.
[12]. Ciobotea-Barbu O.C., Ciobotaru I.A., Cojocaru A., Benga F.M., Vaireanu D.I., SEM, EDS and electrical capacitance study on electrodeposited Ni-Cu layers, *Revista de Chimie*, 70, 9, (2019), 3210-3212.
[13].Ciobotea-Barbu O.C., Ciobotaru I.A., Vaireanu D.I., Dumitras D.G., Nicolae C., XRD, Raman and SEM surface analysis on Ni-Cu electrodeposited layers, *Journal of Optoelectronics and Advanced Materials*, 21, 7-8, (2019), 536-540.

PRECISION AND REPEATABILITY IN BIODIESEL ANALYSIS

Nicoleta G. STEFAN, Petrica IANCU*, Valentin PLESU

University POLITEHNICA of Bucharest,Chemical and Biochemical Engineering Department, 1-3 Gheorghe Polizu, 011061, Bucharest, Romania

Abstract

Intermediate precision and repeatability of fatty acids methyl esters (FAME) from transesterified Camelina sativa and hempseed oils are investigated in this study. The analysis was performed using gas chromatography coupled with a mass spectrometry detector – a technique which offers good response factor and confirmation of compounds identity based on the spectral information. Standard Deviation (SD) and Relative Standard Deviation (RSD) were calculated for each fatty acid methyl esters. For FAME from Camelina Sativa oil intermediate precision RSD was between 0.822-4.071% while for repeatability RSD was found between 0.395-2.386%. Concerning FAME from hempseed oil intermediate precision RSD was between 0.491-3.107% while for repeatability RSD was found between 0.509-1.594%.

Key words: gas chromatography, mass spectrometry, fatty acid methyl esters, precision, repeatability

1. Introduction

Fatty acid methyl esters (FAME) has been described by the American Society for testing and Materials (ASTM) as mono alkyl esters of long chain fatty acids. Biodiesel is a mixture of FAME from vegetable oils and it's considered an environmentally friendly alternative to conventional diesel fuel [1-4]. Other studies investigated the possibility to obtain valuable products from biodiesel by using special techniques as supercritical CO_2 fractionation [5], molecular distillation [6-7] etc.

FAME is commercially produced by alkali catalyzed (NaOH, KOH, $NaOCH_3$) transesterification with methanol to form esters and glycerol, which results in a short reaction time. The transesterification reaction is reversible and can never reach 100% completion. The complete process includes the transesterification reaction, separation of the raw ester layer from the glycerol layer and esters

* Corresponding author: Email address: p_iancu@chim.upb.ro

purification [8]. Other processes for production of biodiesel involve using a heterogenous catalyst [9]. The advantages of these processes are especially based on separation and reusing of catalyst.

Due to FAME destination as a fuel, its characterization has an important part. Gas chromatography (GC) is one of the most widely used commercial analysis technique because it comes with a lot of advantages: is sensitive, precise, rapid and provides reproducible analysis.

In gas chromatography the mobile phase is a carrier gas (an inert gas like helium) and the stationary phase is a layer of polymer on an inert solid support inside a metal tubing which is the chromatographic column. The capillary column contains a stationary phase. The sample is sent through the column by a stream of carrier gas. Components from the sample are separated because some take longer time to pass through the column than others [10]. The resolution of a GC chromatogram is given by the column length, stationary phase polarity and detector type. GC it's able to separate volatile compounds and to provide a good resolution, but it cannot identify them.

Most methods used to characterize biodiesel are using gas chromatography coupled with a flame ionization detector (GC-FID). An alternative to GC-FID for biodiesel analysis is gas chromatography coupled with mass spectrometry (GC-MS) because it offers the advantage of a separation on a GC column with information about molecules structure obtained by MS detection [11]. In mass spectrometry with electron impact ionization the molecules in the gas phase are bombarded with high energy electrons and form radical cations. These cations are instable and decompose in the detector. The rate of fragmentation usually depends on the molecule's ability to stabilize the positive charge. The resulting fragments are separated by their mass to charge ratio (m/z) in an electric field [12].

A combined GC and MS equipment can be successfully used to analyze complex organic and biochemical mixtures. Spectra compounds are collected by the mass spectrometer as they exit the chromatographic column which identifies and quantifies the compounds according to their mass to charge ratio (m/z). The amount of compound can be determined by integrating the peaks in the total ion count chromatogram (TIC) [13].

Different authors investigated the performance of FID vs. MS in quantifying FAME separated by GC. Koza et al. [14] compared FID response factors (RF) of FAME with those obtained using EI in quadrupole (QP). Seven saturated and unsaturated C15-C17 FAME were evaluated. They showed that good response factor can be obtained for both FID and MS. Dodds et al. [13] conducted a comparative study of GC-FID and GC-MS methods and they founded that GC-MS offers two important advantages: the ability to confirm the identity of analytes based on spectral information and the ability to separate peaks from a noisy background.

The aim of the present work is to validate the analytical method based on GC-MS techniques for FAME obtained by transesterification from vegetable oils. Two kind of oil with different content of FAME are investigated (*Camelina Sativa* oil and hempseed oil) and the final product composition are analyzed in terms of precision and repeatability of measurements.

2. Experimental

Reagents

The chemicals used for this study are: *Camelina sativa* oil and hempseed oil from local sources, anhydrous methanol (99.8% purity), potassium hydroxide (90% purity), anhydrous magnesium sulfate (98% purity), n-heptane (99% purity) and acetone (99.5% purity) from Sigma Aldrich (Germany).

Transesterification of Camelina sativa and hempseed oils

Triglycerides from vegetable oils react with methanol in basis catalysis (1% KOH from the oil mass) to form glycerol and FAME. Although the reaction stoichiometry requires a molar ratio of 3:1 alcohol: triglycerides, an excess of alcohol is necessary to achieve a higher reaction conversion (alcohol: triglycerides 6:1 molar ratio).

For the transesterification reaction a high pressure, stainless steel reactor Berghof, SS316TI model (Germany) is used. Since the reaction should take place in liquid phase, a nitrogen atmosphere is required to create enough high pressure inside the reactor for preventing methanol evaporation. The transesterification reaction is performed at 75°C and safe autoclave pressure has been set at 9 bars. After the completion of the reaction, the mixture is cooled at room temperature. The reaction product is two phases state (FAME and glycerol) and the glycerol can be removed via a separatory funnel. Then, FAME is washed several times with distilled water, dried with anhydrous magnesium sulfate and filtered.

Characterization and quality evaluation of FAME from Camelina sativa and hempseed oils

FAME analysis is carried out using an Agilent Technologies gas chromatograph type 7890A equipped with a triple-axis MS detector (Agilent Technology, 5975C type). A ZB-FAME capillary column was used (30m length, 0.25mm internal diameter, 0.20μm film thickness) and helium as carrier gas at 3 mL/min. The GC injector temperature is 250°C and the transfer line temperature was 280°C. The oven temperature is initially set at 50°C, increasing to 160°C with

5°C per minute, the hold time being 1 minute, then the temperature is increased to 190°C with 2°C per minute and a hold time of 5 minutes. In the next ramp, temperature is increased to 206°C with 1°C per minute and a hold time of 5 minutes. In the last ramp, temperature is increased to 230°C with 3°C per minute and a hold time of 10 minutes. The MS detector is operated in EI mode, with an m/z scanning range from 50 to 550. The FAME peaks were identified according to NIST Database and FAME chromatographic standards. The method used is in according with standards SR EN 14103 [15]. The polarity of the column stationary phase plays a critical role in a successful separation of FAME. To improve peak resolution, the polarity of the column stationary phase should be close to the polarity of the fatty acids.

Results for each component were evaluated in terms of SD (standard deviation) and RSD (relative standard deviation), where SD was calculated with eq. 1 and RSD with eq. 2.

$$SD = \sqrt{\frac{\sum_{i=1}^{N}(x-\bar{x})^2}{N-1}} \tag{1}$$

where x = individual data, $\bar{x}$ is the mean of the data, N = is the number of data

$$RSD = \frac{SD}{\bar{x}} \cdot 100 \tag{2}$$

where $\bar{x}$ is the mean of the data.

3. Results and discussions

After FAME layer separation, washing with distilled water, drying with anhydrous magnesium sulfate and filtration, the products are analyzed using GC-MS technique. Method precision is evaluated at two levels: intermediate precision and repeatability. The intermediate precision is evaluated by data measured on different days but in the same conditions and the same operator. The repeatability is evaluated by comparing data from simultaneous injections of the same solution of FAME in n-heptane in the same day, by the same operator.

FAME identified in GC-MS chromatograms for *Camelina sativa* oil sample are presented in Table 1.

Intermediate precision was evaluated by injecting the samples from the same solution of FAME of *Camelina sativa* oil in n-heptane in five consecutive days. Results are presented in terms of SD and RSD in Table 2 to relate the concentration measurements errors. Standard deviation SD is lower than 0.45% for the main compounds identified in transesterification product.

Table 1

Main FAME content of *Camelina sativa* oil sample

Compound	Chemical formula	Shortened formula	CAS No.	Molar mass (g/mol)
Methyl palmitate	$C_{17}H_{34}O_2$	C16:0	112-39-0	270.5
Methyl stearate	$C_{19}H_{38}O_2$	C18:0	112-61-8	298.5
Methyl oleate	$C_{19}H_{36}O_2$	C18:1	112-62-9	296.5
Methyl linoleate	$C_{19}H_{34}O_2$	C18:2	112-63-0	294.5
Methyl linolenate	$C_{19}H_{32}O_2$	C18:3	301-00-8	292.5
Methyl eicosenoate	$C_{21}H_{40}O_2$	C20:1	2390-09-2	324.5

Table 2

Intermediate precision results for FAME from *Camelina sativa* oil

Compound		C16:0	C18:0	C18:1	C18:2	C18:3	C20:1	Others
day 1	%	6.616	2.128	20.266	23.842	28.420	14.510	4.219
day 2	%	6.591	2.089	19.913	23.731	28.441	15.32	3.920
day 3	%	6.823	2.057	20.246	24.041	28.655	14.749	3.429
day 4	%	6.646	2.047	20.017	23.678	28.575	15.363	3.674
day 5	%	6.961	1.908	20.266	24.394	29.367	14.400	2.704
average	%	6.727	2.046	20.142	23.937	28.692	14.867	3.589
SD	(%)	0.159	0.083	0.166	0.291	0.390	0.449	0.575
RSD	(%)	2.366	4.071	0.822	1.215	1.358	3.020	16.020

The repeatability was evaluated by comparing data from five simultaneous injections of the same solution of FAME from *Camelina sativa* oil in n-heptane. Results are presented in terms of SD and RSD in Table 3 to relate the measurements errors. Standard deviation SD is lower than 0.35%.

Table 3

Repeatability results for FAME from *Camelina sativa* oil

Compound		C16:0	C18:0	C18:1	C18:2	C18:3	C20:1	Others
injection 1	%	6.766	2.133	20.023	23.514	28.290	15.657	3.617
injection 2	%	7.019	2.241	20.397	23.548	27.558	15.424	3.813
injection 3	%	6.880	2.208	20.461	23.319	27.867	15.760	3.505
injection 4	%	7.034	2.276	20.611	23.474	27.562	15.482	3.561
injection 5	%	6.915	2.214	20.565	23.532	27.490	15.632	3.652
average	%	6.923	2.214	20.411	23.477	27.753	15.591	3.630
SD	%	0.110	0.053	0.233	0.093	0.334	0.136	0.117
RSD	%	1.584	2.386	1.141	0.395	1.202	0.875	3.217

FAME composition from hempseed oil is presented in Table 4.

Table 4

Main FAME content of hempseed oil sample

Compound	Chemical formula	Shortened formula	CAS No.	Molar mass (g/mol)
Methyl palmitate	$C_{17}H_{34}O_2$	C16:0	112-39-0	270.5
Methyl heptadecatrienoate	$C_{18}H_{30}O_2$	C17:3	155273-05-5	278.4
Methyl stearate	$C_{19}H_{38}O_2$	C18:0	112-61-8	298.5
Methyl oleate	$C_{19}H_{36}O_2$	C18:1	112-62-9	296.5
Methyl linoleate	$C_{19}H_{34}O_2$	C18:2	112-63-0	294.5
Methyl linolenate	$C_{19}H_{32}O_2$	C18:3	301-00-8	292.5

Intermediate precision was evaluated by injecting the same solution of FAME from hempseed oil in n-heptane in five days. Results are presented in terms of SD and RSD in Table 5 to relate the measurements errors. Standard deviation SD values are lower than 0.5%.

Table 5

Intermediate precision results for FAME from hempseed oil

Compound		C16:0	C17:3	C18:0	C18:1	C18:2	C18:3	Others
day 1	%	7.082	3.924	3.140	7.350	56.795	20.054	1.655
day 2	%	6.997	3.875	3.088	7.289	56.872	20.472	1.407
day 3	%	7.100	3.951	3.197	7.301	57.509	19.834	1.108
day 4	%	7.043	3.891	3.308	7.370	57.033	20.030	1.325
day 5	%	7.130	3.805	3.311	7.414	56.967	19.974	1.399
average	%	7.070	3.889	3.209	7.345	57.035	20.073	1.379
SD	(%)	0.052	0.056	0.100	0.051	0.280	0.239	0.196
RSD	(%)	0.732	1.427	3.107	0.697	0.491	1.190	14.218

The repeatability was evaluated by comparing data from five simultaneous injections of the same solution of FAME in n-heptane. Results are presented in terms of SD and RSD in Table 6. Standard deviation SD values are lower than 0.3%.

Table 6

Repeatability results for FAME from hempseed oil

Compound		C16:0	C17:3	C18:0	C18:1	C18:2	C18:3	others
injection 1	%	7.075	3.864	3.098	7.547	56.699	20.121	1.596
injection 2	%	7.009	3.867	3.176	7.589	56.475	20.527	1.357
injection 3	%	7.086	3.926	3.097	7.388	57.219	20.023	1.261
injection 4	%	7.054	3.899	3.103	7.300	57.008	20.104	1.532
injection 5	%	7.107	3.876	3.091	7.414	56.969	19.975	1.568
average	%	7.066	3.886	3.113	7.448	56.874	20.150	1.463
SD	(%)	0.037	0.026	0.035	0.119	0.290	0.219	0.146
RSD	(%)	0.527	0.670	1.140	1.594	0.509	1.087	9.993

Generally, SD for repeatability must be smaller or equal to SD for intermediate precision. In case of FAME obtained from transesterified *Camelina Sativa* oil (Tables 2 and 3), all the fatty esters are in good agreement with this theory, except C18:1 which has a sensitive higher repeatability SD. Concerning FAME obtained from hempseed oil (Tables 5 and 6), also C18:1 registered a higher repeatability SD compared with the other compounds. In Figure 1a) is presented RSD for each component in both oils. There are differences less than 1.5% for measurements performed for the same sample in the same conditions in different days. In Figure 1b), RSD differences for measurements performed in the same day are less than 1%.

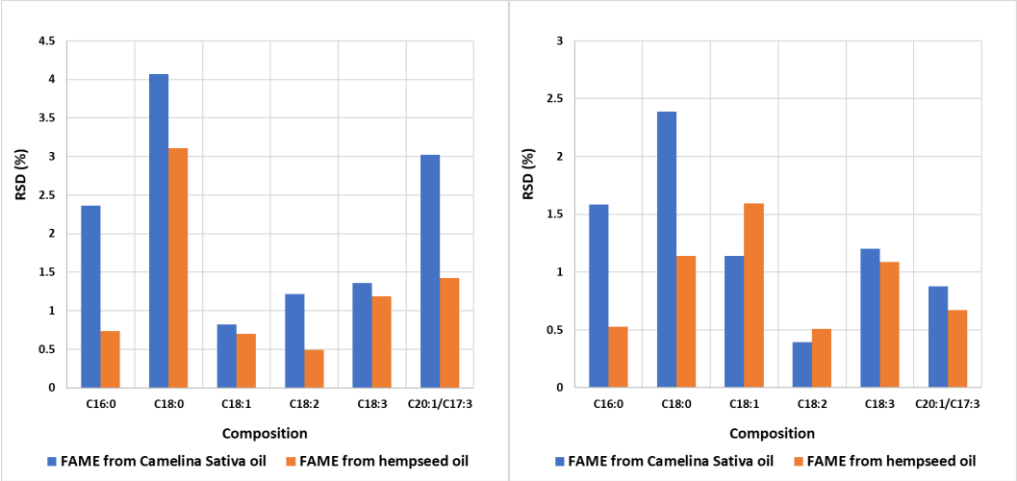

Fig.1. RSD for FAME from *Camelina sativa* oil vs. hempseed oil a) intermediate precision b) repeatability

3. Conclusions

In this study intermediate precision (analysis performed in five consecutively days) and repeatability (five injections of the same sample, in the same conditions and in the same day) of FAME (also known as biodiesel) obtained from transesterified *Camelina Sativa* and hempseed oils were investigated using a gas chromatograph and mass spectrometer detector (GC-MS). Standard deviation (SD) and relative standard deviation (RSD) were calculated for each ester from the FAME mixture. For FAME from *Camelina Sativa* oil intermediate precision RSD is between 0.822-4.071% while for repeatability RSD was found between 0.395-2.386%. Concerning FAME from hempseed oil intermediate precision RSD was between 0.491-3.107% while for repeatability RSD was found between 0.509-1.594%. RSD for repeatability is smaller than RSD for intermediate precision for both types of biodiesel, except C18:1 fatty ester which in both cases is higher.

Acknowledgements: The authors gratefully acknowledge the financial support of the European Commission through the European Regional Development Fund and of the Romanian state budget, under the grant agreement POC P-37-449 (acronym ASPiRE).

REFERENCES

[1] Moser B., Vaughn S., Evaluation of alkyl esters from Camelina sativa oil as biodiesel and as blend components in ultralow-sulfur diesel fuel, *Bioresources Technology*, 101, (2010), 646–653.

[2] Ciubota-Rosie, C., Ruiz, J., Ramos, M., Perez, A., Biodiesel from camelina sativa: a comprehensive characterization, *Fuel*, 105, (2013), 572–577.

[3] Altun S., Yasar F., Oner C., The fuel properties of methyl esters produced from canola oil-animal tallow blends by base-catalyzed transesterification, *International Journal of Engineerring Research and Development*, 2, no. 2, (2010), 2-5

[4] Rashid U., Anwar F., Moser B., Ashraf S., Production of sunflower oil methyl esters by optimized alkali-catalyzed methanolysis, *Biomass and Bioenergy*, 32, (2008), 1202-1205.

[5] Cheng Y.J., Shieh C.J., Wang Y.C., Lai S.M., Chang C.M., Supercritical carbon dioxide extraction of omega-3 oil compounds from Ficus awkeotsang Makino achenes. *Separation and Purification Technology*, 98, (2012), 62-68.

[6] Zhang G., Liu J., Liu Y., Concentration of omega-3 polyunsaturated fatty acids from oil of *Schizochytrium limacinum* by molecular distillation: optimization and technological conditions, *Industrial and Engineering Chemistry Research*, 52, (2013) 3918-3925.

[7] Iancu P., Ştefan N.G., Plesu V., Toma A., Stepan E. Advanced high vacuum techniques for ω-3 polyunsaturated fatty acids esters concentration, *Revista de Chimie Bucharest*. 66(6), (2015) 911-917.

[8] Savaliya M.L., Dhorajiya B.D., Dholakiya B.Z., Current trends in separation and purification of fatty acid methyl ester: A review, Separation and Purification Reviews, 44, no. 1, (2014), 28-40.

[9] Raducanu C.E., Dobre T., Gogoasa C., Biodiesel production using a sulphonated activated carbon-based catalyst, *Bulletin of Romanian Chemical Engineering Society*. 3, no. 1, (2016), 57-66.

[10] Hussain S.Z., Maqbool K., GC-MS: Principle, technique and its application in food science, International Journal of Current Sciences, 13, (2014), 116-126.

[11] Ecker J., Scherer M., Schmitz G., Liebisch G., A rapid GC-MS method for quantification of positional and geometric isomers of fatty acid methyl esters, *Journal of Cromatography B*, 897, (2012), 98-104

[12] Mjos S., Pettersen J., Improved methods for analysis of fatty acid isomers, *Norwegian Herring Oil and Meal Industry Research Institute, Norway*, 2001.

[13] Dodds E.D., McCoy M.D., Rea L.D., Kennish J.M., Gas chromatographic quantification of fatty acid methyl esters: flame ionization detection vs electron impact mass spectrometry, Lipids, 40. no.4, (2005), 419-428.

[14] Koza T., Rezanka T., Wurst M., Quantitative analysis of fatty acid methyl esters by capillary gas chromatography with flame-ionization detection: quadrupole and sector mass spectrometer. *Folia Microbiologica*, 34, no. 2, (1989), 165-169.

[15] European Standards Fat and oil derivatives - Fatty Acid Methyl Esters (FAME) - Determination of ester and linolenic acid methyl ester contents, SR EN Standard No. 14103 (2011).

COMPRESSOR OIL ASSESSMENT BY USING FT-IR SPECTROSCOPY

Radu MIREA*, Mihaiella CRETU, Laurentiu CEATRA

Romanian Research and Development Institute for Gas Turbines COMOTI,
220 D, Iuliu Maniu Blvd., Bucharest, Romania

Abstract

An experimental assessment of compressor oil degradation was carried out in order to establish its degradation. The monitored screw compressor is using poly-alpha-olefin synthetic oil to compress natural gas. Gas composition and working conditions are continuously affecting the oil, which in this type of compressor exerts multiple functionalities: lubrication, cooling, sealing and compression.

Taking into account the gas composition, the oil type used within the screw compressor directly influences its performances and life span. The literature highlights that a thorough monitoring and analyze of the oil is, in fact, one of the most important ways to assess the performances and usage of a screw compressor. Thus, many of the compressor maintenance issues can be identified and solved resulting in both the increase of its life span and the minimization of the maintenance expenditures. Therefore, basic characteristics determinations - flash point and cinematic viscosity were performed as well as FTIR testing for the collected samples. The degradation tendency of the oil based on the influence of gas characteristics was assessed. FTIR spectra evaluation, highlighted the degradation tendency for base oil at chemical level, leading towards a better understanding of both degradation phenomena and altering of oil characteristics.

Key words: Poly-alpha-olefin, FT-IR spectroscopy, screw compressor, oil degradation,

1. Introduction

Oil injected screw compressors are widely used for medium pressure applications in many industries. Low cost compressors can be adopted for compression of helium or other gases, leading to significant cost savings [1].

Synthetic hydrocarbon lubricants are engineered for particular applications. For compressor applications, poly-alpha-olefin (PAO) based oil is commonly used. PAO provide many of the best lubricating features of a mineral oil and without its drawbacks. Although PAO components are derived from petroleum base stock, they are chemically re-engineered to have a consistent, controlled molecular structure of fully saturated hydrogen and carbon. Because

* Corresponding author: Email address: radu.mirea@comoti.ro

their molecules structure is homogenous, their properties and characteristics are predictable. PAO separate water extremely well, are chemical stabile and have low toxicity. PAOs, however, are not good solvents. The additive chemistry must be adjusted for this fact [2].

Machine conditioning monitoring or predictive maintenance is a practice of assessing a machine's condition by periodically gathering data on machine-health indicators to determine when to schedule maintenance. Knowing to interpret the changes observed in the lubricants properties facilitates the increase of both the uptime and the lifespan of the equipment.

Lubricants are the life blood of wetted machinery. As an important element of predictive maintenance technologies, in-service oil analysis, can provide trace information about machinery wear condition, lubricant contamination and as well as lubricant condition. The immediate benefits of in-service oil analysis include avoiding oil mix up, contamination control, condition based maintenance and failure analysis [3].

Solid contamination (sand and dirt) accelerates the formation of abrasive wear. Liquid contamination such as moisture in oil accelerates machine corrosion. Fuel or coolant dilution will decrease the viscosity, therefore generating more abrasive wear (rubbing wear). It is critical to keep the lubricating oil clean and dry all the time. This requires set cleanliness limits and continue monitoring the contamination during the machine operation [3].

Fourier transformed Infrared spectroscopy can be used for monitoring in-service lubricants, since, as shown in figure 1, 14 out of 17 in-service lubricant's properties of interest can be monitored by this technique.

Property	Type	Infrared Relevant?
Particle Count and Distribution	Contamination/Machine Wear	
Wear Metals	Machine Wear	
Glycol	Contamination	✓
Dissolved Water	Contamination	✓
Emulsified Water	Contamination	✓
Incorrect Lubricant	Contamination	✓
Alien Fluid	Contamination	✓
Fuel	Contamination	✓
Viscosity	Contamination/Breakdown	
Nitration	Oil Breakdown	✓
Sulfation	Breakdown	✓
Oxidation	Breakdown	✓
Soot	Contamination/Breakdown	✓
Acid Number (AN)	Breakdown	✓
Base Number (BN)	Breakdown	✓
Antiwear Additive	Depletion	✓
Antioxidant Additive	Depletion	✓

Fig. 1 Typical lubricant parameters that are measured and the relevance of FT-IR spectroscopy per property [4]

The general trend in the analysis of petroleum products is to use different types of spectroscopy: IR, Raman, etc. since these techniques are becoming more and more adapted and accepted as standard tools of choice to perform tests which previously required wet chemical analysis. The infrared spectroscopy of lubricants rely on a very simple method. You observe how much IR radiation the lubricant absorbs as a function of frequency of the radiation. In general, different lubricants have different spectra, so the main issue is to be sure that an accurate IR spectrum is acquired. [4]

2. Experimental

In order to achieve the fully characterization of the oil degradation it is compulsory to perform a set of determinations. Firstly, the analysis of basic characteristics is needed in order to make a comparison with the characteristics provided by the oil's datasheet. Thus the most important base (basic) characteristics that are firstly measured are flash point and cinematic viscosity. After that, a thorough investigation must be done in order to establish oil degradation at molecular level and the most appropriate way to do this is by the means of FT-IR spectroscopy.

The determination of the flash point can be performed in both open or closed cup apparatus. The one used in this paper is an open cup Scavini automatic flash and fire point tester, as shown in figure 2.

Fig. 2. Scavini automatic flash and fire point tester

Flash point measures the tendency of the sample to form a flammable mixture with air under controlled lab conditions. Flash point is used for shipping and safety regulations to define flammable and combustible materials. Flash point can indicate the possible presence of highly volatile and flammable materials in a relatively non-volatile or non-flammable material. For example an abnormally low flash point in a sample of kerosene can indicate gasoline contamination. [5]

The test cup is filled to a specific level with the sample. The temperature of the sample is increased rapidly at first and then at a slow constant rate as the flash point is approached. The flash point is the lowest temperature at which application of the test flame causes the vapor above the sample to ignite. [5]

The cinematic viscosity determination is, along with flash point determination one of the most important methods to test basic characteristics of an lubricating oil. The viscometer used in this paper is a Scavini ubbelhode viscometer, as shown in figure 3.

Fig. 3. Scavini ubbelhode viscometer

Basically, the viscometer consists of the capillary tube, venting tube and filling tube, capillary with the measuring sphere and reference level vessel. Above and below the measuring sphere there are two markers indicating the timing of oil level.

The sample runs down from the capillary as an thin film under atmospheric pressure, while the time in which the sample flows is clocked. The diameter of the capillary should be selected accordingly with the viscosity of the

measured (analyzed) sample. For samples with low viscosity values a smaller capillary is recommended in order to mitigate the measurement errors. [6]

For all the oils used in industrial applications, the datasheet provided by the producer gives the viscosity at 40°C, so all the measurements are made in a thermostatic bath. Depending on the heating fluid used the temperature in the thermostatic bath can vary from room temperature up to 150°C.

FT-IR analysis is a versatile tool for detecting usual contaminants, forming of secondary products and degradation of the additives packages or base oils, thus becoming a wide spread technique related to multiple evaluation of oils degradation. The FT-IR technique is based on the mathematical operation called Fourier transform and the adsorption lines of the sample are correlated with the ones already known for each type of chemical bond. So, initially a reference spectra is acquired for a fresh sample of oil. Then, the spectra for the sample is acquired and after that, the two spectra are compared and registered differences can provide info related to the changes within oil composition, degradation, contamination and equipment wear.

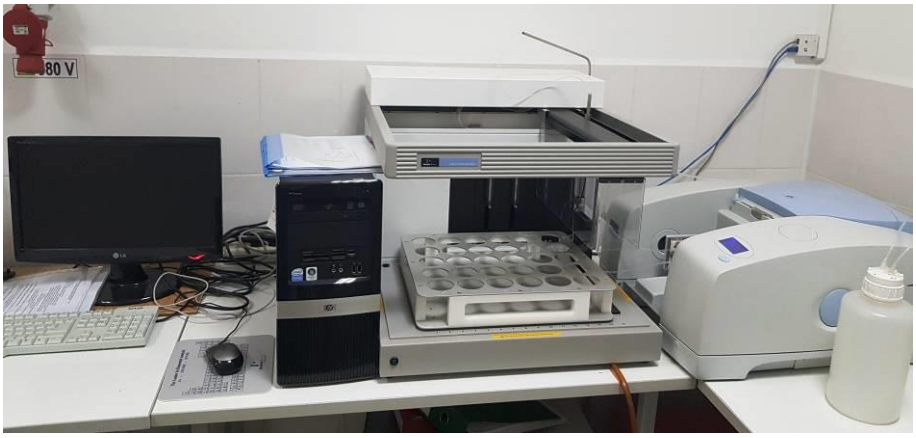

Fig. 4. Perkin Elmer oil spectrometer and autosampler

The analytical instrument used for determinations is a Perkin Elmer oil spectrometer equipped with auto sampler, as shown in figure 4, and provides important information regarding the lubricating oil degradation at several levels as follows):

- degree of oxidation. The oil exposed to oxygen at elevated temperatures will oxidize to a variety of compounds, the majority of which are carbonyl compounds, including carboxylic acids. These acids contribute to the acidity of the oil, depleting the basic additives present in the oil and contributing to corrosion. The degree of oxidation is a good indicator of oil degradation. A rapid increase in oxidation may indicate an overheating or a depletion of the anti-oxidant additive due to an over-extended oil change period.

- nitration value. Nitrogen oxides produced form the oxidation of atmospheric nitrogen during the process, react with the oil. Nitration increases the viscosity of the oil and is the major cause of build-up of varnish. A high nitration value, known as NO_x, indicates excessive loads and/or low operating temperature.

- sulfate value. Sulfur oxides are produced by the reaction of sulfur compounds present in oil with water and can lead to the formation of sulfuric acid. The sulfuric acid is neutralized by the oil's basic additives. A rapid increase of the sulfate value may indicate a high value of sulfur in the compressed gas or a rapid depleting of anti-wear additive.

- ester breakdown. Synthetic oil usually contain a high proportion of poly-ol esters. These esters are susceptible to breakdown in the presence of water and acids (hydrolysis). Ester breakdown contributes to the acidity of the oil and can result in the formation of crystals of the base poly-ol and clogging the filters.

- anti-wear additive depletion. Anti-wear additives are consumed during the normal life of the oil. The consumption of the anti-wear additives is accelerated by the presence of water. A rapid loss of anti-wear additive may indicate excess load or water contamination.

- IR spectra. Having the reference spectra of the analyzed oil, a comparison between the fresh and used oil spectra can be made in order to assess the oil degradation. Although all oil producers do not make public their oil recipe and, thus, it cannot be anticipated which are the degradation products that should be contained by an used oil, a correlation of the information regarding gas composition, physical characteristics and the possible structures that absorb IR radiation at certain wavelengths can result in an appropriate assessment of the oil degradation. It is to be known that the spectrometer's software is provided with its own libraries making possible the visualization of almost all possible structures. [7]

3. Results and discussions

The monitoring protocol states that oil sampling should be made every 500 operating hours, in order to assess oil degradation. Also the sampling protocol must be followed in order to obtain the most representative samples.

Thus, 3 samples have been brought to the lab in order to be analyzed, until the oil has been changed. Table 1 provides a comparison between the values of flash point and cinematic viscosity determined for the used oil samples and the ones stated in the oil's data sheet.

Table 1

Basic characteristics determination

Characteristic	***Cinematic viscosity at 40 °C, mm²/s (cSt)***	***Flash point,° C***
Method	*SR ISO 3104-2002*	*ASTM D92 - 05a*
Equipment	*SCAVINI ubbelhode viscometer*	*SCAVINI Flash point*
Datasheet values	***100***	***>240***
Stabio S100 - 493 h	49,6	36,9
Stabio S100 - 991 h	33,4	27,6
Stabio S100 - 1487 h	24,34	25,8

As it can be observed in Table 1, the basic parameters of the oil rapidly decrease during working hours. In a screw compressor the oil has three main functions: lubrication, cooling and compression. Thus, unlike other compressor types, the oil comes in direct contact with the gas.

Since the gas in this extraction plant is a "rich" one, it can be anticipated that lubricating oil basic characteristics may decrease. Although the lubricating oil basic characteristics provides valuable information regarding its degradation, it is compulsory to perform its chemical degradation assessment, before taking any decision.

Having in mind the above mentioned aspects, FT-IR spectroscopy has been made in order to assess the chemical degradation of the oil.

So, a reference spectra has been acquired using new, unused oil and the first sample's spectra has been compared with it, as shown in figure 5

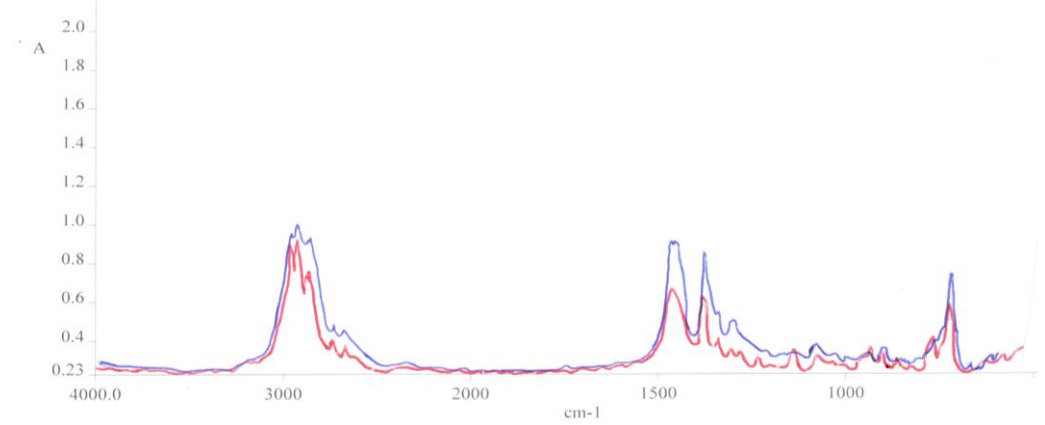

Fig. 5. Comparison between Sample 1 spectra and reference spectra

In table 2, the main indicators regarding oil chemical degradation are shown. It must be emphasized that provided values, represents only the difference between the two spectra.

Table 2.

Sample 1 compared with reference

Characteristic	Values
Antiwear (A/cm)	0.00
Ester BD (A/cm)	1.27
Hydroxy (A/cm)	0.00
NO_x (A/cm)	1.24
Soot 1980 (A/cm)	0.50
Soot 3800 (A/cm)	1.48
Sulfate (A/cm)	0.00
Water (%)	0.00

As it can be seen in tables 1 and 2, during the first 500 working hours, the gasoline present in the natural gas determined both an oil "dilution" (low flash point and low cinematic viscosity) and a slightly depletion of the esters content in the oil. Also the presence of NO_x in the used lubricating oil along with an increased value of Soot indicates an compressor overload.

Anti-wear additive has not been affected during the operation and also, there is no oxidation since, it is well known that "rich" gas contains only trace amounts of water.

After analyzing the IR spectra, and correlating it with gas composition, chemical degradation indicators and possible structures that may occur at different wavelengths, it results that the base oil has been degraded due to the gas composition in short chain substitutes, namely: short chain - methyl, ethyl, propyl, and long chain C_4 mainly with straight chain.

This analysis highlights the fact that the gasoline within the natural gas has blended with the oil thus introducing these substituents in its chemical structure.

The second sample has been brought in the lab after another 500 or so working hours. As it can be seen in table 1, the basic characteristics of the oil continued to decrease but at a slower rate, meaning that the oil is almost saturated in gasoline.

A new IR spectra has been obtained and compared with the previous one, as shown in figure 6.

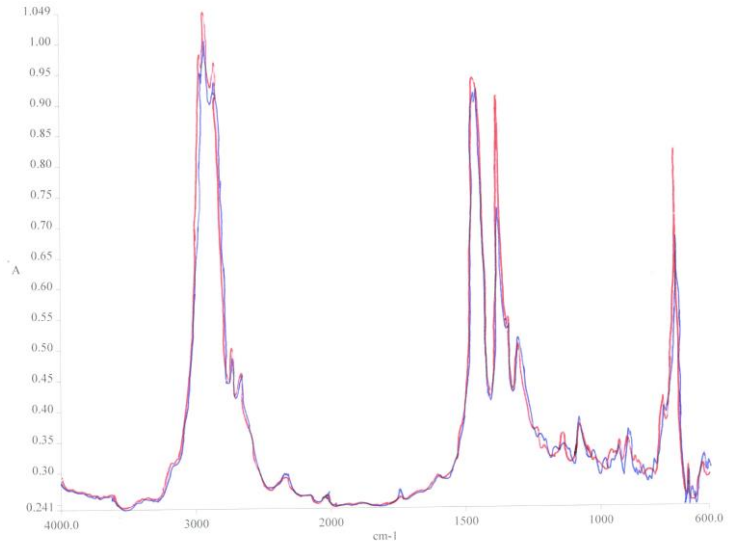

Fig. 6. Comparison between Sample 2 spectra and Sample 1 spectra

In table 3 are shown the main indicators of oil chemical degradation. As mentioned above, the values are for the differences between the two samples.

Table 3

Sample 2 compared with sample 1

Characteristic	**Values**
Antiwear (A/cm)	0.00
Ester BD (A/cm)	1.22
Hydroxy (A/cm)	0.00
NO_x (A/cm)	1.44
Soot 1980 (A/cm)	0.33
Soot 3800 (A/cm)	1.54
Sulfate (A/cm)	0.00
Water (%)	0.00

As it can be seen from table 1 and 3, during the first 1000 working hours, the oil kept degrading, but at a slower rate than in the first 500 working hours. Nevertheless almost the same oil constituents have been degrading and, after analyzing IR spectra it is clearly shown that more and more functional C_1 to C_4 substituent occur in oil's chemical structure with a higher ratio of C_4 substituents, also with straight chains.

The third sample was brought in the lab after almost 1500 working hours, and the above mentioned analysis has been performed.

Table 4 contain the most important indicators for chemical degradation.

Table 4

Sample 3 compared with sample 2

Characteristic	**Values**
Antiwear (A/cm)	0.75
Ester BD (A/cm)	1.27
Hydroxy (A/cm)	0.00
NO_x (A/cm)	1.82
NO_x vs Oxid (A/cm)	4.00
Oxidation (A/cm)	1.41
Soot 1980 (A/cm)	0.00
Soot 3800 (A/cm)	2.02
Sulfate (A/cm)	0.00
Water (%)	0.00

As it can be seen in Table 1, the basic characteristics continued to decrease, reaching a critical value for compressor's integrity. Also, in Table 4, two new indicators are shown: Oxidation and NO_x vs. Oxid, so the oil started to oxidize. The presence of oxidation indicates a depleting of base additives of the oil that causes the compressor corrosion and also it shows that the oil change period has been over-extended. It can be stated also that the anti-wear additive started to deplete.

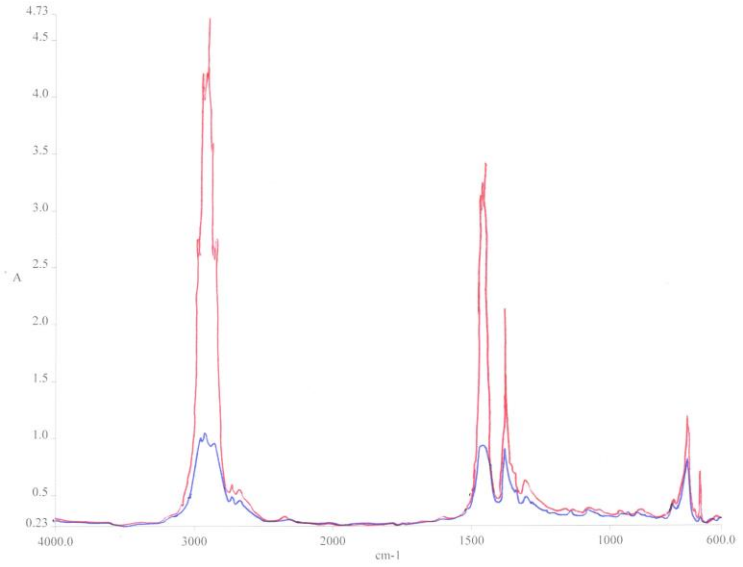

Fig. 7. Sample 3 compared with sample 2 spectra (Comparison between Sample 3 spectra and Sample 2 spectra)

By analyzing the comparative IR spectra (Fig.7), it can be emphasized that a main part of the oil has been transformed in C4 substituents, thus causing the loss of almost any oil like characteristics.

6. Conclusions

- A "rich" natural gas is constantly affecting a PAO based oil, even more when the oil is in direct contact with the gas as the case in screw compressor. So, it can be concluded that PAO based oil may be suitable for other types of compressor applications where the oil it is not in direct contact with the gas, or PAO based oil can be used in screw compressors but in "poor" gas extraction sites.
- FT-IR spectroscopy is a very useful tool to assess oil degradation since it provides valuable information regarding the chemical structure of the compounds of a sample.
- By coupling FT-IR spectroscopy with other analysis, a complete "picture" of oil degradation can be acquired, thus minimizing the risk of compressor breakdown and also its maintenance can be made more easily.
- It is well known that gasoline, acting as diluents is constantly affecting the oil, but the degree of this action can only be assessed by using deep analysis techniques as FT-IR spectroscopy.

Acknowledgements:

The research has been carried out within Program NUCLEU, project PN 19.05.02.02, financed by Romanian Ministry of Research and Innovation.

REFERENCES

[1] Seshaiah N., Sahoo R.K., Sarangi S.K. Theoretical and experimental studies on oil injected twin-screw air compressor when compressing different light and heavy gases, *Applied Thermal Engineering*, 30, (2010), 327-339.
[2] Wayne P., Basics of rotary screw compressor lubricants, www.kseser.com/whitepapers, Kaeser Compressors, Inc. 877-586-2691.
[3] Wu X., Xing z., He Z., Wang X., Chen W., Effects of lubricating oil on the performance of a semi-hermetic twin screw refrigeration compressor, *Applied Thermal Engineering*, 112 (2017), 340-351.
[4] Zhao Y. Oil analysis handbook for predictive equipment maintenance, Spectro Scientific, 2014.
[5] User's guide, "Automatic Flash Point Tester Cleveland - ASTM d92", 2010.
[6] Operating instructions, "Ubbelhode Viscometer", 2010.
[7] Perkin Elmer Oil Spectometer, Indicators of chemical degradation, 2010.

CALORIMETRIC DETERMINATION OF MICROWAVE ENERGY ABSORPTION IN - RESONANT OR MULTIMOD APPLICATORS IN A CONTINUOUS-FLOW REACTOR

Daniela GHIMPEȚEANU[1*], Vasile LAVRIC[1], Ioan CĂLINESCU[1], Mariana PĂTRAȘCU[2]

[1]University POLITEHNICA of Bucharest, Faculty of Applied Chemistry and Materials Science, Bioresources and Polymer Science Department, 1-7 Gh. Polizu street., 011061, Bucharest, Romania

[2]Chemspeed SRL, 2 Gara de Nord street., 010856, Bucharest, Romania

Abstract

Microwaves (MWs) cover a broad spectrum of applications, all having in common the MWs capacity of deploying energy "in situ", throughout the interactions matter-electromagnetic field, overcoming the losses implied when the same amount of energy should be transferred through one or several interfaces. When it comes to process intensification, the key is the efficiency of the deployed energy usage by the process.

In this work, we present the performances of a new applicator based upon two concepts: resonance and focus of the electromagnetic field (EM) on the target. At resonance frequency, the cavity stores the MWs energy – therefore, no MWs will be reflected back into the wave guide. The Q factor, proportional to the ratio of energy stored in the resonator and the energy dissipated per cycle, is a measure of the frequency selectivity of the resonator. When the applicator is at resonant frequency, the Q factor is very high. When the dimensions of the applicator are not in resonance with the MWs frequency, the Q factor drops drastically, since the reflected power starts having high values. The reflection coefficient, S11, witnesses how much of the delivered power is reflected back to the wave guide – the lower the value is, the smaller the fraction of power reflected back. The focusing capacity of the applicator is measured with the liquid absorbed power yield, η_{PL}, defined as the ration between the total power dissipated in the liquid phase and the total power introduced in the applicator. Closer to one the values of the yield, higher the applicator capacity to focus the MWs energy on the target.

In the case of MWs with a frequency of 2.45 GHz and TE_{10} mode, the smallest resonant cavity is a cube with the side equal to 86.525 mm. Unfortunately, when placing a load in the resonant cavity and attached a wave guide to it, the interactions matter-electromagnetic field will change the latter, increasing the energy reflected back. Starting from the aforementioned side, the dimensions of the new applicator were searched such that the liquid absorbed power yield to be maximum – the corresponding new side is 145.26 mm.

This new applicator was tested, both in laboratory and in COMSOL Multiphysics® modeling software, for several liquids with very different loss tangent magnitudes and temperature behavior, namely water, ethylene glycol, cyclohexane, acetic acid and 2-propanol, flowing through a special type of reactor, vertically coiled. The MWs generator is a solid-state Miniflow, with a maximum power of 200 W and a special integrated circuit to measure the direct and reflected power. A conventional multi-mode applicator with a special adaptor ensuring the transition from the coaxial guide to WR340 guide, thus permitting the usage of the same solid-state generator, was employed as reference against the new applicator, doing the

* Corresponding author: Daniela Ghimpeteanu, Email address: ghimpeteanu_daniela@yahoo.com

same experimental and simulation work.

The parameters used to compare the performances of both applicators are:

- *the specific power absorbed by the liquid phase (SAR);*
- *the liquid absorbed power yield;*
- *the Q factors;*
- *the reflection coefficient.*

Key words: Microwave, New Applicator, Comsol Multiphisics Modeling Software, Dielectric Parameters

1. Introduction

Microwave heating technology has been used in many areas as a means of selective, volumetric and instantaneous heating. In the process, the electrical energy is first converted into microwave energy, which is then absorbed by a dielectric medium and converted into thermal energy. A better understanding of the efficiency of these methods is needed by quantitative measurement to optimize the microwave heating process and to use it more efficiently. Research reported so far has divided the process of microwave heating in two stages, measuring in detail the efficiency of energy use and studying the effects for different factors. The result of the experiment can vary greatly depending on the position of the sample inside the cavity, the type of heating medium, the microwave output power and the geometric parameters of the heating medium, as well as the ratio between the volume of the sample and the volume of the applicator.

Microwave heating technology uses the most commonly used electromagnetic waves being 915 MHz and 2450 MHz to heat specific materials. Because it is a selective, volumetric and very rapid heating, this method has been widely used in drying, organic synthesis, pyrolysis of biomass and waste, processing of polymeric materials, removal of pollutants from gas or water and many others [3].

So far, there are many simulated data and very few experimental results. A common problem when using microwaves is the variation of the dielectric properties, the shape and dimensions of the sample that is heated.

In several experimental tests it was shown that in the multimodal applicator, the efficiency of the microwaves varies according to the frequency, the dielectric properties, the position of the reactor inside the cavity as well as its geometry [2].

In the work written by Monzo-Cabrera, J. Pedreno-Molina, J.L. Toledo, T, shows that for several dielectric samples, the efficiency varies according to the distance from the magnetron, following a nonlinear curve, noticeable differences of the energy efficiency values between the best and the weakest positions are reported.

The microwave power absorbed by the sample can be determined by the

temperature difference between the initial and final moments, when the sample has been applied a certain microwave treatment.

It is possible to define the energetic behavior of a microwave applicator by the efficiency parameters, which represents the relationship between the incident power and that reflected in the power supply guide. When a single power port is used, the energy efficiency and the reflection coefficient are related to the following equation. Where: η - energy efficiency, S11 - the reflection coefficient for the power port.

$$\eta = 1 - |S_{11}|^2 \quad (1)$$

On the other hand, the microwave power absorbed by the sample may be related to the increase in temperature difference, as explained in Equation 2. Where: Pabs (W) is the microwave power absorbed by the sample, m_{sample} (Kg) is the mass of the sample, Cp (J/ Kg · C) is the specific heat, Δt (° C) temperature difference and, t, is the irradiation time[2].

$$\mathrm{Pabs} = \mathrm{m_{sample}} \cdot \mathrm{Cp} \cdot \Delta\mathrm{t}/\mathrm{t} \quad (2)$$

The efficiency of the conversion from microwave energy (Qmicrowave) to effective heat (Qef) can be calculated using the following equation [3].

$$\eta = Q\ ef / Qmicrowave \quad (3)$$

2. Comparison of dielectric parameters of common organic solvents and water at 2.45 GHz

The most important characteristic of a solvent under MW irradiation conditions are the dielectric constant (Ɛ’), the dielectric loss factor (Ɛ‘’), and the dissipation factor (tan ɗ). The dielectric constant (Ɛ’) depends on the frequency of the MW radiation and temperature. Dielectric loss (Ɛ‘’) represents the quantity of input MW energy that is lost to the sample by being dissipated as heat. The ratio of the dielectric loss to the dielectric constant is an important factor that determines the heating rate of the microwaves. The ability of a substance to convert electromagnetic energy into heat is determined by the dissipation factor (tan ɗ = Ɛ‘’/ Ɛ‘). Therefore, when the dielectric factors of the sample are compared, it is necessary that comparison be made at some fixed temperature [1].

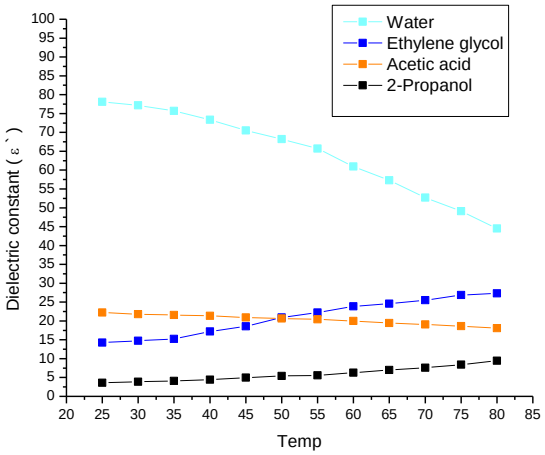

Fig. 1 Dielectric constant (Ɛ')

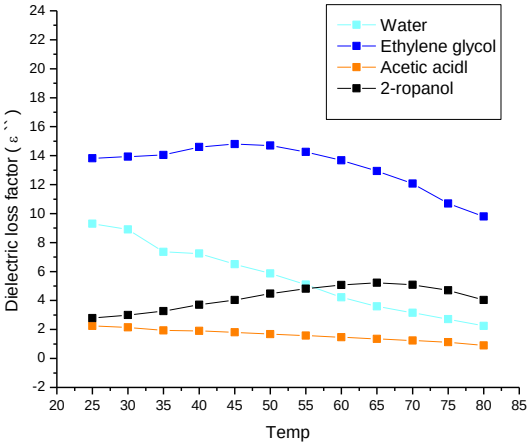

Fig. 2 Dielectric loss factor (Ɛ'')

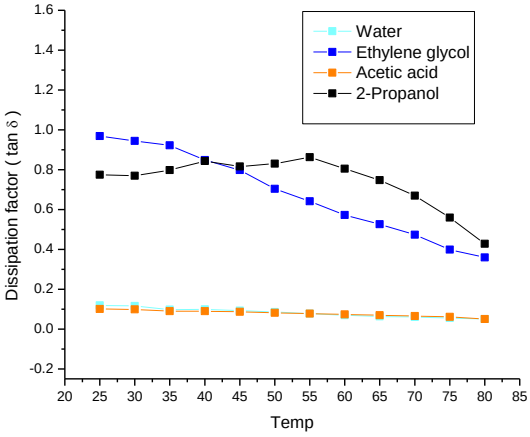

Fig. 3 Dissipation factor (tan d`= Ɛ''/ Ɛ')

3. Comsol Multiphsics® modeling software

Comparative study of the performances of resonant and multimodal applicators using a vertical spiral reactor in dynamic regime. The influence of the dielectric properties of the liquid phase.

Regardless of the fluid used, the inlet flow rate in the reactor is 50 ml / min, the inlet temperature is 25°C, and the power introduced in the applicator is 50 W, with a simulated time of 300 s.

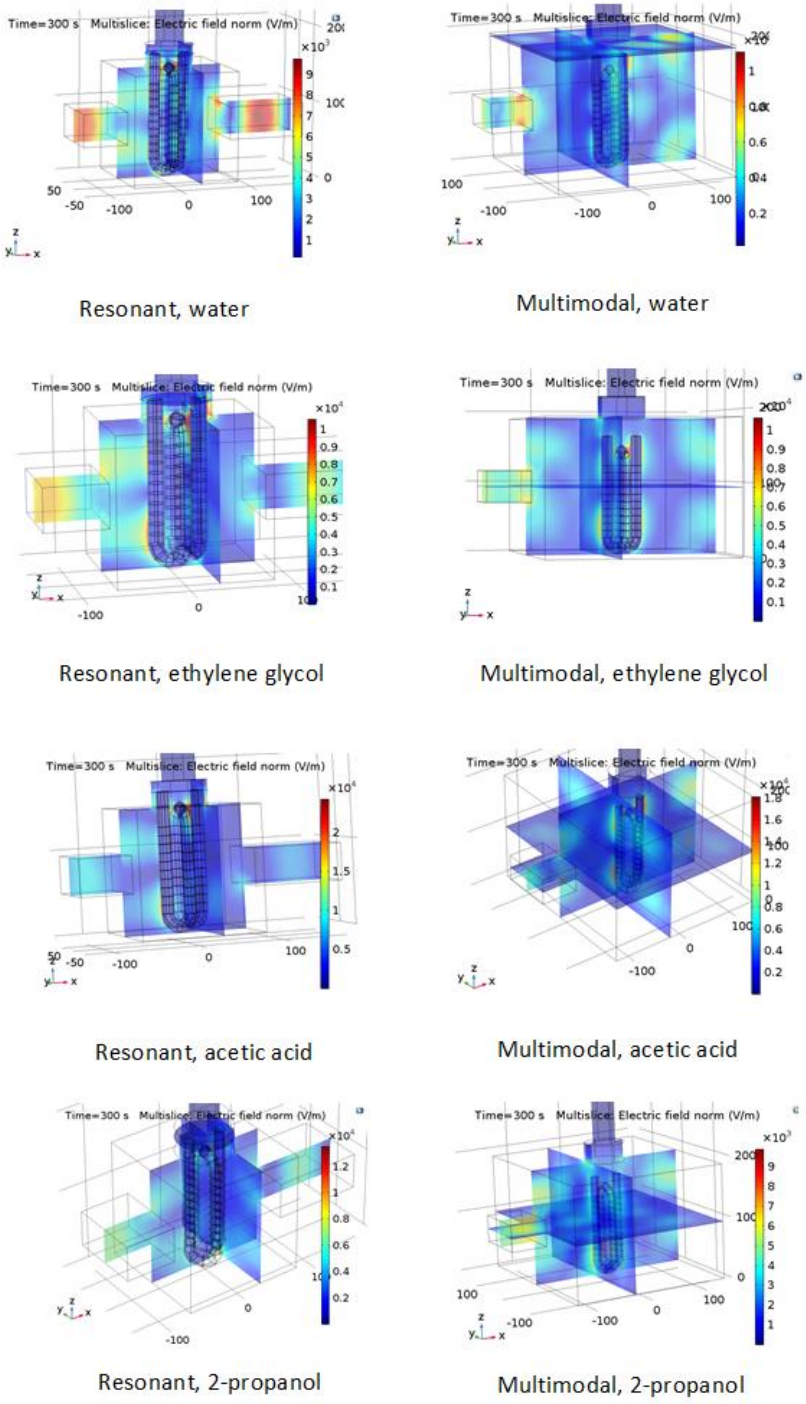

Fig. 4 Spatial distribution of the electric field for distilled water, ethylene glycol, acetic acid, 2-propanol, for the resonant applicator, respectively, the multimodal laboratory applicator.

The uniformity index of the thermal dissipation, UQh, which represents the ratio between the average temperature and its standard deviation - a high value indicates a small standard deviation, compared to the average, therefore, a more uniform distribution.

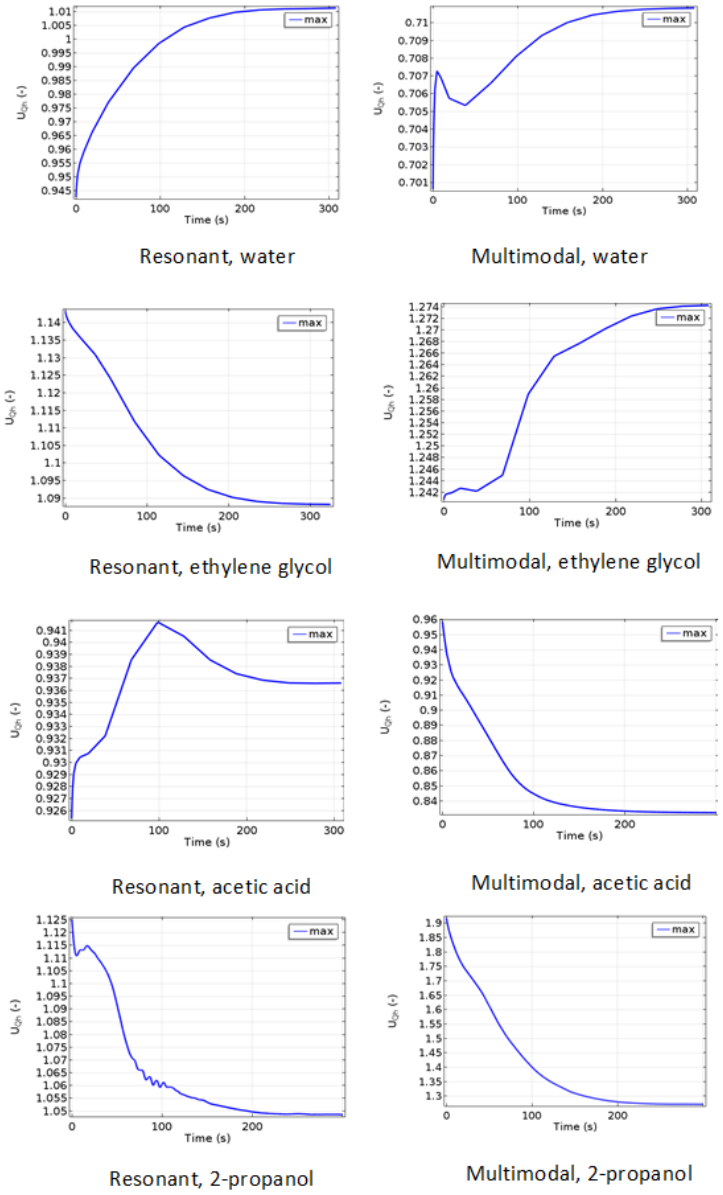

Fig. 5 Temporal variation of the uniformity index of thermal dissipation in the entire liquid phase, for distiled water, ethylene glycol, acetic acid, 2-propanol, in single-mode resonant and multimodal applicator

Another important coefficient, which shows how much of the energy introduced

into the cavity is reflected back, is the parameter S11dB = 20 · log10 (| S11 |). The lower its values, the lower the reflected power. A better behavior of the multimodal applicator is observed, the parameter S11dB having lower values than those of the resonant applicator.

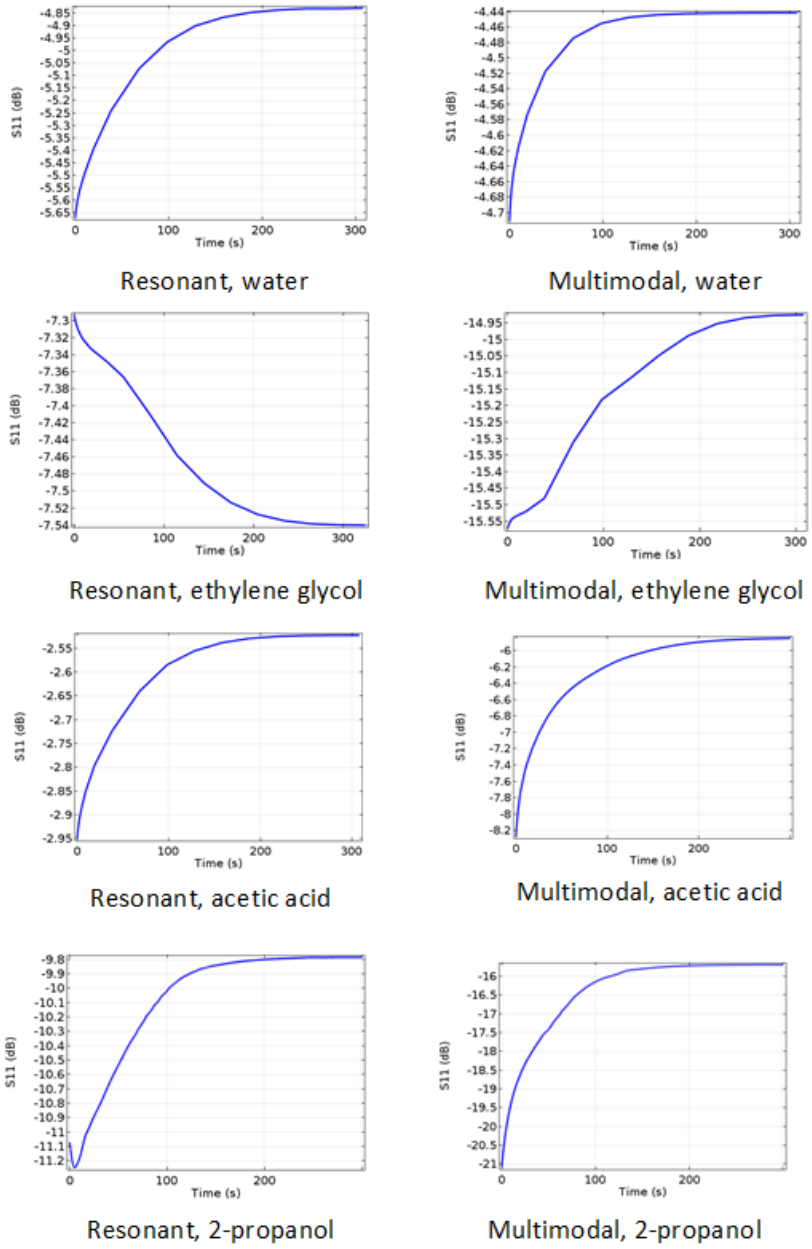

Fig. 6 Temporal variation of parameter S11dB for distilled water, ethylene glycol, acetic acid, 2-propanol, in single-mode resonant and multimodal applicators.

Another parameter of interest, for performance comparison, is the specific power absorbed, SAR (W / kg). Due to the increase of the liquid phase temperature in time and space, the temporal profile of the SAR changes decreasing, to the value corresponding to the thermodynamic balance.

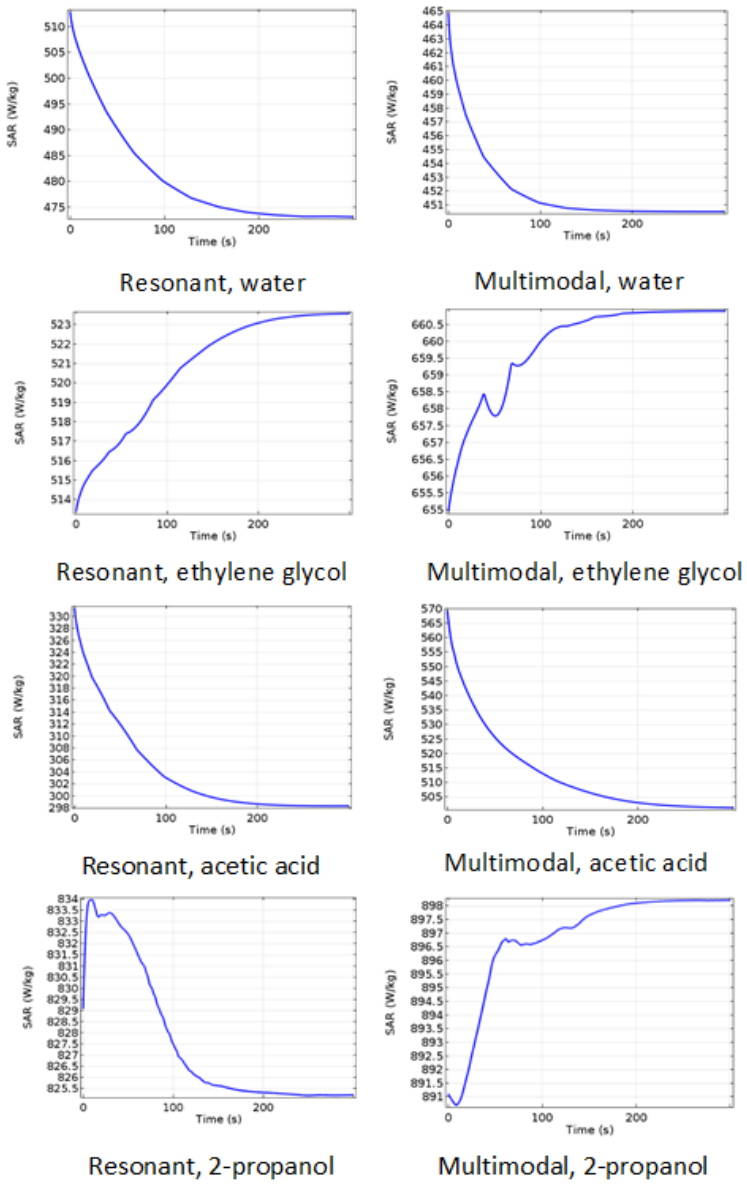

Fig. 7 The temporal variation of SAR for distilled water, ethylene glycol, acetic acid, 2-propanol, in single-mode resonant and multimodal applicator

4. Setup and method

We have carried out activities that allow the experimental investigation of a new microwave applicator (the ability to take microwave energy from liquids with different dielectric properties) in order to optimize the enzymatic pretreatment of lignocellulosic biomass. For this purpose, an experimental installation was carried out by means of which a liquid with the preset temperature and constant flow is pumped through a vertical spiral type reactor which is irradiated with microwaves. The absorbed power by the liquid in the reactor was determined calorimetrically. As a microwave source, the Miniflow solid-state generator was used. Different temperatures were used, at which the dielectric properties of the studied liquid are known and experiments were conducted in the cavity itself and in a multimodal applicator specially adapted to be able to be supplied with microwave energy from the solid-state generator.

In this experiment the infusion of microwaves in a flow system and a reactor in the form of a a vertical spiral, is monitored, by monitoring the temperature at the exit of the reactor. They will be performed in two different equipments, depending on how the microwave energy is applied to the sample, namely: the multimodal system and the single-mode resonant system.

The aim is to establish a working mode for the single mode and multimodal applicator by testing with 4 liquids with different properties. The liquids used are distilled water, ethylene glycol, glacial acetic acid, isopropanol.

Initially, the thermostat and the peristaltic pump are switched on to homogenize the fluid in the system. After a few minutes, the temperature monitoring system and MiniFlow are switched on and left for two minutes to record without microwaves (Initial Temp. 1). Then the microwaves are started at a power around 50 W and left on until the temperature remains constant (Final Temp). After the microwaves are turned off, the temperature is monitored until it returns to its initial value (Initial Temp 2). The temperature is measured in thermostat and at the exit of the reactor with fiber optic, but also with thermocouple. For each temperature set, 2 determinations are made, from 25 ° C to 75 ° C, from 10 to 10 degrees. In each determination, the initial and final temperature are noted when the microwaves are turned off. The power generated by MiniFlow was set to 50 W for all experiments and at 25 ° C more power was tested. For water and ethylene glycol the powers of 25, 50, 75, 100 W were tested and for glacial acetic acid and cyclohexane were tested at 50, 100 and 180 W.

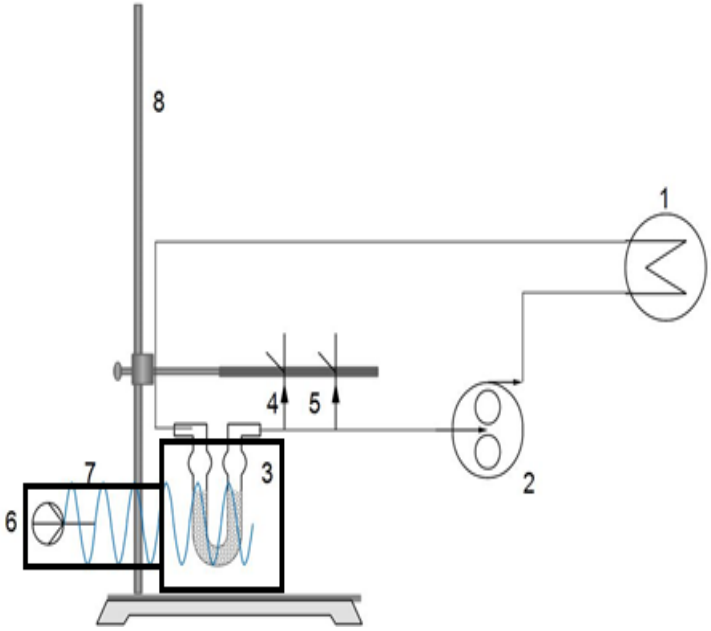

Fig. 8 Experimental set up
1 - Thermostat, 2 - Peristaltic Pump, 3 - Reactor, 4 - Fiber Optics, 5 - Thermocouple,
6 - MiniFlow 200SS, 7 - Microwave Guide WR340

The fluid flow is passed through the peristaltic pump (2) through the thermostat (1), and the liquid used reaching a desired temperature. From the thermostat the liquid enters in a vertical spiral reactor (3). In the reactor the sample is exposed to microwaves at a power of 50 W, generated by MiniFlow (6). The temperature is monitored, for each experiment, using fiber optics (4), but also with a thermocouple (5).

5. Results and discussion

As it can be seen in the graphs below (Fig.9), for distilled water, we have a considerable difference between the multimodal and the resonant applicators.

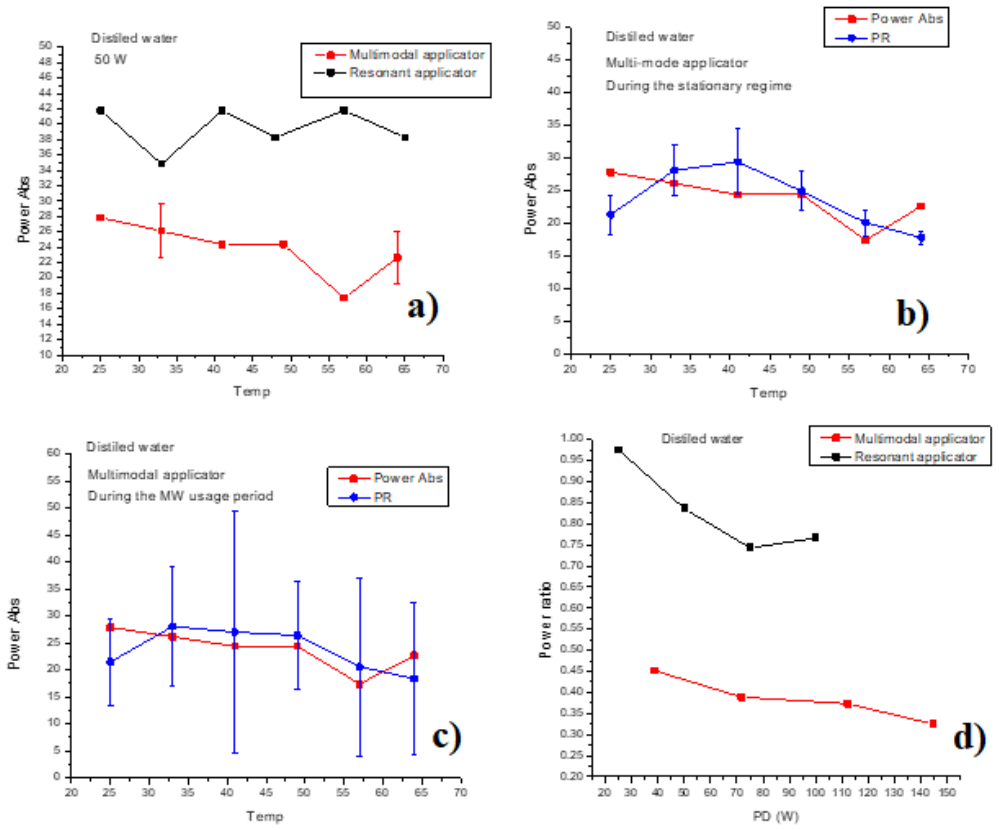

Fig. 9. Results for resonant and multi-mode applicators using distilled reference liquid distilled water

In these graphs we have the values of the experiments for the resonant and multi-mode applicators using as reference liquid distilled water. In the image a) the power absorbed can be observed depending on the temperature; In the image b) the power absorbed according to the temperature can be observed for the multimodal applicator (in the experiments with distilled water only in the multimodal applicator we had reflected power) but also the reflected power (PR) during the stationary regime period for each experiment with the minimum values and maximums for the respective period; In the image c) the power absorbed according to the temperature can be observed for the multimodal applicator, but during the whole heating period (300-400 seconds); and in image d) the differences between the power ratio and the direct power for the two applicators are represented.

In Fig. 10, we have presented the values of the experiments for the resonant and multimodal applicators using as reference liquid ethylene glycol.

In Fig.11 and 12 the results for acetic acid as well as for 2-propanol we have reflected power in the multimodal applicator but also in the resonant applicator.

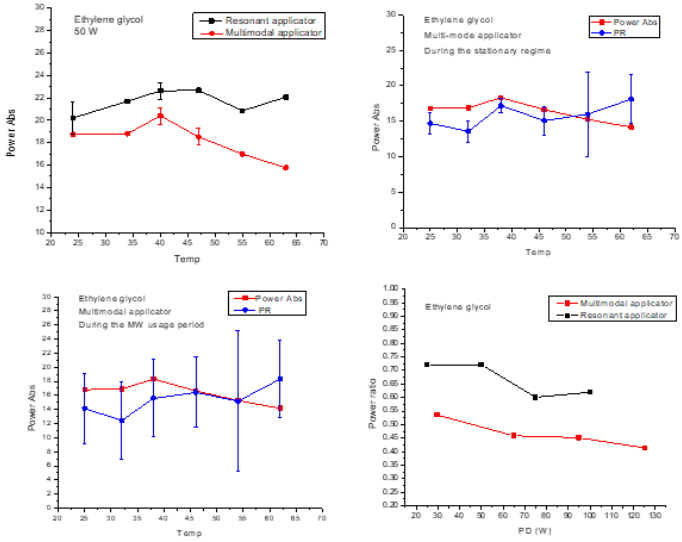

Fig. 10. Results for resonant and multi-mode applicators using distilled reference liquid ethylene glycol

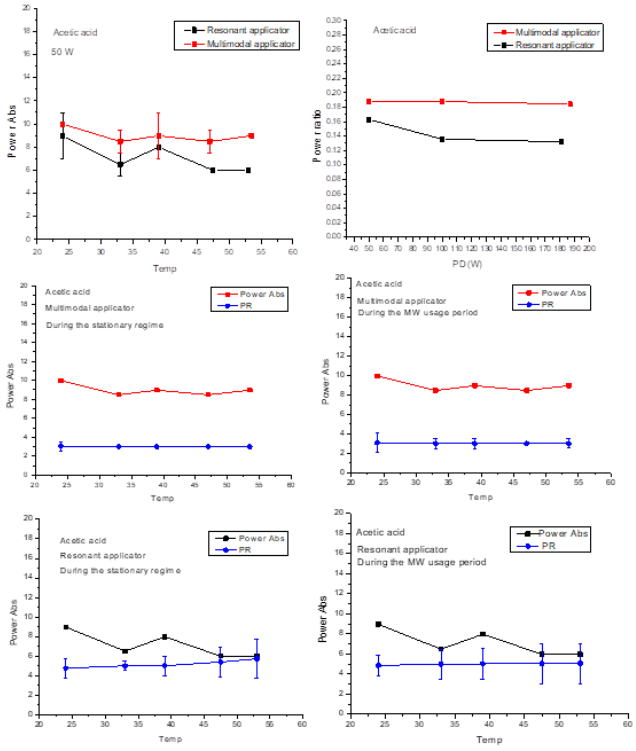

Fig. 11. Results for resonant and multi-mode applicators using distilled reference liquid acetic acid

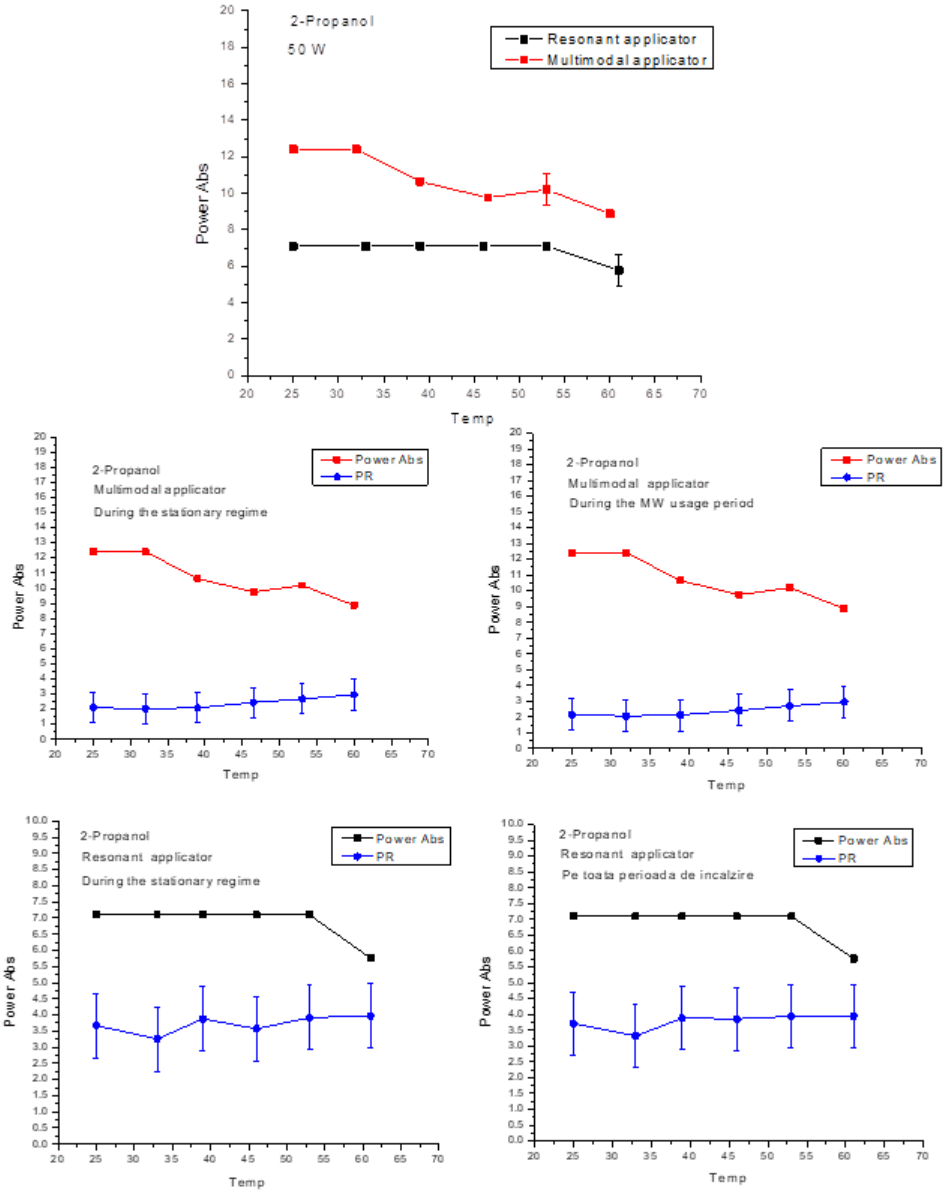

Fig. 12 Results for resonant and multi-mode applicators using distilled reference liquid 2-propanol

6. Conclusions

In the case of modeling in Comsol as well as experimental, we have the same results except for ethylene glycol, where the results are very close for the 2 applicators.

A considerable difference can be observed when using distilled water as the reference liquid between the two applicators. The resonant applicator is superior to the multimodal one.

For acetic acid and 2 propanol we have reflected power for both types of applicators. We can reduce the reflected power to a minimum by using Stub Automatic Tuner.

These differences between the 4 liquids tested in the 2 applicators are due to the dielectric factors.

Acknowledgment

The authors acknowledge the financial support received from the Competitiveness Operational Programme 2014 - 2020, Action 1.1.4: Attracting high-level personnel from abroad in order to enhance the RD capacity, ID project: P_37_471, MY SMIS 105145, Ultrasonic/Microwave nonconventional techniques as new tools for nonchemical and chemical processes, financed by contract: 47/05.09.2016.

REFERENCES

[1] Horikoski S., Matsuzaki S., Mitani T., Serpone N., Microwave frequency effects on dielectric properties of some common solvents and on microwave-assisted syntheses: 2-Allylphenol and the C_{12}-C_2-C_{12} Gemini surfactant, *Radiation Physics and Chemistry*, 81,(2012),1885-1895.

[2] Monzo-Cabrera J., Pedreno-Molina J.L., Toledo T., Feedback control procedure for energy efficiency optimization of microwave-heating ovens, *Elsevier*, 42, (2009), 1257-1262.

[3] Wang W., Zhao C., Sun J., Quantitative measurement of energy utilization effciency and study of influence factor in typical microwave heating process, *Elsevier*, 87, (2015), 678-68.